NATIONAL INSTITUTE FOR FUSION SCIENCE

Resent Developments of Pulsed Power Technology and Plasma Application Research

Edited by Jun Hasegawa and Tetsuo Ozaki

(Received - Oct. 27, 2022)

NIFS-PROC-123 Feb. 5, 2023

Resent Developments of Pulsed Power Technology and Plasma Application Research

Edited by Jun Hasegawa and Tetsuo Ozaki

January 11-12, 2022
National Institute for Fusion Science
Toki, Gifu, Japan

ABSTRACT

The papers presented at the symposium on “Recent trends in pulse power technology and plasma/quantum-beam technology” held on January 11-12, 2022 at National Institute of Fusion Science are collected. The papers in this proceeding reflect the current status and progress in the experimental and theoretical researches on pulsed power technology and quantum beam technology.

Keywords

high power particle beams, high energy density plasma, pulsed power technology, z-pinch, plasma focus, soft x-ray, EUV, neutron source, pulsed discharge, high power micro wave, water treatment, inertial confinement fusion, heavy ion accelerator, fusion reactor

Preface

The symposium entitled “Recent trends in pulse power technology and plasma/quantum-beam technology” was organized as a part of the General Collaborative Research of National Institute for Fusion Science (NIFS) and held on January 11-12, 2022 at NIFS, Toki.

In the symposium, 24 papers were presented in two days, of which 20 papers are reported in this proceeding. The total number of participants was 41 including students and researchers from universities and companies.

The main purpose of this symposium is to provide a forum for a wide range of discussions on pulsed power technology and related technologies, from fundamental researches to various applied researches. Therefore, the papers in this Proceedings reflect recent achievements in experimental and theoretical studies on pulsed power circuit, water treatment, z-pinch discharge, high power microwave, discharge neutron source, ion/cluster sources, inertial confinement fusion engineering, etc. It is our great pleasure with the unexpectedness if the symposium was beneficial to the development of pulsed power and fusion technologies.

We would like to express our sincere thanks to all of the participants, the authors and the staff of NIFS.

Jun Hasegawa
Tokyo Institute of Technology

Tetsuo Ozaki
National Institute for Fusion Science

Contents

(∗National Institute of Technology, Nagaoka College), Makoto Nakamura (National Institute of Technology, Kushiro College), Yoshihiro Kajimura (National Institute of Technology, Akashi College), Kazuhiko Horioka (Tokyo Institute of Technology)

List of Participants

Ken Takayama	(High Energy Accelerator Research Organization)
Hisaki Kikuchi	(Iwate University)
Katsuyuki Takahashi	(Iwate University)
Tetsu Sakakibara	(Iwate University)
Tetsu Ozaki	(National Institute for Fusion Science)
Yuji Inoue	(Tokyo Institute of Technology)
Kazuhiro Matsuda	(Tokyo Institute of Technology)
Jun Hasegawa	(Tokyo Institute of Technology)
Kazuhiko Horioka	(Tokyo Institute of Technology)
Shoto Ito	(Tokyo Institute of Technology)
Tohru Kawamura	(Tokyo Institute of Technology)
Shunta Mochizuki	(Tokyo Institute of Technology)
Hiroaki Ito	(Toyama University)
Seigo Kato	(Toyama University)
Atsuya Miyamoto	(Toyama University)
Miharu Takao	(Toyama University)
Takuho Yamada	(Toyama University)
Atsushi Yamamoto	(Toyama University)
Hirotada Matsui	(Toyama University)
Jun Matsuyama	(Toyama University)
Yosuke Oomura	(Toyama University)
Taichi Takezaki	(Toyama University)
Ryotaro Hasegawa	(Toyama University)
Wataru Tagami	(Toyama University)
Akira Fujino	(Toyama University)
Naoya Okamura	(Nagaoka University of Technology)
Kosuke Okabe	(Nagaoka University of Technology)
Takashi Kikuchi	(Nagaoka University of Technology)
Weihua Jiang	(Nagaoka University of Technology)
Kazumasa Takahashi	(Nagaoka University of Technology)
Toru Sasaki	(Nagaoka University of Technology)
Makoto Obata	(Nagaoka University of Technology)
Souma Ueno	(Nagaoka University of Technology)
Masahiro Moriizumi	(Nagaoka University of Technology)
Taichi Sugai	(Nagaoka University of Technology)
Naoto Watanabe	(Nagaoka University of Technology)
Shoma Watanabe	(Nagaoka University of Technology)
Zhehao Lin	(Nagaoka University of Technology)
Tsuyoshi Imada	(Niigata Institute of Technology)

Tatsuya Horigome (Japan Nuclear Fuel Limited)
Takashi Ebisawa (National Institutes for Quantum Science and Technology)

Silicon Wafer Etching Rate Characteristics Using 150 kHz Band High-Power Pulse Burst Inductively Coupled Plasma

Hisaki Kikuchi, Katsuyuki Takahashi*, Seiji Mukaigawa, Koichi Takaki

Faculty of Science and Engineering, Iwate University

**Agri-Innovation Center, Iwate University*

ABSTRACT

The electrical and etching characteristics were experimental investigated, focusing on the input power and the pulse burst width of 150 kHz band high-power burst inductively coupled plasma. The pulse burst width was varied in the range of 400-1000 μs and repetition rate was set to 10 Hz. A mixture of argon (Ar) and carbon tetrafluoride (CF_4) gas was used and injected into vacuum chamber. During the discharge, about 3 kW of power was applied. The impedance decreases when the plasma was generated, after that increases with time. The electron temperature and plasma density were measured by the double probe method. The plasma density in the etching region was 10^{18}–10^{19} m^{-3}. The target current increased with t burst width. The etching rate of Ar discharge at burst width of 1000 μs was 0.005 μm/min. Adding CF4 into Ar, the etching rate became 0.05 μm/min, which was about 10 times higher. The etching rate increased with burst width.

Keywords

ICP, Etching, High power, Burst pulse, Double probe measurement, CF_4, Ar

1. Introduction

Plasma processing, a material processing technique using plasma, is an essential part of today's manufacturing industries. Inductively coupled plasma (ICP) has been widely used for plasma processing of materials such as deposition of film and etching because of its advantages, such as simple equipment configuration and high density plasma at low pressure[1]. ICP can be generated with electrodeless electrodes, and the positive ions can be independently controlled by the bias voltage applied to the substrate[2].

A new ICP system using burst waves has been developed[3,4]. In this system, the impedance matching circuit which conventional ICP system requires is not necessary because the frequency is set to 100-200 kHz, and the high power can be delivered to the plasma. Therefore, high density plasma can be obtain in this system. In addition, the pulse burst width and duty ratio can be freely set to optimize the process conditions.

In this study, reactive ion etching was performed using a carbon tetrafluoride (CF_4) and argon (Ar) mixed gas atmosphere, and the etching rate was compared with that of physical etching using argon gas atmosphere. It has been reported that the etching rate of the burst wave ICP is affected by the substrate bias voltage and CF_4 contents. In this paper, the influence of the burst width and input power on the electric and etching characteristics was investigated. The electrical characteristics were evaluated by time-resolved measurements.

2. Experimental Setup

Figure 1 shows a schematic of the experimental apparatus. The vacuum chamber consisted of a cylindrical glass tube (51 mm, inner diameter, 55 mm external dimeter). The plasma source consisted of a

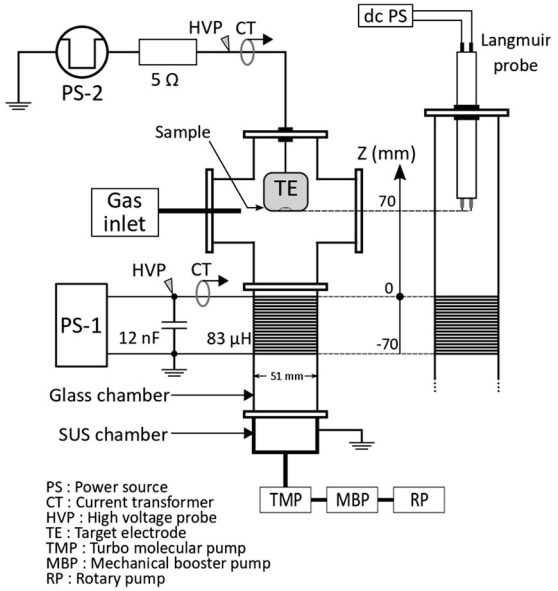

Fig. 1 Schematic of the experimental apparatus.

solenoid coil (50 turns, length 70mm, 83.7 μH) wound on a glass tube. A capacitor (12 nF) was connected to the coil in parallel and was used to build a resonance circuit with the coil. The 400-1000 μs wide high voltage burst pulse with a frequency of 157 kHz were generated using a power supply (PS-1, PEKURIS KJ14-4873) and applied to the solenoid coil to generate ICP. The number of sine waves per burst pulse was 157 for the burst width of 1 ms, and the repetition rate of the burst pulse was 10 Hz. The pressure in vacuum chamber was reduced to 25 mPa using the rotary pump, the mechanical booster pump, and the turbomolecular pump. Argon and tetrafluoro-carbon gases were supplied through mass flow controllers (HORIBA, SEC-400MK3 and SEC-E40MK3) into the chamber. Total gas flow rate was controlled in range of 19.3–41.7 sccm. The solenoid coil voltage and current were measured by a high voltage probe (Tektronix, P6015A) and a current monitor (Pearson, model 110A), respectively. The silicon wafer ((100), 12.6 mm diameter, 250 μm thickness) to be etched was set on the target electrode. A stainless steel mask (12.6 mm diameter, 150 μm thickness) with 1 mm square holes was placed on the wafer. The target electrode was made of titanium (26 mm diameter, 35 mm length) and had a cylindrical shape. The target electrode was placed inside the chamber. The distance between the target electrode and the end of the coil was 70 mm as shown in Figure 1. A negative-polarity rectangular pulse voltage with a pulse width of 1000 μs and a voltage of 800 V was applied to the target electrode by a power supply (PS-2, PEKURIS KJ06-3265) via a current limiting resistor of 5 Ω consisting of two 10 Ω resistors connected in parallel. The repetition rate, the burst width and the application timing were synchronized with the burst signal. During the first 3 min of etching, the presputter process was done by gradually increasing the bias voltage from about −100 V. The specified bias voltage was applied to the target for 20 min after the presputter process. After etching process, the etching depth of the wafer was measured by a surface roughness tester (Taylor Hobson, Form Talysurf Super S5K), and the etching rate was calculated by dividing the etching depth by the processing time. The voltage applied to the target and current flowing through the electrodes were measured by a high voltage probe (Tektronix, P-5100) and current monitor (Pearson, model 110A), respectively. The electron temperature and the ion density were obtained by floating double probe measurements. The probe tip was a cylindrical tungsten electrode (ϕ 0.4) with an exposed length of 3 mm and a tip-to-tip distance of 8 mm. The measurement position of the probe was 70 mm from the coil edge. Electron energy distribution function was assumed as Maxwellian[5].

3. Results and Discussion

Figure 2 shows the typical waveforms of the coil voltage and coil current, and the time evolution of the effective power Ar/CF_4 discharge. The waveform was divided into 3 stages (I) ~ (III) as shown in Figure 2. In Ar/CF_4 discharge, the plasma was ignited at 40 μs (stage (II)). The peak values of coil voltage and current before the plasma ignition (stage (I)) were approximately 3.4 kV and 39 A, respectively. The impedance calculated from the amplitude of the coil

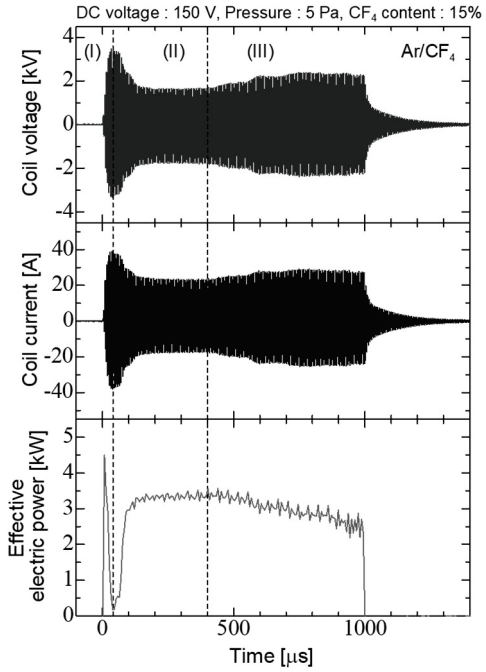

Fig.2 Typical waveform of the coil voltage, coil current, and the time evolution of the effective electric power.(I) before discharge, (II) constant discharge, (III) discharge

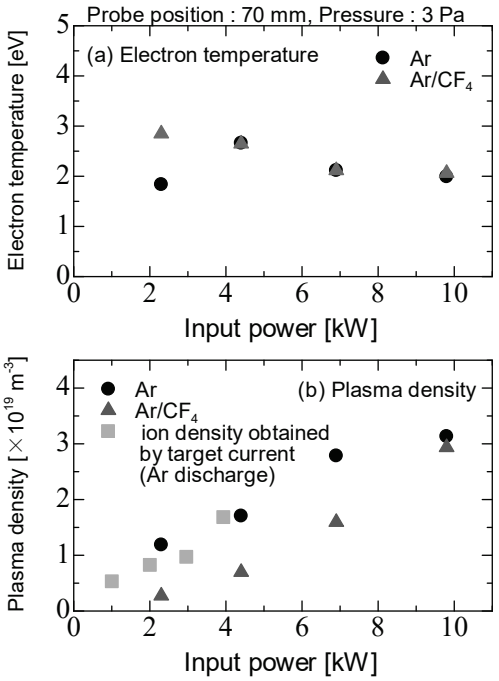

Fig.3 Plasma parameters as a function of input power. (a) Electron temperature and (b) plasma density for Ar and Ar/CF_4 discharges.

voltage and current was about 87 Ω, which was almost equal to the impedance of the induction coil of 83 Ω. After the plasma ignition (stage (II)), the coil voltage and current decreased to 1.7 kV and 21 A, respectively. When the plasma was generated, a transformer, where the plasma was regarded as the secondary winding was coupled between the coil and the plasma, and the impedance changed. The impedance at this time was approximately 81 Ω. After the time of 400 μs (stage (III)), the coil voltage and current increased again to approximately 2.2 kV and 26 A, respectively. This trend of time evolution was also observed in the Ar discharge. The effective power was 3 kW in Ar/CF_4 discharge.

Figure 3 shows (a) the electron temperature (T_e) and (b) plasma density (n_p) of Ar and Ar/CF_4 discharges as a function of the input power. The target electrode was not placed in the chamber. The probe measurement position was 70 mm from the coil edge. Figure 3 also shown the ion density calculated by the target current, which is obtained as following equation,

$$n_i = J/0.61eu_B \qquad (1)$$

where J is the target current density obtained from the measured target current I_t, u_B is Bohm velocity and e is an elementary charge. The electron temperature is 2–3 eV and is not affected by gas species. In conventional ICP, the electron temperature is around 3.5 eV[6,7], and this ICP is almost equal to the conventional value. The plasma density increases with the input power, and is on the orders of 10^{19} m^{-3} in Ar discharge, and 10^{18} m^{-3} in Ar/CF_4 discharge. In conventional ICP, the plasma density is on the orders of 10^{17}–10^{18} m^{-3} in Ar discharge, and 10^{16} m^{-3} in Ar/CF_4 discharge[1,8]. In this ICP, it was 10 to 100 times higher than the conventional ICP. Therefore, it is expected to be applied to high-speed processes. The plasma density in the Ar/CF_4 discharge is lower than that in Ar discharge because of electron loss due to electron attachment to various kinds of molecules[8].

Figure 4 shows the target current for (a) Ar discharge and (b) Ar/CF_4 discharge at each input power. The burst

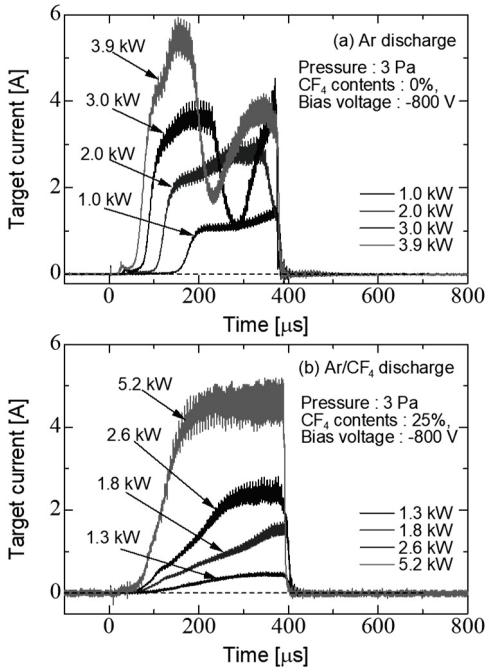

Fig.4 Waveform of target current at each input power. (a) Ar discharge and (b) Ar/CF_4 discharge.

width was set to 400 μs in order to reduce the arcing at the target electrode and make the process stable. The input power increased, the maximum value of the target current became larger, and the time to ignite plasma and the rise time of the target current became shorter, because the high-energy electrons increased with input power, which accelerated the ionization. In addition, a large change in the target current was observed at 3.0 kW and 3.9 kW in the Ar discharge. It is though that the change of plasma impedance is one of the reasons. However, more study is needed to clarify the detail of the mechanism.

Figure 5 shows the etching rate for Ar and Ar/CF_4 discharges as a function of the input power. The etching rate by Ar discharge was much smaller than Ar/CF_4 discharge. Because in the etching in Ar discharge, the Ti target electrode was etched by argon ions, and fractions were deposited in the trench. The etching rate in Ar/CF_4 discharge increased with input power, and the maximum etching rate was 0.13 μm/min. In conventional ICP, the etching rate is 0.02–0.03μm/min[9]. In this ICP, the etching rate was faster

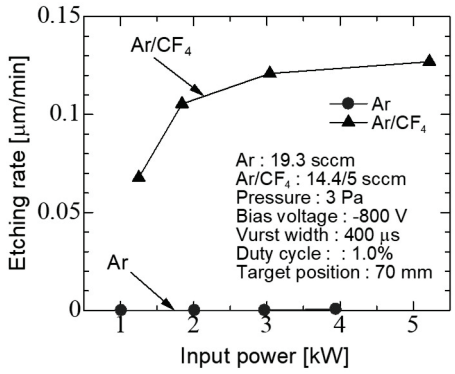

Fig.5 Input power characteristics of the etching rate for Ar discharge and Ar/CF_4 discharge.

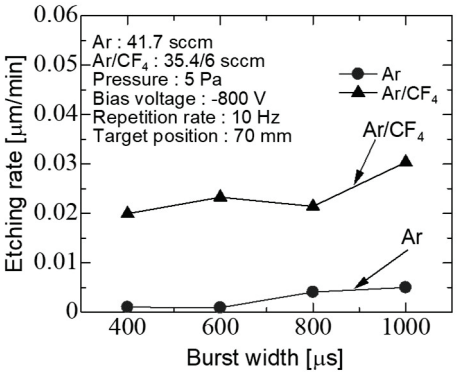

Fig.6 Burst width characteristics of the etching rate for Ar discharge and Ar/CF_4 discharge with fixed repetition rate (10 Hz).

than the conventional ICP. This is supported by the high density compared to the conventional ICP.

Figure 6 shows the etching rate for Ar and Ar/CF_4 discharges as a function of the burst width with a repetition rate of 10 Hz. The repetition was fixed, the input power per cycle was increased with burst width. In Ar and Ar/CF_4 discharges, the etching rate increased slightly with the increasing burst width and was about 0.005 μm/min in Ar discharge, and about 0.02–0.03 μm/min in Ar/CF_4 discharge. The etching rate in the case of Ar/CF_4 discharge was 4–6 times higher than that of Ar discharge.

Figure 7 shows the etching rate for Ar discharge and Ar/CF_4 discharge as a function of the burst width with a duty cycle of 1.2%. The duty cycle was fixed, the input power per cycle did not change. When the duty

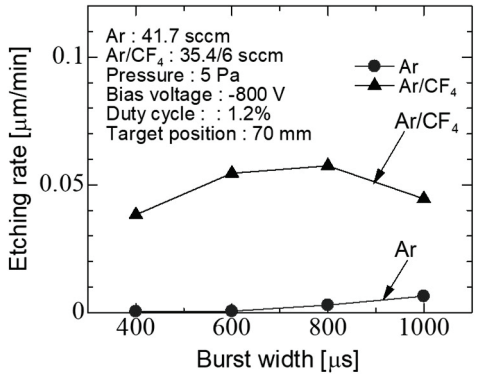

Fig.7 Burst width characteristics of the etching rate for Ar discharge and Ar/CF_4 discharge with fixed duty cycle (1.2%).

ratio was fixed, there was no significant change with the burst width, unlike when the repetition rate was fixed. Therefore, the etching rate is affected by the input power. The etching rate was about 0.005 μm/min for Ar discharge and 0.04–0.05 μm/min for Ar/CF_4 discharge.

4. Conclusions

The electrical characteristics and etching rates of the high-power burst Ar and Ar/CF_4 ICPs were investigated. The electrical characteristics was obtained by time-resolved measurements. The etching was operated in Ar and Ar/CF_4 discharges, and the effects of the power and burst width were investigated. It was found that during Ar/CF_4 discharge, about 3 kW was applied. It was confirmed that the coil current and voltage changed with the impedance. Double probe measurements showed that the plasma density in the etching area was in the order of 10^{18}–10^{19} m^{-3}, that the etching was performed under high density. The etching rate of the silicon wafer by Ar/CF_4 discharge (reactive ion etching) was larger than the Ar discharge (physical etching) and increased 0.05 μm/min with the burst width increasing at a constant repetition rate. At this time, since the duty ratio is 1.0%, a DC equivalent value of 5 μm/min could be obtained.

Acknowledgments

This research was supported by a Grant-in-Aid for Scientific Research (S), Grant Number 19H05611.

References

[1] U. Helmersson *et al*., "Ionized physical vapor deposition (IPVD): A review of technology and applications", *Thin Solid Films*., **513**, pp. 1–24 (2006).

[2] J. Hopwood *et al*., "Review of inductively coupled" *Plasma Sources Sci. Techno*., **1**, pp. 109–116 (1992).

[3] K. Yukimura *et al*., "Generation of RF plasma assisted high power pulsed sputtering glow discharge without using a magnetic field" *Nucl. Instrum. Methods Phys. Res. B*., **267**, pp.1701–1704 (2009).

[4] K. Yukimura *et al*., "High-power inductively coupled impulse sputtering glow plasma" *IEEE Trans. Plasma Sci*., **39**, pp. 3085–3093 (2011).

[5] T. Kimura et al., "Electron energy distribution detection in symmetrically driven rf argon discharge" *Jpn. J. Appl. Phys*., **32**, pp.3601–3605 (1993).

[6] M. A. Lieberman *et al*., *Principles of Plasma Discharges and Materials Processing*, 2nd ed., Wiley: New York, NY, USA (2005).

[7] J. Hopwood *et al*., "Electromagnetic fields in a radio-frequency induction plasma" *J. Vac. Sci. Technol*., **11**, pp. 147–151 (1993).

[8] A. M. Efremov *et al*., "Etching characteristics and mechanism of $Pb(Zr,Ti)O_3$ thin films in CF_4/Ar inductively coupled plasma" *Vacuum*., **75**, pp. 321–329 (2004).

[9] A. Kumar et al., "Optimizing the isotropic etching nature and etch profile of Si, Ge and $Si_{0.8}Ge_{0.2}$ by controlling CF_4 atmosphere with Ar and O_2 additives in ICP" *IEEE Trans. Semicond. Manuf*., **34**, pp. 177–184 (2021).

Characterization of Pulsed Forming Network Using Inductive Energy Storage

Shoma Watanabe, Taichi Sugai, Akira Tokuchi*, and Weihua Jiang

Extreme Energy Density Research Institute, Nagaoka University of Technology.

**Pulsed Power Japan Laboratory Ltd.*

ABSTRACT

IES type circuits can operate at low voltage and have the feature of charging with current. In this study, we propose an IES-PFN circuit as an improvement on the previous study [1]. Three operation tests, i.e., IES-PFN, IES-Blumlein PFN, and voltage superposition were conducted. In each test, the operation at low voltage of several tens of volts DC and the voltage superposition operation were confirmed.

Keywords

pulsed power, nanosecond pulsed power technology, inductive energy storage (IES), pulsed forming network (PFN), bulmlein pulsed forming network, pulsed voltage adding

1. Introduction

There is nanosecond pulsed power technology, where the pulse width is on the order of nanoseconds. Applications include water treatment, exhaust gas treatment, lasers, and sterilization. Each application has its own technical requirements for pulsed power such as compactness, high power, high efficiency, and high repetition rate, and researches have been conducted to meet these requirements.

Meanwhile, there are two methods of energy storage for pulsed power: capacitive energy storage (CES) and inductive energy storage (IES). As a comparison of the characteristics of each type of energy storage, CES uses a capacitor for the energy storage and a closing switch as a switch, while IES uses an inductance for the energy storage and an opening switch as a switch. CES uses voltage V in electric circuit and electric field E in electromagnetism as energy source, while IES uses current I and magnetic field H. The maximum energy density of IES is much higher than that of CES, with a theoretical difference of more than one order of magnitude. Thus, we have developed IES circuits.

Although the IES-PFL circuit was developed At a previous study[1], this has a long line to realize a long square wave, resulting in a large scale pulse source. In this study, we developed a nanosecond pulsed power generator using IES-PFN for compactness and confirmed the operation of a single module and a multi-stage module.

2. Pulsed Forming Network using Inductive Energy Storage

Figure 1 shows the circuit diagram of the IES-PFN. The operating principle of the circuit has three steps described below.

i) When the switch is turned on and all the inductances L are charged by current flowing from the external capacitor C through the diode on the right side. When the current reaches to a certain set current, the switch is turned off.

ii) When the switch is turned off, the capacitor C_n of the PFN is charged sequentially from the left side because there is no more current

path. The polarity of the charge is - at the top and + at the bottom. During this time, the current on the right side goes through the diode, so there is no output.

iii) At the moment when all the capacitors C are charged with the same voltage, there is no current anymore in the circuit and the PFN is charged as CES. After this moment, the PFN is discharged from the CES-charged PFN to the load matched by R=Z.

The main components used in the fabrication of the circuit are shown in Table 1. After the fabrication, three operational tests that are IES-PFN operation test, IES-Blumlein PFN operation test, and IES-Blumlein PFN operation test in a multi-stage module were conducted. The results of these tests are described in the next section.

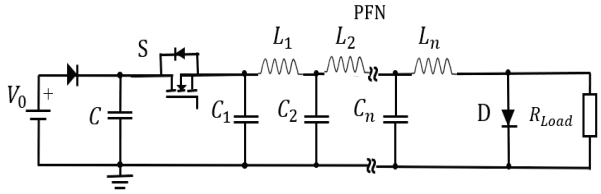

Fig. 1 The circuit of the IES-PFN

Table 1
The main components of the circuit

Component	Quantities and Specifications
Capacitor 1~n	Panasonic ECQE12102KF, 1 nF
Inductor	Handmade copper wire coil of ~100 nH
Switch	CREE C2M0025119D
Capacitor	KMG EKMG451ELL100MK20S, 10 μF

3. Experimental Demonstration

3.1 Experimental Demonstration of IES-PFN

The results of the IES-PFN, where the operation test was conducted at 34 V DC and 10 Ω matching load are shown in Fig. 2. When the switch is turned off, the current is cut off, indicating that the device is operating as an IES. The output of the load was obtained with a voltage of 469 V, a current of 46.8 A, a pulse width of 110ns, a rise time of 10.1ns, and a voltage on the switch of 952 V. The pulse width and rise time of the simulated values were 100 ns and 8.00 ns, respectively, so that there was a slight difference in the pulse width and rise time. The cause of this difference is the parasitic inductance in the circuit. Although there were some deviations, we were able to confirm the operation of the IES-PFN at a low voltage of 34 V DC.

3.2 Experimental Demonstration of IES-Blumlein PFN

The circuit diagram and waveforms of IES-Blumlein PFN are shown in Fig. 3 and 4, respectively. 29 V DC and 5 Ω matching load was used for the operation test. When the switch is turned off, the current is cut off, indicating that the device is operating as an IES. The output voltage of the load was 454 V, the current was 90.8 A, the pulse width was 111 ns, the rise time was 11.2 ns, and the voltage across the switch was 908 V. The simulated output load voltage was 500 V, the load current was 100 A, the pulse width was 100 ns, the rise time was 8.00 ns, so that there were some differences in the pulse width and rise time, and the output peak. The cause of this is thought to be the effect of parasitic inductance and loss in the circuit. Although there were some deviations, we were able to confirm the operation of the IES-Blumlein PFN at a low voltage of 29 V DC.

3.3 Experimental Demonstration of Voltage Adding

The circuit diagram and waveforms of the three-stage IES-Blumlein PFN are shown in Fig. 5 and 6 respectively. The operation test was conducted with 87 V input DC voltage and a matching resister. Fig.6 also includes waveform, for one and two stages with a resister depending on the number of modules. When the switch is turned off, the current is cut off and the device operates as the IES. From the waveform of the switch voltage of each stage, we can see that each stage operates independently without interference. The output voltage of the load is 452 V (1module), 901 V (2module), 1343 V (3module), the pulse width is 110 ns, the rise time is 11.3 ns, and the

voltage applied to the switch is 909V. The output load voltage of the simulated values are 500 V (1module), 1000 V (2module), and 1500 V (3module) which are higher than the experiment. We believe that this is caused by parasitic inductance and losses in the circuit. Although there were some deviations, we were able to confirm that the voltage superposition operation was generally in accordance with the number of modules without interference in each stage independently at a low voltage of 87 V DC.

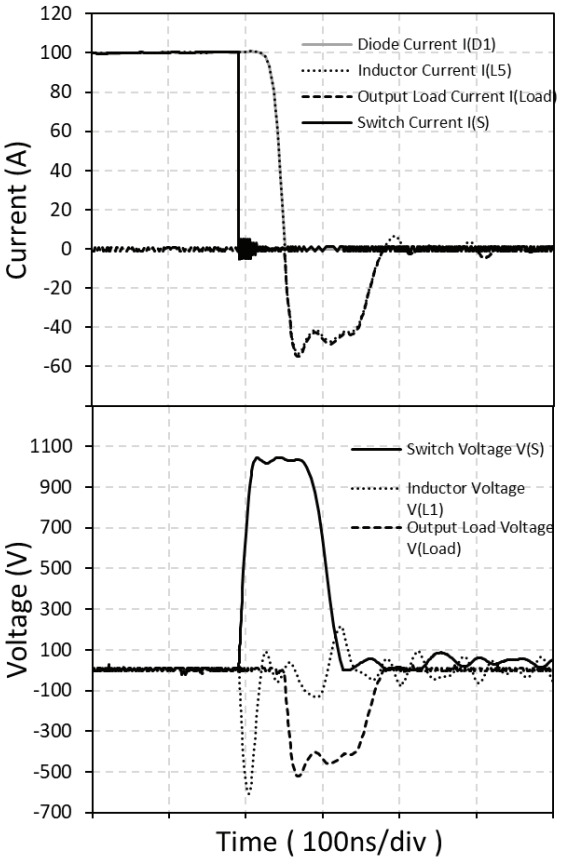

Fig. 2 The experimental results of the IES-PFN

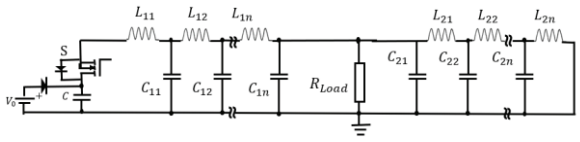

Fig. 3 The circuit of the IES-Blumlein PFN

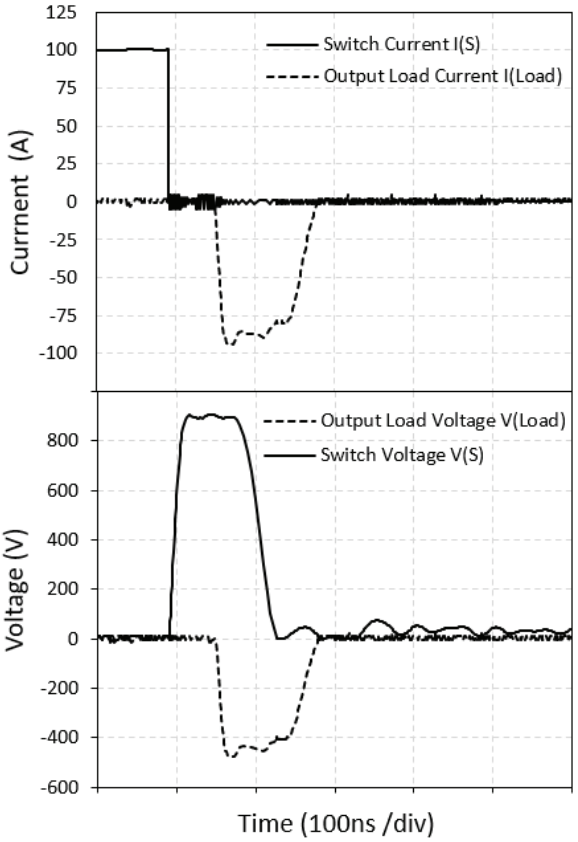

Fig. 4 The experimental results of the IES-Blumlein PFN

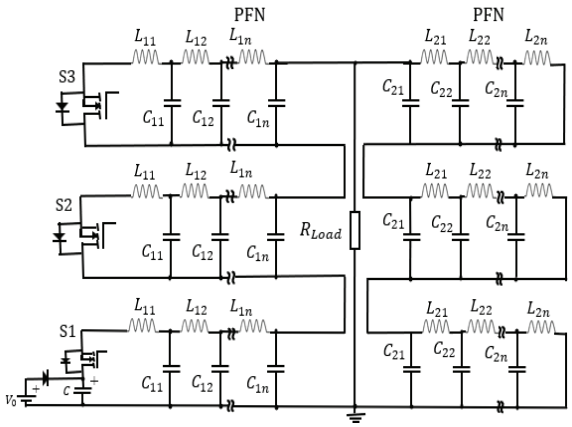

Fig. 5 The circuit of the voltage adding

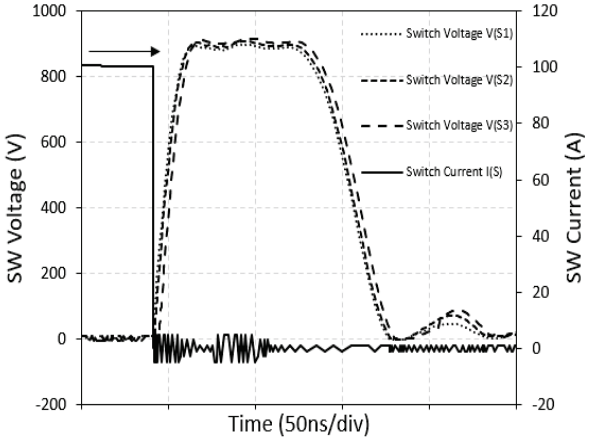

(a) Voltage waveforms for each switch and switch current waveform

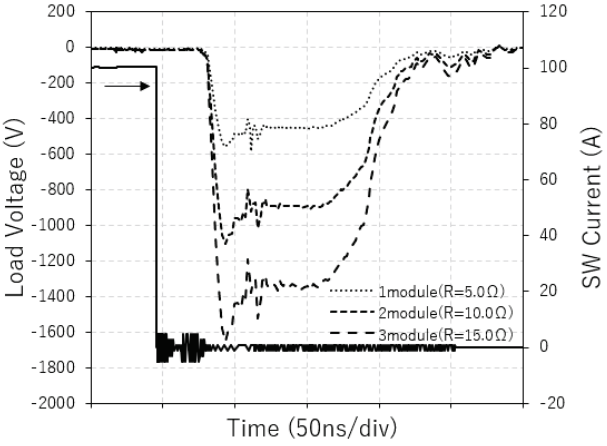

(b) Voltage Adding waveform for each module

Fig. 6 The experimental results of Voltage Adding

4. Conclusions

In this study, IES-PFN is developed and three operation tests were conducted. At the first test, the operation of the IES-PFN at a low voltage of 34 V DC was confirmed. At the second IES-Blumlein PFN operation test, IES-Blumlein PFN operation at a low voltage of 29 V DC was confirmed. At final test of multi-stage, we were able to confirm the voltage superposition operation according to the number of modules without interference at a low voltage of 87 V DC.

At next work we plan to conduct operation tests by increasing the number of stages to 5 and 10.

References

[1] Liang Yu, Zezheng Jiu, Taichi Sugai, Akira Tokuchi, and Weihua Jiang, “Pulsed Voltage Adder Topology Based on Inductive Blumlein Lines,” *IEEE Trans. Plasma Sci.*, vol. 46, no. 5, pp.1816–1820 (2018).

Regeneration Rate Improvement and Loss Reduction in Resonant Charge Pulsed Power Circuits

Naoya Okamura, Kazuki Nagao, Taichi Sugai, Akira Tokuchi*, Weihua Jiang

Extreme Energy-Density Research Institute,
Nagaoka University of Technology

** Pulsed Power Japan Laboratory Ltd.*

ABSTRACT

The purpose of this study is to develop a resonant-charge pulse power supply. The conventional resonant-charge pulsed power circuit has a problem of poor regeneration rate, making high repetition rate operation impossible. In this study, we designed and tested a new resonant-charge pulse power circuit in which the power supply and capacitor are in series, to improve regeneration rate. As a result, a high repetition rate of 500 kHz and a regeneration rate of 100 % were achieved.

Keywords

Pulsed Power, Resonant Charge, regeneration rate, high repetition rate

1. Introduction

A resonant-charge pulse power supply is required for a power supply to a capacitor load.[1] The schematic diagram of the circuit and output waveform of the resonant-charge pulsed power supply are shown in Figs. 1 and 2, respectively. The features of the resonant-charge pulse power supply are that the output voltage is at most twice the input voltage, the pulse width can be adjusted by the timing difference between a charge switch and a regenerative switch, and the rise time of the output voltage depends on the sine half-wave time of the current. However, actual voltage is not twice the input voltage due to the element loss in the circuit, and is also remained voltage in C_2 exist even after regeneration (cf. Fig. 3), which makes high repetition operation impossible (cf. Fig. 4). In this study, we developed new circuit topologies to solve the problems.

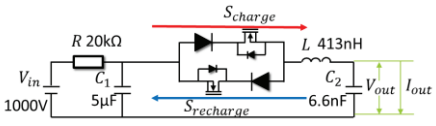

Fig. 1 Resonant charging circuit

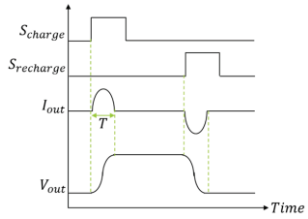

Fig. 2 Schematic of output waveforms

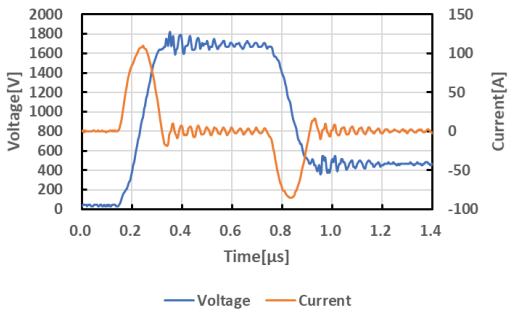

Fig. 3 Output waveform (1 shot)

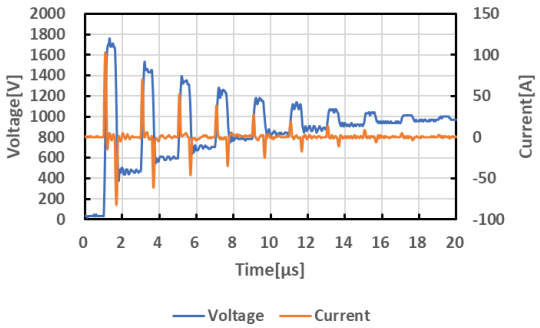

Fig. 4 Output waveform (10 shot, 500 kHz)

2. Experimental Setup

We developed two circuit topologies. One is a type with a discharge section and the other is a type with capacitors connected in series. The detail is as follow.

2.1 Circuit with a discharge section

A schematic circuit diagram and output waveform of the type with a discharge section are shown in Figs. 5 and 6, respectively. Table 1 shows the experimental conditions of that. Operating principle of the circuit is as follow. Initially, the voltage discharged from the C_1 is charged to the load capacitor C_2 through the charging switch. Then, the charged C_2 voltage is regenerated to the C_1 via the regenerative switch. Finally, the voltage remaining in the C_2 is discharged via a discharge switch to drop it to zero.

Table. 1 Experimental conditions

Pulse width	
Charge switch	**200ns(delay=0ns)**
Discharge switch	**200ns(delay=600ns)**
Recharge switch	**500ns(delay=1000ns)**

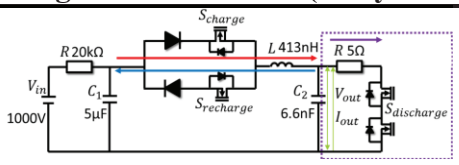

Fig. 5 Circuit with a discharge section

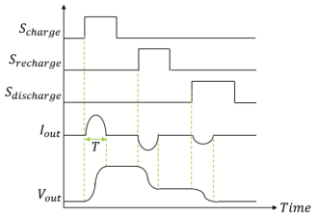

Fig. 6 Schematic of output waveforms

2.2 Series capacitor circuit

A schematic circuit diagram of the type with serial capacitors is shown in Fig. 7 and its experimental condition is shown in Table 2. The operating principle of the circuit is as follows. Initially, capacitors C_1 and C_3 are charged from power supplies V_{in1} and V_{in2}. Then, the voltage charged to the capacitors C_1 and C_3 is discharged to the load capacitor C_2 through the charge switch. Finally, the voltage charged to the C_2 is discharged to the capacitor C_3 through the regenerative switch. In this circuit, when regenerating from the load capacitor C_2 to the capacitor C_3, the voltage of C_3 is important to regenerate all the voltage of C_2. From experimental tests, the voltage was decided to V_{in1}=380 V and V_{in2}=620 V.

Table. 2 Experimental conditions

Pulse width	
Charge switch	**200ns(delay=0ns)**
Discharge switch	**200ns(delay=600ns)**

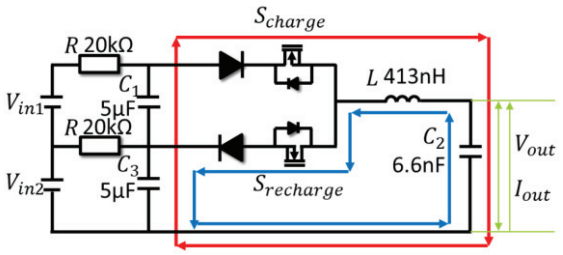

Fig. 7 Series capacitor circuit

3. Results and Discussion

3.1 Circuit with a discharge section

The measurement results of the output voltage and current waveforms of the resonant charging pulse power circuit with the discharge section are shown in Figs. 8 and 9. Table 3 shows the results of determining the amount of charge on the load capacitor C_2 from the output current waveform in Fig. 8. It is confirmed that output at a high repetition rate of 500 kHz becomes possible since the remained charge of C_2 is discharged. A remained problem with this circuit is that the residual charge of the load capacitor results in losses.

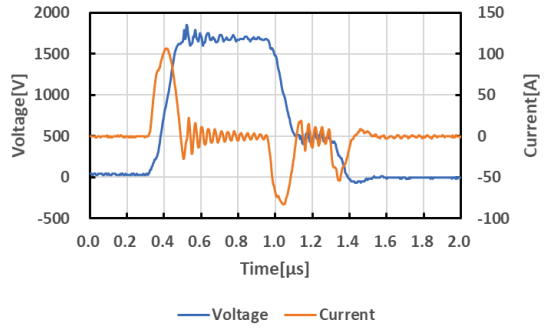

Fig. 8 Output waveform (1 shot)

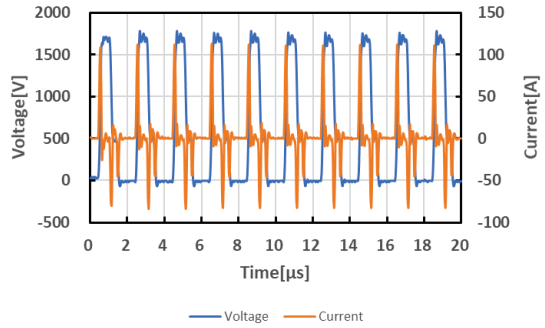

Fig. 9 Output waveform (10 shot, 500 kHz)

Table. 3 Amount of charge on load capacitor C2

Amount of charge	
During charge	11.8μC
During recharge	8.5μC
During discharge	3.3μC
Recharge rate	72.0%
Discharge rate	28.0%

3.2 Series capacitor circuit

The measurement results of the output voltage and current waveforms of the type with serial capacitors are shown in Figs. 10 and 11. Table 4 shows the results of determining the amount of charge on the load capacitor C_2 from the output current waveform in Fig. 10. It is confirmed output pulse at high repetition rate of 500 kHz with a charge regeneration rate of 100 % is possible.

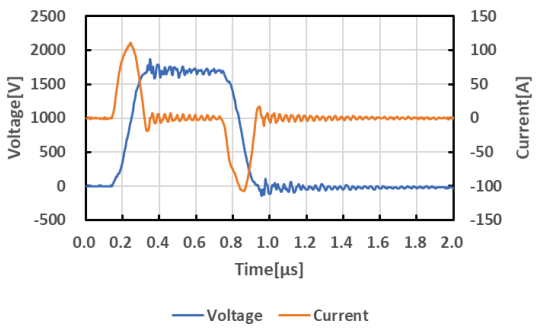

Fig. 10 Output waveform (1 shot)

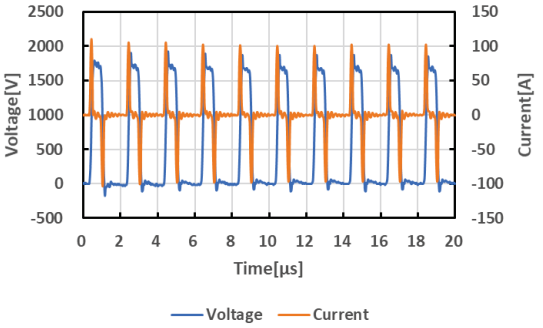

Fig. 11 Output waveform (10 shot, 500 kHz)

Table. 4 Amount of charge on load capacitor C2

Amount of charge	
During charge	12.3μC
During recharge	12.3μC
Recharge rate	100%

3.3 Losses in the circuit

The voltage and current across the elements for the charge and the regeneration, and across the discharge section in the type with the discharge section are shown in Figs. 12 to 14. Table 5 shows the power dissipation of the circuit calculated from the voltage and current waveforms. The voltage and current across the charging and regenerative elements of the type with serial capacitors are shown in Figures 15 and 16. The losses of the circuit calculated from the voltage and current waveforms are shown in Table 6. As the result, the type with serial capacitors caused higher loss than the type with the discharge section. This is because the voltage across the element for the regeneration increases due to the input voltage dividing by series connection of capacitors.

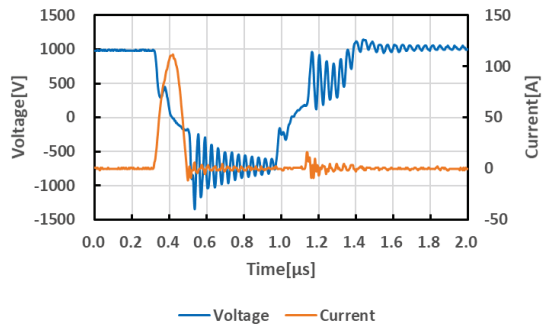

Fig. 12 Voltage and current between charging device

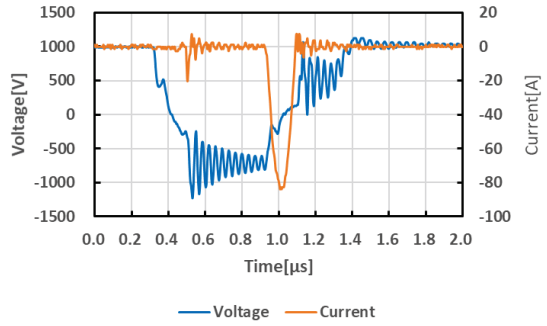

Fig. 13 Voltage and current between recharging device

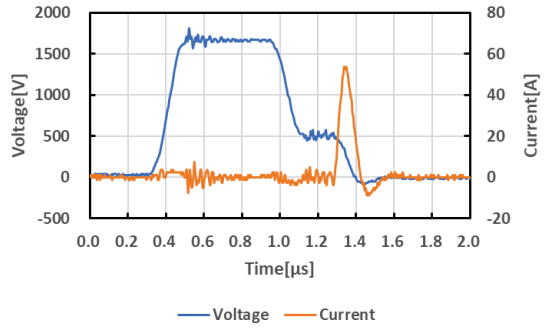

Fig. 14 Discharge part voltage and current

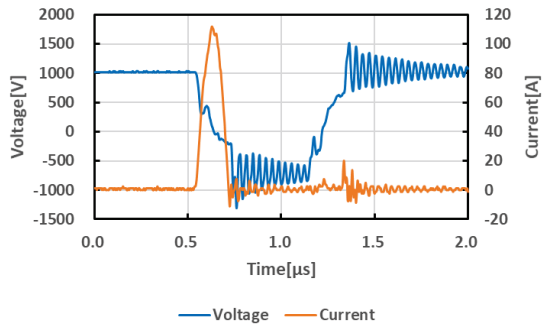

Fig. 15 Voltage and current between charging device

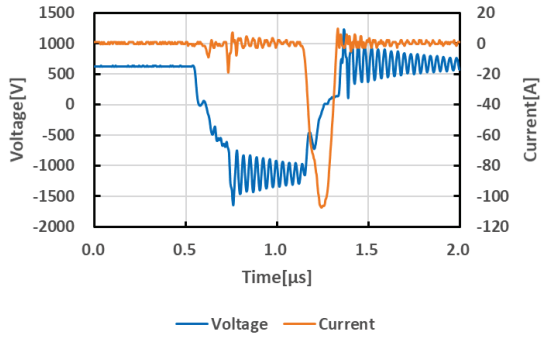

Fig. 16 Voltage and current between recharging device

Table. 5 Loss in the circuit

Loss	
charging device	1.94mJ
rechargeing device	1.00mJ
discharge part	1.05mJ
Total	3.99mJ

Table. 6 Loss in the circuit

Loss	
charging device	2.06mJ
rechargeing device	3.16mJ
Total	5.22mJ

4. Conclusions

4.1 Circuit with a discharge section

・An operation with a high repetition rate of 500 kHz is available since the voltage drops to 0 V after the pulse output.

・The energy of the load capacitor can't be fully utilized, resulting in losses.

・The circuit became larger due to the increase in the number of elements.

4.2 Circuit with a serial capacitor

・An operation with a high repetition rate of 500 kHz is available since the voltage drops to 0 V.

・Confirmed that all the charge on the load capacitor was regenerated.

・Confirmed that the loss of the circuit was 1.23 mJ larger than that of the circuit with a discharge section.

References

[1] K YATSUI et al, "Pulse Electromagnetic Energy Engineering", The Institute of Electrical Engineers of Japan, pp.42-45(2002).

Development of high voltage pulse generator using Semiconductor Opening Switch and LC circuit

Masahiro Moriizumi, Makoto Obata, Shintaro Tokutake, Taichi Sugai, Akira Tokuchi*, Weihua Jiang

Nagaoka University of Technology

**Pulsed Power Japan lab*

ABSTRACT

Recently, a special element called Semiconductor Opening Switch (SOS) is used to generate pulsed power. In order to improve the output of the pulse power supply using SOS and clarify the characteristics of SOS itself, we built and evaluated a pulse power supply using SOS and LC inverting circuit. As a result, an output of -33kV and a rise time of 25ns was obtained with the created power supply. In addition, as a result of the evaluation, it is considered that further output improvement can be obtained by increasing the residual carriers of SOS or increasing the applied reverse voltage.

Keywords

Key Words : pulsed power, high voltage, semiconductor opening switch, inductive-energy-storage, lc circuit

1. Introduction

Pulsed power is a technique that obtains extremely large power by releasing the stored energy in an extremely short time [4]. There are various energy forms of pulsed power. Especially, in applications such as water treatment, exhaust gas treatment, food and material processing and laser excitation, required waveforms are fast rise time, short pulse width, and high repetition rate. In recent years, to satisfy the requirements, a special element called Semiconductor Opening Switch: SOS is studied to generate pulse power [1]-[3]. However, the SOS characteristics and the circuit method for effectively utilizing them has not been unclear. This paper introduces the development of a pulse power supply that can generate a short pulse width and high voltage using SOS, the characteristics of SOS using it, and a circuit improvement plan.

2. Experimental Setup

2.1 Semiconductor Opening Switch

A semiconductor open switch (SOS) is a device developed for generating pulsed power. SOS is a type of diode, but its behavior during reverse recovery is unique. Since ordinary diodes are used for rectification, they are designed to minimize the current flowing in the opposite direction. However, when a voltage is applied to SOS in the reverse direction, immediately after the number of residual carriers increases with the forward current the residual carriers flow as a reverse current. After that, a depletion layer is formed and rapidly insulated. This reverse current and the transition to insulation are used as an open switch [4].

2.2 Experimental Circuit

The Fig. 1 is a circuit diagram of the high voltage pulse generation circuit created this time.

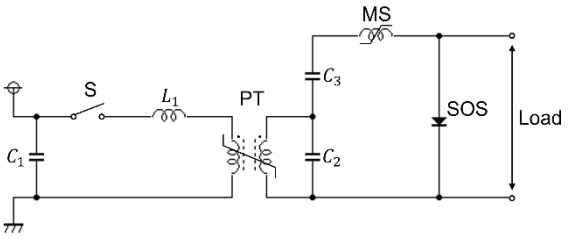

Fig. 1 Experimental circuit

First, if S is turned on after C1 is charged, it is boosted by the pulse transformer with turn ratio of 2:20 and charged to C2 and C3. At this time, a forward current flows through the SOS. As soon as charging is completed, the core of the pulse transformer is saturated, and the voltage of C2 is inverted by the secondary inductance of the pulse transformer. At the timing when the voltage of C2 is inverted, the magnetic switch MS is reversed, and the reverse voltage of C2 and C3 is applied to SOS. At this time, the residual carriers of SOS flow in the circuit and inductive energy is accumulated. After that, the SOS shifts to the isolated state, resulting in a high-voltage pulse output at the load [2], [4], [5].

3. Results and Discussion

3.1 Operation check

The Fig. 2 shows the result of a pulse output at a load of 15 kΩ in the built circuit.

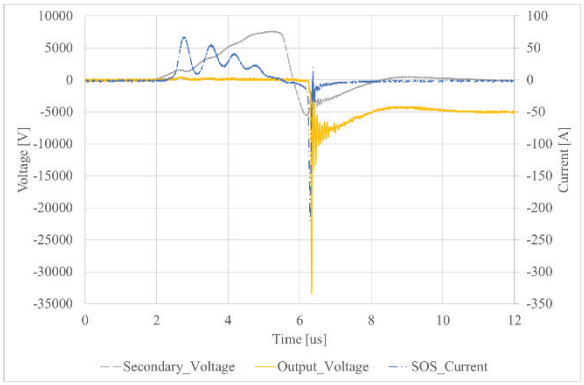

Fig. 2 Each waveform during operation

From the experiment, it was found that the circuit can obtain a maximum output voltage of -33 kV with a rise time of 25 ns. It was also confirmed that a voltage of several kilovolts remained after the pulse output. When this waveform is evaluated in detail, it can be seen that the reverse current of SOS flows after the voltage of C2 (secondary voltage) is inverted by the action of the magnetic switch. It is considered that the reverse voltage caused the steep reverse current resulting in the sharp output voltage. Further, the voltage remaining after the pulse output is considered to be due to the voltage remaining in C2 and C3.

3.2 Characteristics due to circuit inductance

The Fig. 3 shows the output voltage waveform when the inductance in the secondary circuit is changed. From this figure, it can be confirmed that the pulse width increases as the inductance in the circuit increases. The Fig. 4 shows the current flowing through the SOS at this time. From this figure, it can be seen that as the inductance in the circuit increases, the peak of the current decreases and the time required to cut off current also increases. From this, it is considered that the inductance in the circuit reduces the di / dt of the flowing current and increases the width of the output voltage [5].

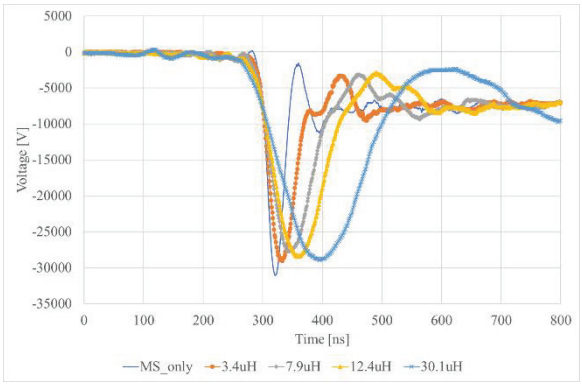

Fig. 3 Output voltage waveform at each inductance

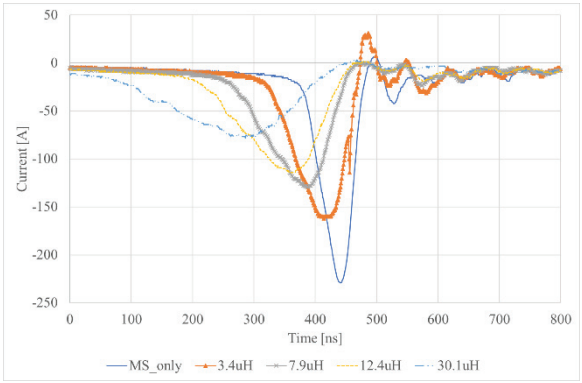

Fig. 4 SOS reverse current at each inductance

In addition, the Fig. 5 shows the amount of electric charge of forward and reverse current. From this figure, it can be seen that the amount of residual carriers is constant regardless of the waveform of the reverse current, which is extremely small as compared with the amount of forward charge. From these results, it is considered that increasing the residual carriers and

pulling out quickly contributes to the improvement of output.

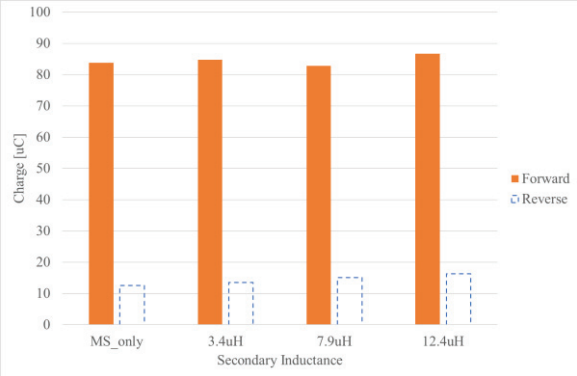

Fig. 5 Amount of SOS charge in the forward and reverse directions

3.3 Load characteristics

The Fig. 6 shows the output voltage waveform when the resistance value of the load is changed. From this result, it can be seen that when the load becomes small, a fast rise and a high voltage cannot be obtained.

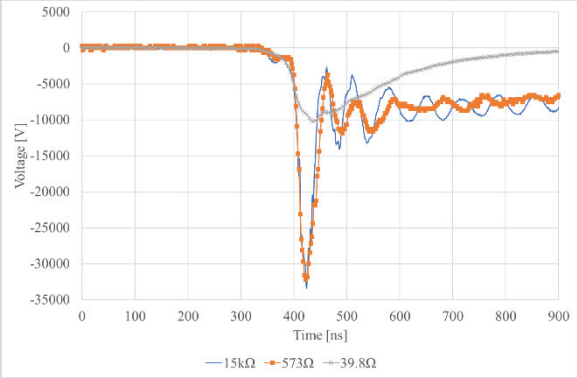

Fig. 6 Output voltage waveform at each resistance value

4. Conclusions

From the results of this experiment, it is considered that further performance improvement is possible depending on the current flowing through the SOS and the applied voltage. For example, if a higher voltage can be applied when extracting the residual carriers of SOS, the extraction speed can be increased, resulting in higher di / dt and output voltage of higher peak and faster rise time. Furthermore, efficiency improvement can be expected by selecting the inductance and capacitor to be used according to the characteristics of SOS.

In future, optimal voltage and current for forward pumping and reverse sweep will be investigated for further improvement.

References

[1] Weihua Jiang, “Pulsed High-Voltage Generator using Semiconductor Opening Switch”, *IEEJ Transactions.*, 130, 6, pp.538-542(2010).

[2] S. N. Rukin, “Pulsed power technology based on semiconductor opening switches: A review”, *Review of Scientific Instruments.*, 91, 011501(2020).

[3] Taichi Sugai et al., “Influence of a Circuit Parameter for Plasma Water Treatment by an Inductive Energy Storage Circuit Using Semiconductor Opening Switch”, *IEEE Transactions on plasma science*, 41, 4, pp967-974(2013).

[4] Koichi Takaki et al., “High voltage pulse power engineering”, *RIKOH TOSHO CO., LTD.*, 2018.

[5] Saburo Adachi, Shigeo Ohnuki, “Electromagnetism”, *MORIKITA PUBLISHING CO., LTD.*, 2014.

Characterization of Magnetic cores in pulsed power generation circuits

Makoto Obata, Yuki Okazaki, Masahiro Moriizumi, Taichi Sugai, Akira Tokuchi*, Weihua jiang

Nagaoka University of Technology

*Pulsed Power Japan Laboratory Ltd.

ABSTRACT

The spiker-sustainer circuit is a discharge excitation circuit for excimer lasers. In this circuit, it is necessary to provide an isolation element to suppress the leakage current. Therefore, in this study, a magnetic switch using RT cores was employed as the isolation element. To implement the magnetic switch, the characteristic of RT core was evaluated, and the result of $\Delta B_{\mathrm{sat.}}$ was 1.14T, the VT product was 132μVsec., $\mu_{\mathrm{sat.}}$ was 2.70×10^{-4} H/m, and t $\mu_{\mathrm{unsat.}}$ was 5.57×10^{-2} H/m. Based on the results, we designed magnetic switches and confirmed that the target values of leakage current, rise time, etc. were achieved.

Keyword

pulsed power, excimer laser, magnetic core, spiker-sustainer circuit

1. Introduction

1.1 Excimer lasers

Excimer lasers is laser that uses a mixed gas of noble gases and halogen gases, and oscillates when the excimer formed in the excited state falls to the ground state due to stimulated emission. In the ground state, the noble gases and the halogen dissociate due to weak bonding.

High-density power excitation is essential for excimer lasers. The spatial power required for oscillation is ~MW/cm^3 which is tens of thousands of times larger than that of a CW carbon dioxide laser. This is because lifetime of excimer extremely short [1].

1.2 Discharge excitation

The important things about the discharge excitation methods are that the laser gas at several atmospheres must be excited by a spatially uniform glow discharge in a very short time. At this method, there are divided two types of excitation: electron beam controlled discharge excitation and self-sustained discharge excitation. The latter method requires a short pulse and low inductance circuit system that applies a pulse voltage to the discharge gap with a short time width and a fast rise time.

1.3 Spiker-Sustainer circuit

The spiker-sustainer circuit is known as a discharge excitation circuit with high oscillation efficiency and large output power. First, in this circuit, a high-voltage pulse is output from the spiker circuit to lower the impedance of the discharge load. After breakdown, excitation energy is injected from the sustainer circuit which is matched with the impedance of the load [2].

However, if different sources of a spiker and a sustainer are connected to a discharge load such a Fig. 1, leakage current flows from the spiker side to the sustainer side, so that it is necessary to implement an isolation element between the two circuits. On the other hand, the element is also necessary to have a low impedance when energy is injected from the sustainer.

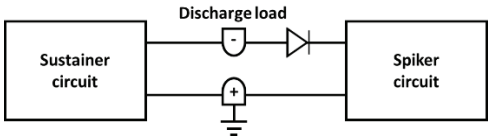

Fig. 1 Spiker-sustainer circuit

1.4 Purpose of research

To realize the element satisfying above, we adopted a magnetic switch as the isolation element. By making magnetic flux of a core saturate, energy from the sustainer can be injected efficiency due to the low inductance, but leakage current by the spiker, which is a direction opposite to the sustainer current, can be suppressed due to high inductance.

To implement the magnetic switch, it is essential to evaluate the characteristics of the magnetic core and select the appropriate inductance value. Thus, we evaluated the characteristics of the core and selected the number of turns and cross-sectional area to design a magnetic switch with appropriate inductance.

2. Experimental setup

2.1. Racetrack core (RT core)

In this study, a magnetic core in the shape of a racetrack is used. The general shape and specific dimensions of the RT core are shown in Fig. 2 and Table 1. The reason for using this core is that it has a shape that matches the shape of the chamber electrode which has an elongated shape. In the case of a circular core, there is a problem that multiple cores need to be placed, which makes wiring difficult. On the other hand, in the case of RT cores, the number of cores can be reduced because they can be placed around the electrodes, making wiring easier. In addition, the sustainer capacitor can be placed along the core to ensure uniform discharge, and by winding the multiple coils along the core, the inductance is reduced due to parallelization, resulting in efficient energy injection from the sustainer circuit. However, it should be noted that the leakage current from the spiker side increases if the inductance for the sustainer reduces.

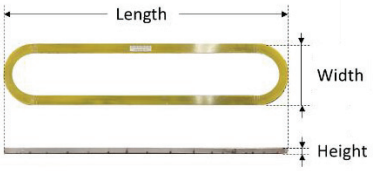

Fig. 2 Outline of RT core

Table 1 Dimensions of RT core

Item	Value
Length	593 mm
Width	130 mm
Height	7 mm
Magnetic length	1.267 mm
cross-sectional area	115.5 mm^2

2.2. Saturated inductance

The sustainer circuit targets an output current of 10kA and rise time of less than 100ns for the discharge load. The equivalent circuit and parameters of the sustainer circuit are shown in Fig. 3(a). From the circuit, the sustainer circuit can be regarded as RLC circuit, so the circuit parameters were substituted into the Equation (1.1), and the saturation inductance $L_{\mathrm{sat.}}$ was selected.

$$i(t) = \frac{V_{\mathrm{sus.}}}{L_{\mathrm{sat.}}\beta} e^{-\alpha t}\sin\beta t \tag{1.1}$$

$$\alpha = \frac{Z_{\mathrm{after\ dis.}}}{2L_{\mathrm{sat.}}} \tag{1.2}$$

$$\beta = \sqrt{\frac{1}{L_{\mathrm{sat.}}C_{\mathrm{sus.}}} - \left(\frac{Z_{\mathrm{after\ dis.}}}{2L_{\mathrm{sat.}}}\right)^2} \tag{1.3}$$

where $V_{\mathrm{sus.}}$ is the input voltage, $L_{\mathrm{sat.}}$ is saturation inductance, $C_{\mathrm{sus.}}$ is the sustainer capacitor, $Z_{\mathrm{after\ dis.}}$ is the impedance at discharge. The current waveform at 100nH of $L_{\mathrm{sat.}}$ is shown in

Fig. 4. From the Figure, it can be confirmed that output current and rise time are satisfied for the target value.

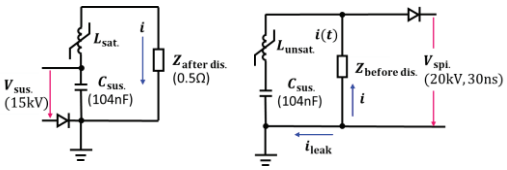

(a) sustainer circuit (b) spiker circuit

Fig. 3 Discharge load as seen from each circuit

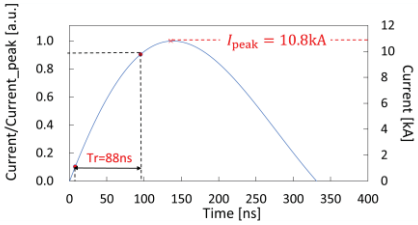

Fig. 4 Waveform of current at $L_{sat.} = 100\text{nH}$

2.3. Unsaturated inductance

The spiker circuit targets an output voltage of 20kV, a pulse width of 30ns, and a leakage current less than 50A. The circuit and parameters of the magnetic switch as seen from the spiker circuit is shown Fig. 3(b).

Substituting the parameters into the inductor voltage equation (2), we obtained the unsaturation inductance $L_{\text{unsat.}}$,

$$L_{\text{unsat.}} = \frac{V_{\text{spi.}}}{dI_{\text{Leak}}/dt} \tag{2}$$

where $V_{\text{spi.}}$ is the spiker voltage, I_{Leak} is the leakage current. As a result, it can be confirmed that the target value for leakage current is satisfied when $L_{\text{unsat.}} > 12\mu\text{H}$. In addition, the saturation VT product of 0.6mVsec. must also satisfied to prevent the magnetic core from being saturated by the spiker voltage.

3. Experimental result and simulation

3.1. Evaluation of magnetic properties of RT core

The measurement circuit shown in Fig. 5 was used to evaluate the $\Delta B - H$ characteristics of the RT core. As a measurement method, the voltage V_L and current I_L were measured and substituted into the equation (3),(4) to obtain the variation range of magnetic flux density ΔB and the magnetic field H.

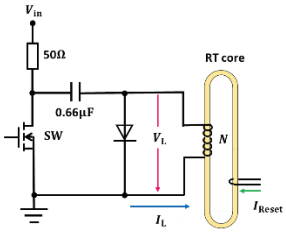

Fig. 5 Measurement circuit

$$\Delta B = \frac{1}{NS}\int V_L dt \tag{3}$$

$$H = \frac{NI_L}{l} \tag{4}$$

where N is number of turns, S is effective cross-sectional area, l is effective magnetic length. The result of the $\Delta B - H$ characteristics of the RT core are shown in Fig. 6. In the measurement, the number of turns N was set to 5, the reset current to 4.8A, and the pulse width to 5μs.

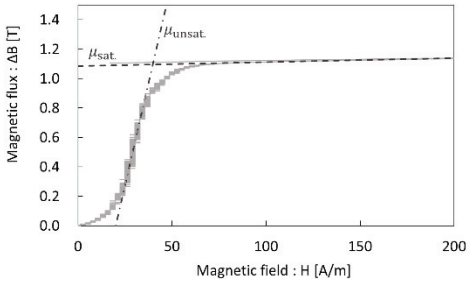

Fig. 6 $\Delta B - H$ characteristics of RT cores

Fig. 6 shows that the saturation magnetic flux density $\Delta B_{\text{sat.}}$ is 1.14T, the VT product is 132μVsec., the permeability at saturation $\mu_{\text{sat.}}$ is 2.70×10^{-4} H/m, and the permeability at unsaturation $\mu_{\text{unsat.}}$ is 5.57×10^{-2} H/m. It was confirmed that the inductance value at unsaturation is about 200 times higher than that at saturation.

3.2. Selection of the number of turns and number of RT cores in magnetic switches

Using $\mu_{\text{sat.}}$ and $\mu_{\text{unsat.}}$ obtained from the $\Delta B - H$ characteristics of RT cores, the number of turns and number of cores that satisfy the target value of saturation and unsaturation inductance were calculated. The results are shown in Table 2. Equation (5) was used to calculate the inductance.

$$L = \frac{\mu N^2 S}{l \times 20} \tag{5}$$

Note 20 in eq. 5 is the number of coils wound along the core, which we connected in parallel. Table 2 lists three options that satisfy the inductance target value. In the case of N=4, S=462 mm^2, the saturation VT product is larger than the others. In the case of N=5, S=231mm^2, the leakage current is larger than the others, but the rise time is the fastest. In the case of N=6, S=231mm^2, the rise time is slower, but leakage current is suppressed the most in these.

3.3. Simulation of magnetic switch

The designed magnetic switch was simulated by LTSPICE. The circuit used in the simulation is shown in Fig. 7. Fig. 7(a) shows the magnetic switch seen from the sustainer circuit, and Fig. 7(b) shows it seen from the spiker circuit.

The results of the simulation using these circuits are shown in Fig. 8. Fig. 8(a) shows the current waveform flowing in load R1 in the circuit of Fig. 7(a). Fig. 8(b) shows the leakage current waveform flowing in inductor L3 in the circuit of Fig. 7(b).

Table 2 Design results of magnetic switches

N [-]	S [mm^2]	$L_{\text{unsat.}}$ [μH]	$L_{\text{sat.}}$ [nH]	Sat. VT [mVsec.]	I_{Leak} [A]	Rise time [ns]
4	4	16.2	78.7	2.11	40.7	71.3
5	2	12.7	61.5	1.32	52.0	65.4
6	2	18.3	88.6	1.58	36.1	82.0

(a) sustainer circuit (b) spiker circuit

Fig. 7 Simulation circuit

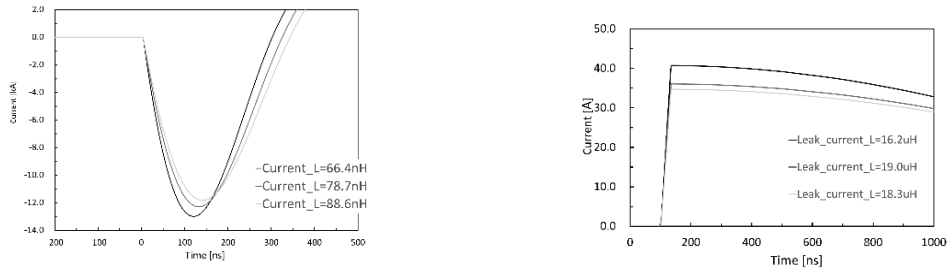

(a) Current waveform of discharge load (b) Waveform of leakage current

Fig. 8 Waveform of simulation

Table 3 shows the results of reading the peak current, pulse width, and rise time from Fig. 8(a). From the Table 3, it was confirmed that all the options satisfied the target value of 10kA load current and the rise time was within 100ns. In addition, the pulse width was found to be about 200ns.

Table 3 Simulation results of current

N [-]	S [mm^2]	I_{peak} [kA]	P.W. [ns]	R.T. [ns]
4	4	-11.7	195	71.3
5	2	-12.7	173	65.4
6	2	-11.3	240	82.0

Table 4 shows the results of reading the peak current in Fig. 8(b). the leakage current is about 50A for all the options. It was confirmed that all options satisfy the target value.

Table 4 Simulation results of current

N [-]	S [mm^2]	I_{Leak} [A]
4	4	40.7
5	2	52.0
6	2	36.1

4. Conclusions

In the spiker-sustainer circuit for the discharge excitation, it is necessary to implement an isolating element to suppress the leakage current. In this study, magnetic switch using RT cores was proposed. To design the magnetic switch, we evaluated the characteristics of the RT core. As the result, $\Delta B_{sat.}$ was 1.14T, the VT product was 132μVsec., the permeability at saturation was 2.70×10^{-4} H/m , and the permeability at unsaturation was 5.57×10^{-2} H/m. Using these results, we designed a magnetic switch and proposed three options that satisfy the target values. As a result of the simulation, it was confirmed that all the options satisfied the target values for current, rise time, and leakage current.

References

[1] H.Nagai, Laser process technology ~From basics to practice~ (in Japanese), Optronics Co.,Ltd. , 2000, p101-108

[2]Y.Sato, M.Inoue, K.Haruta, H.Nagai, High Power XeCl Laser with a Spiker-Sustainer Circuit – Characteristics of Repetitive Operation -, The Laser Society of Japan, 1991, p38-40

The effects of AC electric field on ice nucleation in the super-cooling of a liquid

Katsuyuki Takahashi*, Yota Sawada, and Koichi Takaki*

Faculty of Science and Engineering, Iwate University

**Agri-Innovation Center, Iwate University*

ABSTRACT

The effects of an AC electric field on ice nucleation temperature and nucleation rate were investigated by freezing distilled water while exposing it to varied AC electric field strengths and frequencies. To eliminate the influence of ion injections and electric field concentrations at a metal electrode surface on ice nucleation, distilled water filled in resin cuvettes are used as samples. The samples are exposed to AC electric field induced by parallel plate electrodes placed outside of the cuvettes. The cuvettes and parallel plate electrodes placed in a freezer with an inside temperature fixed at -15 ℃. The electric field strength in the sample is 2 or 7.5 kV/m and frequency varies from 50 Hz to 10 kHz. The ice nucleation temperature and the nucleation rate of distilled water increase with increasing the electric field strength and the frequency

Keywords

Electric field; ice nucleation; supercooling;

1. Introduction

Recently, freezing under an electric field has attracted attention as a technique for controlling ice nucleation in the freezing process. Because the molecules of water are dipolar, they orient themselves under an electric field such that the dipole moment aligns with the direction of the electric field. Furthermore, the oriented water mole-cules form clusters that form ice nuclei via hydrogen bonding [1,2]. Under an electric field, the Gibbs energy required for ice nucleation is smaller, and the ice nuclei form at a higher temperature compared to normal freezing; therefore, it is possible to make the size of the ice crystals formed during freezing small [3,4]. However, there is a research gap on factors such as the mechanisms for the effects of electric field treatment on the freezing of water, influence of frequency, etc. In addition, it has been reported that, when foods are frozen under an electric field, the sizes of ice crystals are smaller, the destruction of cells is suppressed, and the drip during thawing is reduced [3-6]. In general, it is preferable for supercooling and freezing of food to occur at lower temper-atures because the ice crystals are smaller. However, many experimental and numeri-cal studies have reported that supercooling is unlikely to occur and freezing starts at higher temperatures when an electric field is applied [7-18], which contradicts this result

This study investigates the effects of electric field strength and frequency on ice nucleation temperature, nucleation rate, and freezing time in the supercooling of a liq-uid under an AC electric field. To eliminate the influence of ion injections and electric field concentrations at a metal electrode surface on ice nucleation, distilled water filled in resin cuvettes are used as samples. The samples are exposed to AC

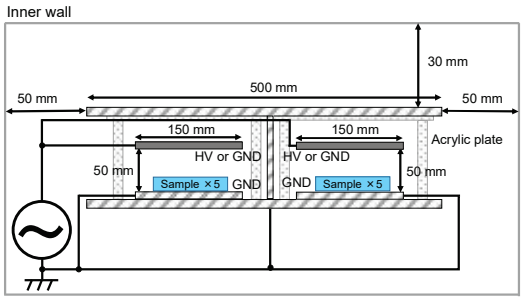

Figure 1. Schematic diagram of the electrodes inside freezer

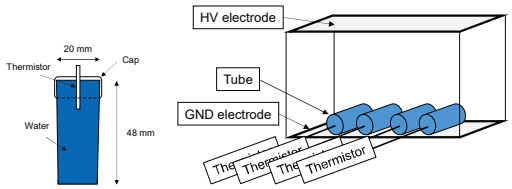

(a) (b)

Figure 2. Method of installing samples between the electrodes

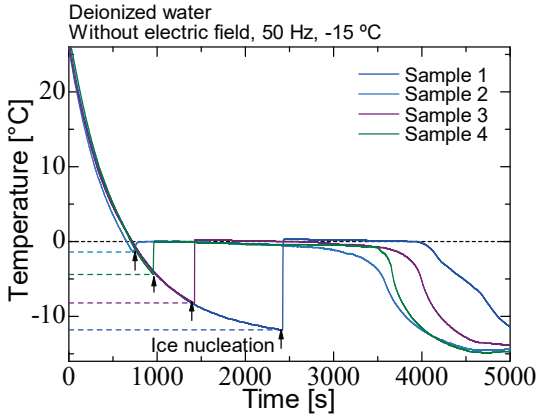

Figure 3. Examples of freezing curve

electric field in-duced by parallel plate electrodes placed outside of the cuvettes.

2. Experimental Setup

An external image of the freezer (FMU-204I, Fukushima Industries Corp.), which was used as the apparatus for freezing the samples and a schematic diagram of the electrodes inside, is presented in Figures 1. Two pairs of parallel-plate electrodes con-sisting of two metal plates positioned 50 mm apart, respectively, were installed inside the freezer. By connecting an AC power source (Trek, Inc., Model 615-10) or a high-voltage transformer to one upper electrode and earthing the other, an electric field was generated between the pair of electrodes on the right (Figure 1), and the sam-ples placed between this pair of electrodes were considered in the 'electric field appli-cation zone'. Because no electric field was generated between the pair of electrodes on the left (Figure 1), the space between this pair was considered the 'control zone'. An earthed metal plate was installed between the two pairs of electrodes to block the elec-tric field from entering the control zone.

Distilled water was used for the samples. 2 mL samples were placed into cylindri-cal cuvettes with capacities of 2 mL as shown in Figure 2 (a). To measure the ice nucle-ation temperature, a hole was made on the lid of the cuvette, and a 15 mm insertion was made with a thermistor (T&D Corporation, RTR-52A). The container was placed on its side—sample placement method shown in Figure 2 (b) —between the paral-lel-plate electrodes in the freezer, and it was frozen while an electric field was applied. The temperature inside the freezer was set to –15 °C, and each container had 20 sam-ples. Sine wave voltages with crest values of 2.5 kV and 10 kV at frequencies of 50 Hz–10 kHz and 50 Hz, respectively, were applied to the high-voltage electrode.

In this study, the ice nucleation temperature was taken as the temperature immediately before supercooling was released and the temperature increased rapidly as shown in figure 3. The freezing time was taken as the time from the start of thermal equilibrium to the time the temperature had dropped by 5 °C. Ice nucleation temperature and freezing time were evaluated by performing a t-test on the results of normal freezing and freezing under an electric field. The confidence level was taken as 95 % ($p < 0.05$). Additionally, the number of nucleations was represented using a histogram with a bin width of 1 °C, and the nucleation rate (R) at each bin temperature was

calculated using the following equation:

$$R(T_i) = \frac{r n_i}{\Delta T_i \left(\frac{n_i}{2} + \sum_{j>i} n_i\right)} \quad (1),$$

where r is freezing rate, °C/s; n_i is the number of nucleations in each bin; and ΔT_i is the bin width, °C. Because the nucleation rate is the number of ice nuclei formed per unit area, per unit time, the higher the nucleation rate, the smaller the size of the ice crystals formed during freezing. The effects of electric field strength at a frequency of 50 Hz and the effects of frequency at an electric field strength of 50 kV/m, respectively, on the nucleation temperature and nucleation rate of ice were investigated for each sample.

3. Results and Discussion

Figure 4 shows the results of analysing the electric field distribution between the electrodes using a 2-D electric field solver software (Ansoft Corporation, Maxwell II SV). It also presents that, at applied voltages of 2.5 kV and 10 kV, the strengths of the electric field acting on the samples were approximately 2 kV/m and 7.5 kV/m, respectively.

Figure 5(a) shows the ice nucleation temperature for distilled water at the respective electric field strengths. An increase in the electric field strength was accompanied by an increase in the ice nucleation temperature, and a significant difference ($p < 0.05$) from the control was obtained at all the conditions. Figure 5(b) shows the freezing time for distilled water at the respective electric field strengths. As the ice nucleation temperature increases, the heat of solidification emitted when supercooling is released is expected to decrease. However, the freezing time did not differ from the control under any of the conditions. Figure 6 shows the ice nucleation temperature for distilled water at the respective frequencies. An increase in the frequency was accompanied by an increase in the ice nucleation temperature, and a significant difference ($p < 0.05$) from the control was obtained at all the conditions.

Figure 7 shows the ice nucleation rate for distilled

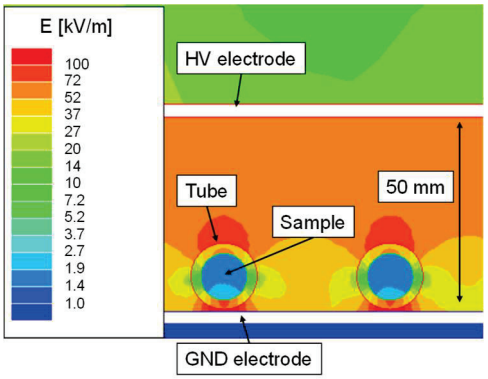

(a)

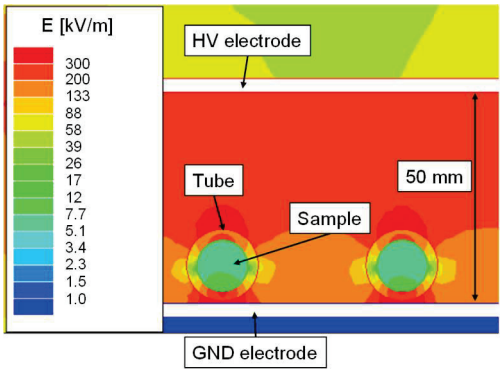

(b)

Figure 4. Electric field distribution between electrodes with applied voltages of (a) 2.5 kV and (b) 10 kV.

water at the respective (a) electric field strengths and (b) frequencies. At 50 kV/m and 200 kV/m, the nucleation rates were higher than those of the control in the high temperature zone, but lower at the low temperature zone; therefore, it is possible that the electric field application affects the freezing process after nucleation. The ice nucleation rate (R) [19,21] can be expressed in Equation (2).

$$R = J_0 \exp\left(-\frac{\Delta G^*}{k_B T}\right) \quad (2),$$

where J_0 is the frequency factor, s^{-1}; ΔG^* is the activation energy, J; and k_B is the Boltzmann constant, J/K. Based on this equation, the gradient of each linear approximation in Figure 7 represents the logarithm of the ratio of the activation energy to the Boltzmann constant, and the y-intercept represents the logarithm of the frequency factor. There were no differences in

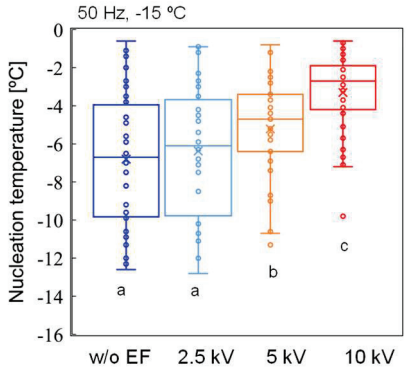

(a)

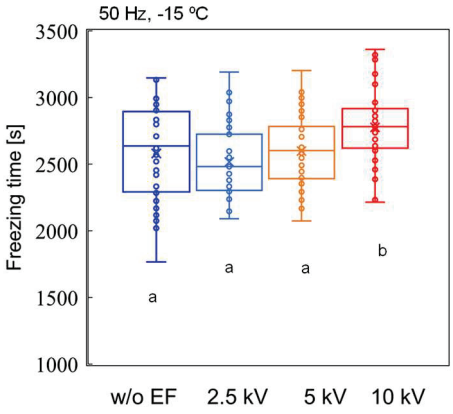

(b)

Figure 5. (a) Ice nucleation temperature and (b) freezing time when voltage is changed

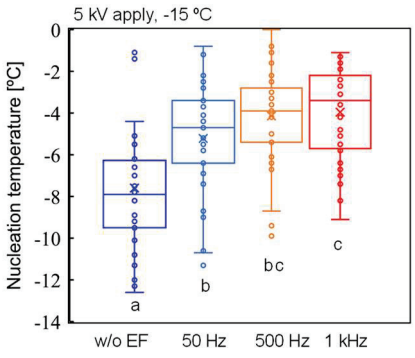

(a)

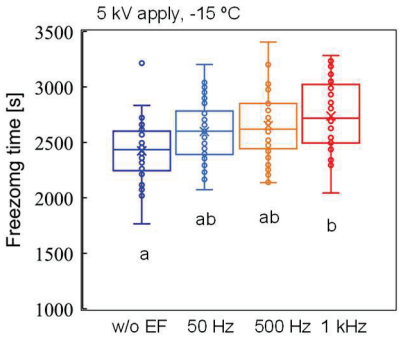

(b)

Figure 6. (a) Ice nucleation temperature and (b) freezing time when frequency is changed

activation energy at each frequency, but higher frequencies resulted in higher frequency factors. Therefore, an increase in frequency of the applied electric field did not affect the activation energy, but it increased the number of orientation polarisations, which increased the probability of reaching ice nucleation, thereby also increasing the ice nucleation temperature. Additionally, the orientation polarisation of water molecules results in dielectric loss as a function of frequency, and the frequency at which the dielectric loss of water reaches a peak is in order of 10^{10} Hz [19,20]. Additionally, at the maximum frequency applied in this study, there is almost no dielectric loss [21]. Under the experimental conditions in this study, almost no water heating occurs from the electric field strength and frequency. Therefore, rise in ice nucleation temperature might not occur due to heat.

4. Conclusions

In this study , the effects of an AC electric field on ice nucleation temperature and nucleation rate were investigated by freezing distilled water while exposing it to varied AC electric field strengths and frequencies. The results showed that, when the electric field strength was varied, the ice nucleation temperature of distilled water increased proportionally to the electric field strength, and high values of nucleation rate were obtained. Additionally, when the frequency was varied, the ice nucleation temperature of distilled water increased proportionally to the frequency, and high values of nuclea-tion rate were obtained. There were no differences between the freezing point of the samples with an electric field applied and the control samples under any of the condi-tions. This showed that changes in electric field strength and frequency do not affect the freezing point.

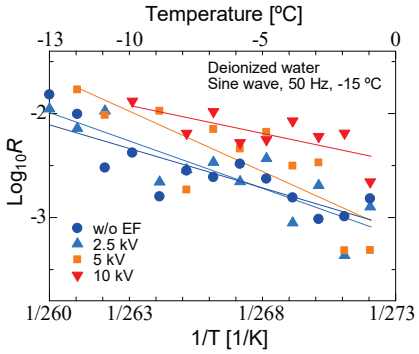

(a)

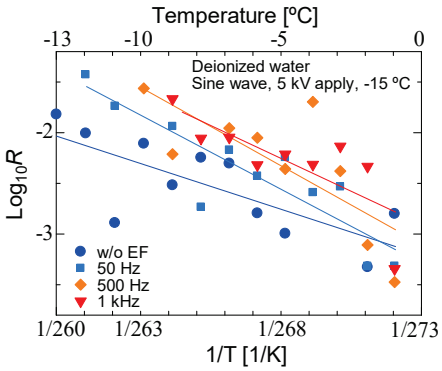

(b)

Figure 7. Ice nucleation rate the respective (a) electric field strengths and (b) frequencies.

Acknowledgments

This research was supported by a Grant-in-Aid for Scientific Research (S), Grant Number 19H05611.

References

[1] U. Helmersson *et al*., "Ionized physical vapor deposition (IPVD): A review of technology and applications", *Thin Solid Films*., **513**, pp. 1–24 (2006).

[2] S. Bauerecker *et al*., "Electric Effect during the Fast Dendritic Freezing of Supercooled Water Droplets", *J. Phys. Chem. B*, **118**, pp. 13629−13635 (2014)

[3] M. Orlowska et. al., "Controlled ice nucleation under high voltage DC electrostatic field conditions", *Food Res. Int.*, **42**, pp.879-884 (2009)

[4] J.H. Mok *et. al.*, "Emerging pulsed electric field (PEF) and static magnetic field (SMF) combination technology for food freezing", *Int. J. Refrig*., **50**, pp. 137-145 (2015)

[5] W. Sun *et. al.*, "Chuanxiang X. Effect of Alternated Electric Field on the Ice Formation During Freezing Process of 0.9%K2MnO4 Water", In Proceedings of the IEEE 8th ICPADM, Bali, pp. 774–777 (2006)

[6] M. Dalvi-Isfahan *et. al*., "Effect of freezing under electrostatic field on the quality of lamb meat", *Innovative Food Sci. Emerging Technol.*, **37**, pp. 68–73 (2016)

[7] E. Xanthakis et.al., "Effect of Static Electric Field on Ice Crystal Size Reduction during Freezing of Pork Meat", *Innov. Food Sci. Emerg. Technol.* **20**, pp. 115–120 (2013)

[8] Y. Ma et. al., "Effect of Applied Electric Field on the Formation and Structure of Ice in Biomaterials during Freezing". In Proceedings of the 2010 10th IEEE International Conference on Solid Dielectrics; IEEE (2010)

[9] T. Hozumi *et.al.*, "Effects of Shapes of Electrodes on Freezing of Supercooled Water in Electric Freeze Control", *Int. J. Refrig*, **28**, pp. 389–395 (2005)

[10] S. Wei et.al, "Effects of Dipole Polarization of Water Molecules on Ice Formation under an Electrostatic Field", *Cryobiology*, **56**, pp. 93–99 (2008)

[11] M. Dalvi-Isfahan *et.al.*, "Review on the Control of Ice Nucleation by Ultrasound Waves, Electric and Magnetic Fields", J. Food Eng. *et al*., **195**, pp. 222–234 (2017)

[12] X.X. Zhang *et. al.*,"Role of the Electric Double Layer in the Ice Nucleation of Water Droplets under an Electric Field", *Atmos. Res.*, pp. 178-179, (2016)

[13] J.Y. Yan, *et. al.*, "Heterogeneous Ice Nucleation Induced by Electric Fields", *J. Phys. Chem. Lett.*, , **2**, pp. 2555–2559 (2011)

[14] H. Nada, *et. al.*, "A Clear Observation of Crystal

Growth of Ice from Water in a Molecular Dynamics Simulation with a Six-Site Potential Model of H2O", *J. Cryst. Growth*, **266**, pp. 297–302 (2004)

[15] S. Sivanesan *et. al.*, "Ice Nucleation of AgI - CuBr Nucleants in the Presence of Electric Field", *Mater. Chem. Phys.*, **27**, pp. 385–392 (1991).

[16] J.Y. Yan, *et. al.*, "Heterogeneous Ice Nucleation Induced by Electric Fields", *J. Phys. Chem. Lett.*, **2**, pp.2555–2559 (2011)

[17] H. Nada *et.al.*, "A Clear Observation of Crystal Growth of Ice from Water in a Molecular Dynamics Simulation with a Six-Site Potential Model of H2O", *J. Cryst. Growth*, **266**, pp. 297–302. (2004(

[18] X. Wang *et.al,* "Textural and Rheological Properties of Soy Protein Isolate Tofu-Type Emulsion Gels: Influence of Soybean Variety and Coagulant Type.", *Food Biophys.*, **13**, 324–332 (2018)

[19] L.H. Seeley *et.al*, "Two-Dimensional Nucleation of Ice from Supercooled Water.", *Phys. Rev. Lett.*, 1–4 (2001)

[20] R. Buchner *et.al.*, "The Dielectric Relaxation of Water between 0C and 35C"*, Chemical Physics Letters*, **306**, 57–63. (1999)

[21] U. Kaatze, "Complex Permittivity of Water as a Function of Frequency and Temperature", *J. Chem. Eng. Data*, **34**, 371–374 (1989)

Decomposition of Dibutyl Phosphate by Discharge inside Bubble in Water

Tetsu Sakakibara, Hirotoshi Takayama, Katsuyuki Takahashi*, Koichi Takaki*, Tatsuya Horimai**, Kiyoshi Anzai**, Takeshi Tsukada**

Faculty of Science and Engineering, Iwate University

**Agri-Innovation Center, Iwate University*

*** JAPAN NUCLEAR FUEL LIMITED Co., Ltd.*

ABSTRACT

Decomposition of dibutyl phosphate dissolved in electrolyte solutions using discharges inside bubble is investigated. Capacitors which have 50 pF capacitance is connected in series between the reactor and the pulsed power generator to suppress the discharge current flows into solution with high conductivity, which contributes to the improvement of the energy efficiency for the decomposition. The concentration of dibutyl phosphate decreased by discharge inside the bubble in any solutions. Dibutyl phosphate is decomposed by a quasi-first order reaction of rate constants on order of $10^{-5} \sim 10^{-4}$ s^{-1} with input power of 0.7 ~ 2 W.

Keywords

Atmospheric plasma, Discharge inside bubble in water, Dibutyl phosphate, Spent nuclear fuel, Nuclear energy

1. Introduction

Reprocessing of spent fuel from nuclear power plant enables effective utilization of nuclear fuel, such as reuse of fuel material and reduction of waste volume [(1)]. Spent fuel contains residual uranium (U), newly produced plutonium (Pu), and high-level radioactive waste. The reprocessing process can separate uranium and plutonium from spent fuel. Generally, the PUREX process has been used to reprocess spent nuclear fuel in the nuclear fuel cycle [(2), (3)]. In the PUREX process, tributyl phosphate (TBP) is used as an extraction solvent for U and Pu [(4)]. TBP is degraded to dibutyl phosphate (DBP) by radiation ray in the solution [(5)]. DBP forms a complex with metal components in high level liquid waste (HLLW) and causes blockage in pipes [(6)], which leads unstable operation of reprocessing plants. Therefore, effective methods for DBP decomposition are required.

Discharge inside bubble in water treatment has attracted attention as a promising method for water treatment. A pulsed discharge inside bubble in water can produce chemical active species such as hydroxyl radical (•OH) and ozone (O_3) at high density. Owing to their high oxidizing power, they contribute to decomposition of organic compounds without selectivity in a short time [(7), (8)]. This process realizes high-speed wastewater treatment without pretreatment, such as pH adjustment. This process also has the advantage that the chemically active species produced can be controlled by selecting the gas injected [(9)].

In this study, decomposition of DBP dissolved in alkaline solutions using discharges generated inside bubble is investigated. Three types of simulated alkaline solutions with different conductivities and ion contents were prepared. Solutions containing these ions has about 100 mS/cm conductivity. In the treatment of high conductivity solutions, discharge current becomes

large because of low resistance of the solutions [9]. Thus, a capacitor which has 50 pF capacitance is connected in series between the reactor and the pulsed power generator to suppress the conductive current flows into solution with high conductivity.

2. Experimental Setup

Three types of simulated alkaline solutions, DBP, SE1 and SE2, were prepared. Table 1 shows solutes and conductivity of each simulated solutions. A solution, DBP, was prepared by dissolving sodium hydroxide (NaOH) and dibutyl phosphate. SE1 was prepared by dissolving sodium carbonate (Na_2CO_3), sodium nitrate ($NaNO_3$), and DBP. SE2 was prepared by adding sodium nitrite ($NaNO_2$) to SE1. The concentration of NaOH, Na_2CO_3, and $NaNO_2$ was 1 M in each solution. The initial concentration of DBP was 23.8 mM in each solution. The initial conductivities of DBP, SE1 and SE2 were 1.7, 100 and 120 mS/cm.

Figure 1 shows a schematic diagram of the reactor. A tungsten wire is inserted into a glass tube and used as a high voltage electrode. Argon (Ar) gas is injected into the glass tube at a gas flow rate of 100 mL/min to generate bubble at the tip of the glass tube. The reactor is immersed in a water bath (LBT-400a, AS ONE Co.) up to a height of 40 mm from the bottom of the reactor to fix the solution temperature at 20 °C. Figure 2 shows a magnetic pulse compression circuit (MPC, Suematsu Electronics CO., LTD., MPC3000S SP) using to apply high voltage pules to the reactor. Peak value of applied voltage is 10 kV, and pulse repetition rate is 250 pps. A capacitor which has 50 pF capacitance is connected in series between the reactor and the pulsed power generator to suppress the conductive current flows into solution with high conductivity.

Table 1 Solutes and conductivity of each simulated solutions

Name	Solutes	σ [mS/cm]
DBP	DBP(23.8 mM) + NaOH(1M)	1.2
SE1	DBP(23.8 mM) + $NaNO_3$(1M) + Na_2CO_3(1M)	93
SE2	DBP(23.8 mM) + $NaNO_3$(1M) + Na_2CO_3(1M) + $NaNO_2$(1M)	117

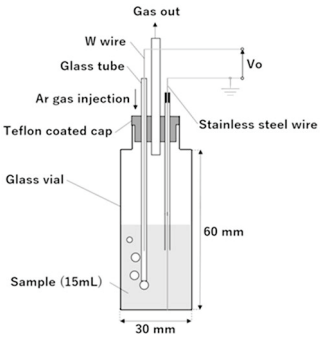

Fig. 1. Schematic diagram of the discharge reactor

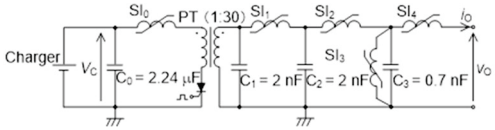

Fig. 2. Schematic diagram of the Magnetic Pulse Compression Circuit.

3. Results and Discussion

3.1 Decomposition of Dibutyl Phosphate

Figure 3 shows typical voltage–current waveforms of the pulse discharge inside bubbles in DBP solutions. The output voltage has a peak value of 7 kV, and its pulse width is 180 ns. The pulse repetition rate is fixed at 250 pulse per second (pps). The energy into the reactor per pulse is calculated by integrating the electric power obtained by the output voltage and current over time and obtained as 8.3 mJ.

Figure 4 shows the time course DBP concentration and energy efficiency for DBP decomposition during discharge treatment. DBP concentration decreases with increasing treatment time, and it decreases to about 2.74 mM with 9 hours treatment. The decomposition rate reaches 90 % after 9 hours treatment. The result shows that DBP can be decomposed by discharge in bubbles in water. DBP is decomposed by a quasi-first order reaction of rate constants on 6.9×10^{-5} s^{-1}. The energy efficiency for DBP decomposition decreases with increasing treatment time, and it decreases to

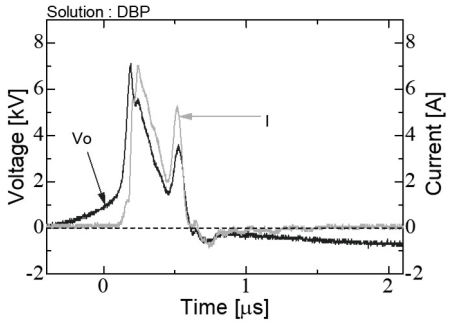

Fig. 3. Typical waveforms of the applied voltage and the current flowing on the reactor when DBP treatment.

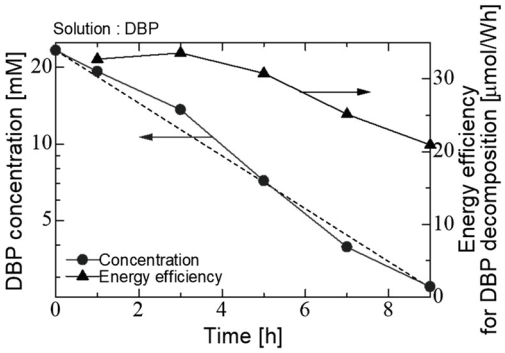

Fig. 4. The time course DBP concentration and energy efficiency for DBP decomposition during discharge treatment.

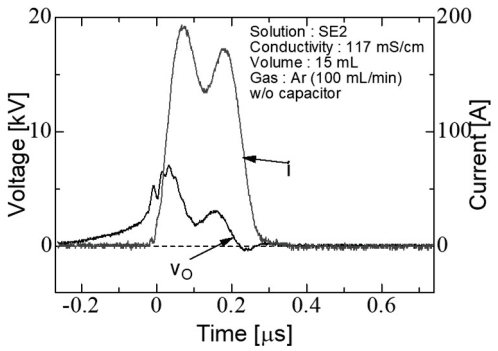

(a)SE2, without capacitor

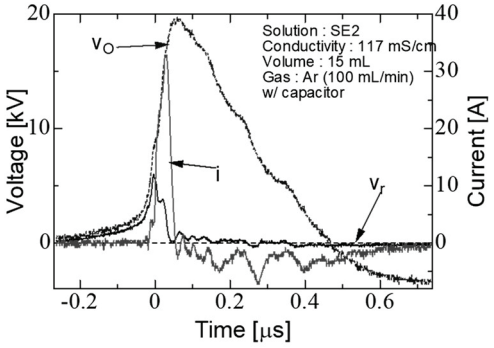

(b)SE2, with capacitor(50 pF)

Fig. 5. Comparison of waveforms of the applied voltage and the current flowing on the reactor with and without capacitor

about 21 μmol/Wh. The reaction rate between DBP and active species produced by discharges decreases with decreasing DBP concentration, and recombination loss reactions of active species increases, which leads decrease in the energy efficiency.

3.2 Using capacitor to suppress reactor current treating high conductivity solutions

Figure 5 shows typical voltage–current waveforms of treating SE2 solutions (a) without and (b) with the capacitor. This figure voltage shows applied voltage to the reactor(v_r) and (v_O). The peak value of the current is 200 A without capacitor, which can be suppressed to 30 A by connecting capacitor. The current pulse width with the capacitor and without capacitor are 250 ns and 70 ns, respectively, and the energy consumption of the reactor with capacitor and without capacitor are 82 mJ and 3 mJ, respectively. Therefore, connecting capacitor between the output terminal of the MPC and the reactor is effective in suppressing the energy per applied high voltage pulse caused by suppressing the current flow and shortened pulse width.

3.3 Reaction rate of decomposition DBP

Figure 6 shows the time course of DBP concentrations in DBP, SE1 and SE2 solutions during discharge treatment. The 50 pF capacitor is connected and the peak applied value of reactor voltage sets 10 kV. The decomposition rates for DBP, SE1 and SE2 solutions after 9 hours treatment are 99%, 80% and 60%, respectively. The result indicates that discharge treatment is effective in DBP decomposition even in solutions containing NO_3^-, CO_3^{2-} and NO_2^-. DBP is decomposed by a quasi-first order reaction. The rate constants in the case of DBP, SE1 and SE2 are 1.9×10^{-4} s^{-1}, 4.8×10^{-5} s^{-1} and 2.6×10^{-5} s^{-1}, respectively.

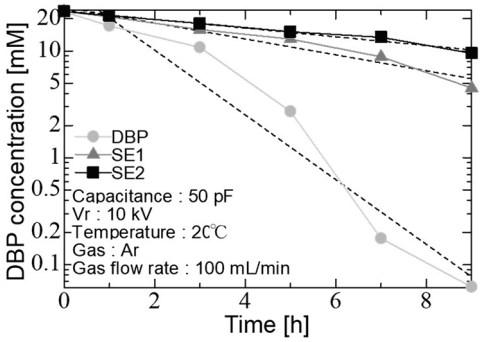

Fig. 6. The time course DBP concentration during discharge treatment.

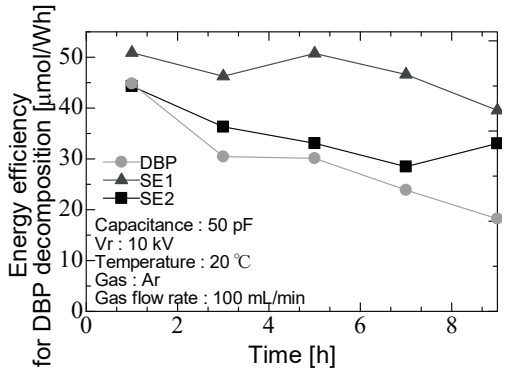

Fig. 7. The time course energy efficiency for DBP decomposition during discharge treatment.

Figure 7 shows energy efficiency for DBP decomposition as a function of treatment time. The energy efficiency after 9 hours treatment in the case of DBP, SE1 and SE2 are 20 mol/Wh, 33 mol/Wh and 22mol/Wh, respectively. SE1, SE2 and DBP are highest energy efficiency, in that order. This is because of increased energy loss due to impedance matching with treating DBP solution or the contribution of carbonate radicals.

4. Conclusions

Three simulated DBP solution are treated by pulsed discharges inside bubbles in solution. DBP decomposition rate in case of DBP, SE1 and SE2, reaches 99%, 80% and 60%, respectively, after 9 hours treatment. DBP concentration decreases according to a quasi-first order reaction. The rate constants in the case of DBP, SE1 and SE2 are 1.9×10^{-4} s^{-1}, 4.8×10^{-5} s^{-1} and 2.6×10^{-5} s^{-1}, respectively. DBP decomposed in solutions even containing NO_3^-, CO_3^{2-} and NO_2^-.

Acknowledgments

This work was supported by METI "Basic research programs of vitrification technology for waste volume reduction" Program Grant Number JPJ010599.

References

[1] Agency for Natural Resources and Energy, “The 6th Strategic Energy Plan”, (2021).

[2] K. Takahashi, “Analysis and Study of Spent Fuel Reprocessing Technology from Birth to Present”, *Trans. At. Energy Soc. Japan*, **5**, 2, pp.152-165 (2006)

[3] H. Ojima, “Outline of the Nuclear Fuel Cycle”, *JAEA-Review 2008-020*, (2008).

[4] A. G. Baldwin et al., “Distribution of Fission Products into Tributyl Phosphate under Applied Nuclear Fuel Recycling Conditions”, *Ind. Eng. Chem. Res.*, **55**, 51, pp.13114–13119 (2016).

[5] A. R. Gillens et al., “Rapid quantification of TBP and TBP degradation product ratios by FTIR-ATR”, *J. Radioanal. Nucl. Chem.*, **296**, 2, pp.859-868 (2013)

[6] C. Lamouroux et al., “Characterization of zirconium complexes of interest in spent nuclear fuel reprocessing by electrospray ionization mass spectrometry”, *Rapid Commun. Mass Spectrom.*, **14**, 19, pp.1869-1877 (2000)

[7] H. Akiyama, “Streamer discharges in liquids and their applications”, *IEEE Trans. Dielectr. Electr. Insul.*, **7**, 5, pp.646-653 (2000).

[8] K. Takahashi, “A Novel Wastewater Treatment Method Using Electrical Pulsed Discharge Plasma over a Water Surface”, *Sewage*, IntechOpen (2021).

[9] K. Takahashi et al., “Influence of reactor geometry and electric parameters on wastewater treatment using discharge inside a bubble”, *Int. J. Plasma Environ. Sci. Technol.*, **13**, 2, pp.74-82 (2019).

Role of Short-Life and Long-Life Active Species on Water Treatment by Water Spray into Pulsed Discharge

Souma Ueno, Phung Nhat Thanh, Taichi Sugai, Weihua Jiang

Extreme Energy-Density Research Institute,
Nagaoka University of Technology

ABSTRACT

In this study, the role of long-life and short-life active species on water treatment by water spray into pulsed discharge was investigated. For this investigation, decomposition rate of indigo carmine and production rate of hydrogen peroxide were evaluated. From the evaluation, these roles are predicted as follows. The Ozone of long-life active specie is not only to decompose substances that are relatively easy to decompose, but also to produce OH radical from its reaction with water and hydrogen peroxide, which decompose persistent substances. The short-life active species such as OH radical and O radical produced directly by the pulsed discharge also decompose persistent substances. However, radicals produced directly by the discharge results in less decomposition rate than OH radical produced via reaction of ozone with water.

Keywords

Ozone, OH radical, pulsed power, water droplet, water treatment

1. Introduction

Since there are serious water issues, e.g., water shortages and water contamination in the world, water treatment technology is very important. Generally, chemical and biological treatments have been used as conventional water treatment. However, these have the inability to decompose persistent substances and generate harmful secondary products. To solve these problems, pulsed discharge water treatment technology has been studied. This is characterized by the strong oxidizing effect of OH radicals and ozone produced by pulsed discharge, which enables the decomposition of persistent substances. A pulsed discharge in gas including air and water dissociates O_2 to form O atoms, cf. Eq. (1) [1]. These O atoms promote the generation of ozone cf. Eq.(2) [1]. Also, the dissociation of water molecules generates OH radicals cf. Eq.(3)[1]

$$O_2 + e \rightarrow 2O\cdot + e \quad (1)$$

$$O_2 + O\cdot \rightarrow O_3 \quad (2)$$

$$H_2O + e \rightarrow H\cdot + OH\cdot + e \quad (3)$$

In many kinds of reactor structures using pulsed discharge, the best efficiency has been obtained by a method of spraying water into pulsed discharge in gas. The purpose of this study is to further investigate the role of short-life species such as OH radical and long-life species such as ozone on this method.

2. Experimental Setup

Figure 1 and Figure. 2 show the experimental setup. Figure 1 shows the reactor discharge system. The composition of the discharge reactor is an acrylic cylinder and coaxial electrodes. The acrylic cylinder has an inner diameter of 40 mm, and the wire electrode is made of stainless-steel wire (diameter = 0.28 mm). The cylindrical electrode is made of stainless-steel cylinder (diameter=38 mm, length 300 mm). Sample water in a tank is sprayed into the reactor where the discharge is generated, while being circulated by a pump. From a top side of the reactor, air is also flowed. The discharge in the reactor produces short-life (OH radical, O radical) and long-life (Ozon) active species. In the setup in Fig. 2, calling ozonizer discharge system, an electrode of

same structure as Fig. 1 is put at external place of the reactor which the water sample is sprayed into. Only long-life active species (Ozon) produced in the electrode is supplied into the reactor by air flow. To generate the discharge, a positive pulsed voltage is applied to the wire electrode by a pulse generator which is an inductive energy storage circuit using a Semiconductor Open Switch [2], and the cylindrical electrode is grounded. Fig. 3 shows typical voltage and current waveforms at the electrode.

In this study, two experiments were conducted. The first experiment was a decomposition experiment of Indigo carmine[1]. For this experiment, 1.5 L of indigo carmine solution (20 mg/L) was used. The frequencies of the pulse apply were 100, 300, and 500 Hz. The air flow rate was 10 L/min. Two evaluations were done for this experiment: one is evaluation of the decomposition of the chromogenic bonds of the indigo carmine by measuring the absorbance at 610 nm. The other is evaluation of the decomposition of unsaturated bond by measuring the absorbance at 250 nm. The second experiment was the measurement of hydrogen peroxide. In this evaluation, 1.5 L of deionized water was used and frequencies of pulse apply were 100, 300, and 500 Hz. The air flow rate was 10 L/min and the treatment time was 5 minutes. The hydrogen peroxide produced based on the above condition was measured using a reagent set (Kyoritsu Riken Co., Ltd.).

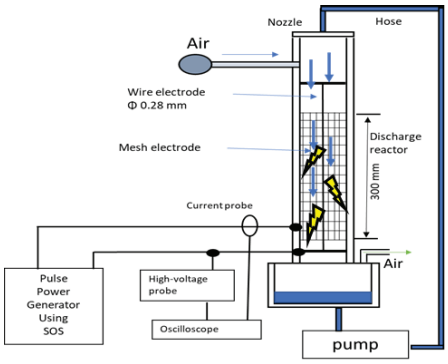

Fig. 1 Reactor discharge system.

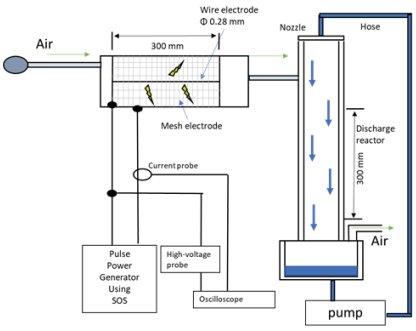

Fig. 2 Ozonizer discharge system

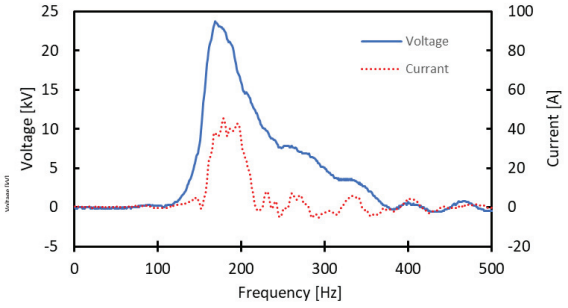

(a)

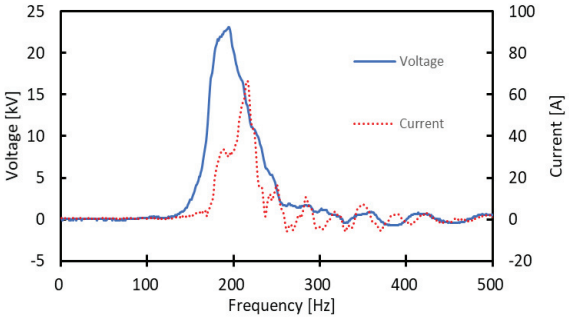

(b)

Fig. 3 (a) Reactor discharge wave form. (b) Ozonizer discharge wave form

3. Results and Discussion

Figure 4 shows rate and energy efficiency for the decomposition of the chromogenic bond for the two systems. In both systems, energy efficiency decreased with increasing frequency. From this result, it is predicted that the increase of the amount of ozone was saturated with the increase of frequency. Comparing the reactor discharge and the ozonizer discharge, the ozonizer discharge is faster decomposition, and less input energy than the reactor discharge.

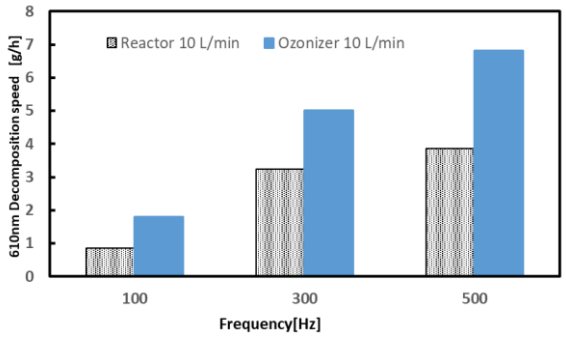

(a)

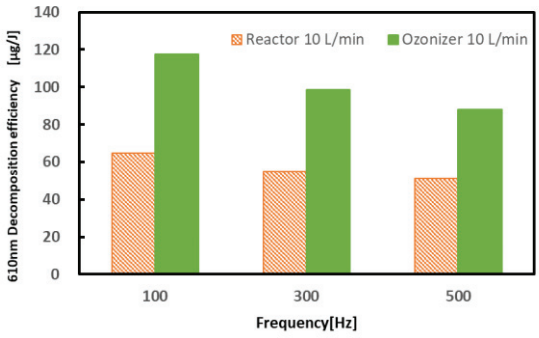

(b)

Fig. 4 (a) Chromogenic bond decomposition rate at various frequencies. (b) Chromogenic bond energy efficiency for the decomposition at various frequencies.

This means that reactor discharges are inefficient at producing ozone because energy is also used for water excitation, dissociation, and ionization, making it difficult to produce ozone

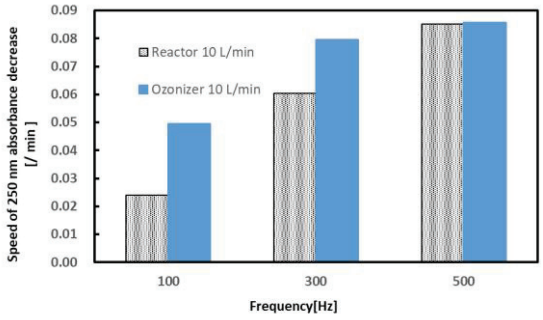

(a)

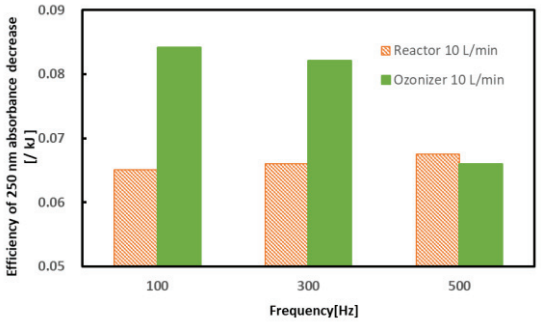

(b)

Fig. 5 (a) Decrease rate of absorbance 250 nm (b) Energy efficiency of decrease of absorbance 250 nm Note absorbance of 250 nm is proportional to unsaturated bond of indigo carmine.

Figure 5 shows the rate of decrease of 250 nm absorbance to time and input energy, which are equivalent to speed and energy efficiency of the decomposition of unsaturated bonds. In the case of the ozonizer discharge, the decrease of the absorbance of 250 nm was faster with less input energy than the case of the reactor discharge, and the energy efficiency decreased with increasing frequency, as with the decomposition of the chromogenic bond. Thus, not only OH radical and O radical but also ozone contributes the decomposition of the unsaturated bond. On the other hand, the energy efficiency of the reactor discharge was unaffected by frequency. It is expected that short-life active species, i.e., OH and O radicals produced by electron collision with water, mainly decomposed the unsaturated bonds in case of the reactor discharge.

Figure 6 shows the measurement results of hydrogen peroxide. The reason for measuring hydrogen peroxide is to find out how much OH radicals are generated by the reaction equation shown in Eq. (4)[3].

$$HO\cdot + HO\cdot \rightarrow H_2O_2 \qquad (4)$$

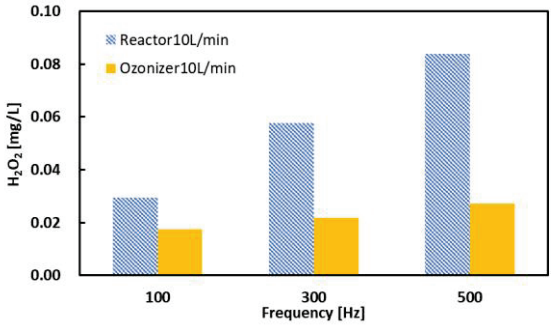

Fig. 6 The amount of hydrogen peroxide at various frequency

As the result, hydrogen peroxide was also detected from the ozonizer discharge system. As the process of OH radical production, complicated reactions of ozone with hydroxide ion are expected. The amount of hydrogen peroxide produced by the reactor discharge is higher than that by the ozonizer discharge. As the reasons of this, it is predicted that more ozone produced by the ozonizer discharge decomposes more hydrogen peroxides, cf. Eq. (5)[4], and that OH radicals produced by electron collision is easier to combine each other to produce hydrogen peroxide than those produced via ozone decomposes

$$H_2O_2 + 2O_3 \rightarrow 2OH \cdot + 3O_2 \qquad (5)$$

Considering the above discussion, ozone contributes to the decomposition of the unsaturated bond via OH radical production from the reactions of ozone with water, as with OH radical and O radical produced by the electron collision with water and oxygen. Since Fig. 6 shows more unsaturated bonds are decomposed by the ozonizer discharge than by the reactor discharge, the OH radicals produced from ozone may be more likely to react with the organic matter in the water than those produced via electron collision due to easier combination of OH radical produced via electron collision.

4. Conclusions

The role of long-life active species such as ozone is to decompose substances that are relatively easy to decompose. Also ozone reacts with water and hydrogen peroxide to produce OH radicals, which decompose persistent substances. The role of short-life active species OH and O radicals generated by the reactor discharge decompose persistent substances. The OH and O radicals generated directly by the discharge are short-life, so their efficiency is not affected by the discharge frequency. However, the OH radicals generated directly by the discharge might be easier to combine each other, causing the efficiency of organic decomposition to decrease.

References

[1] Yasushi Minamitani, Member, IEEE, Satoshi Shoji, Yoshihiro Ohba, and Yoshio Higashiyama, Member, IEEE: “Decomposition of Dye in Water Solution by Pulsed Power Discharge in a Water Droplet Spray”, IEEE TRANSACTIONS ON PLASMA SCIENCE, Vol. 36, No. 5, p.2588 (October 2008)

[2] Taichi Sugai, Member, IEEE, “The Effect of Scale-Up of Pulsed Corona Discharge for Treatment of Pollution Water Sprayed in Discharge Gap” IEEE TRANSACTIONS ON PLASMA SCIENCE, VOL. 44, NO.10, p2209, (OCTOBER 2016)

[3] K. Takahashi, K. Takahashi and N. Satta: “Water remediation using pulsed power discharge under water with advanced oxidation process”, Adv. Oxidat., Vol. 15, No.2, pp.365-373(2012.6)

[4] Mika E.T. Sillanpää, Tonni Agustiono Kurniawan and Wai-hung Lo, “Degradation of chelating agents in aqueous solution using advanced oxidation process (AOP)”, Chemosphere 83 (2011) 1449

Effect of anode tip shape on pinch plasma formation in plasma focus

Takuho Yamada*, Yosuke Omura, Hiroaki Ito, and Taichi Takezaki

Department of Electrical and Electronic System Engineering, University of Toyama

ABSTRACT

Plasma focus (PF) devices are able to produce high-temperature and high-density plasmas by self-pinch (Z-pinch) due to the magnetic field generated by the discharge current in the plasma. The PF device emits an ion beam with high energy of several MeV even at a charging voltage of several tens kV. In order to apply the plasma focus device to the intense pulsed ion source, it is necessary to examine the ion acceleration mechanism for generating optimal ion beams. In this study, the influence of four anode tip shapes, cylindrical with a hollow top, tapered with a hollow top, and two tapered with a flat top having taper angles of 10° and 45°, on the plasma sheet was investigated to improve the ion beam characteristics and to clarify the acceleration mechanism of the ion beam.

Keywords

Plasma focus devices, pinch plasma, plasma sheet, high-intensity ion beam

1. Introduction

Plasma Focus (PF) devices can produce a high-temperature and high-density plasma and emit high-energy ions, electrons, X-rays, and neutrons [1-4]. The main applications of PF devices are as a source of charged particle beams, X-rays, neutrons, etc. Especially, high-energy ion beams (>1 MeV) have been confirmed to be generated by the PF devices at a charging voltage of several tens kV [5, 6], and are expected to be used for material processing, ion implantation, and other applications. It has been found that the high-energy ion beam intensity emitted from PF devices depends on the electrode geometry, the energy of the capacitor bank, and the working gas and pressure [7]. Although these parameters are thought to influence the ion acceleration mechanism, the mechanism of high-energy ion beam generation has not been fully understood [8].

In previous studies, the tapered anode enhanced the intensity and the energy of the ion beam in comparison with the conventional cylindrical one [9]. In this study, to clarify the influence of the anode tip shape on the ion beam characteristics, the plasma sheet evolution and the plasma column formation were observed using a high-speed camera and the effect of the anode tip shape was investigated.

2. Plasma focus operating principles

Figure 1 shows the principle of operation of the plasma focus devices. The coaxial plasma focus device consists of a central electrode (anode) and an outer electrode (cathode), separated by an insulator between the two electrodes. The principle of operation is shown below.

① When a high voltage pulse is applied between the electrodes after filling gas in the chamber, the discharge current due to the dielectric breakdown flows on the insulator and a plasma sheet (current sheet) is generated.

② The current sheath lifts off the insulator and is accelerated axially to the electrode tip by the interaction of the current with its own magnetic field (Lorentz force $J \times B$).

③ After the plasma sheet reaches the tip of the electrode, it contracts in the radial direction with axial motion. At the compression phase, a hot

and dense plasma column is formed on the top of the anode.

④ The dense plasma column rapidly pinches and collapses due to the growth of instabilities such as sausage instability, etc., which leads to an emission of soft x-rays and an induced electric field. With this electric field, electrons are accelerated towards the anode, while ions are accelerated in the opposite direction.

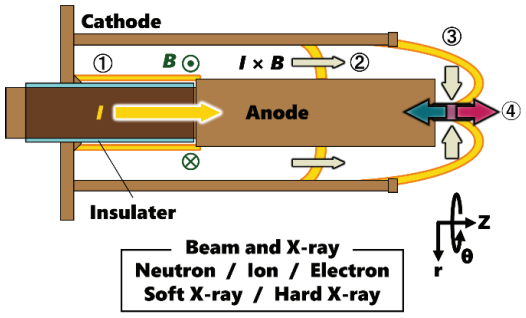

Fig.1 Operation principle of plasma focus

3. Experimental Setup

3.1 PF device and measurement system

Figure 2 shows the experimental arrangement used in the present study. The plasma focus device is a Mather-type device. The electrode arrangement is composed of a central copper anode with 270 mm in length and 50 mm in diameter and a cathode made up of 24 copper rods arranged in a circle of 100 mm in diameter. The length and diameter of 24 cathode rods are 245 mm and 10 mm, respectively. A Pyrex glass insulator sleeve with 100 mm long and 60 mm in outer diameter is rigidly fixed at the bottom end of the anode separating the electrodes.

A gated image intensifier with the gate width of 5 ns was used to observe the contraction process of the pinch plasma near the anode tip and evaluate the evolution of current sheet and the formation of dense plasma column. The camera was placed at 270 mm in the radial direction from the central axis of the anode. The discharge current was measured using a Rogowski coil. The ion current density and the hard X-ray emitted after the pinch were measured using a biased ion collector (BIC) and a scintillation probe, respectively. The BIC was placed 180 mm away from the anode tip on the central axis and the scintillation probe was placed 6 m from the plasma focus device.

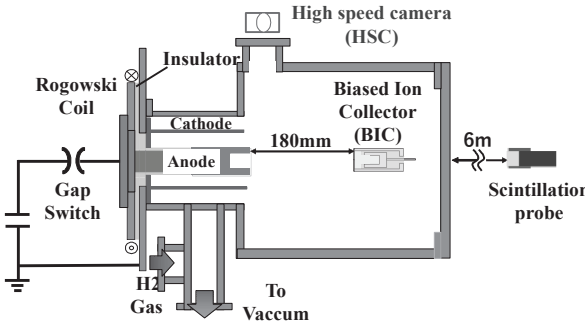

Fig.2 Experimental arrangement

3.2 Anode tip shape

Figure 3 shows the design of four anode tips used in this experiment. A cylindrical hollow anode, a 10° tapered hollow anode, a 10° tapered flat anode, and a 45° tapered flat anode were used. The total length of the anode is 270 mm and the effective length of all these tips is 75 mm. The diameter of tapered anode tip is 30 mm. To reduce the production of impurity ions and the damage of the electrode, the anode has a hollow shape top. The hollows of cylindrical and tapered anodes have 50 mm in depth and 39 mm and 20 mm in diameter, respectively. They have a length of 75 mm, an outer diameter of 50 mm for the cylinder, and an outer diameter of 30 mm for the tapered tip.

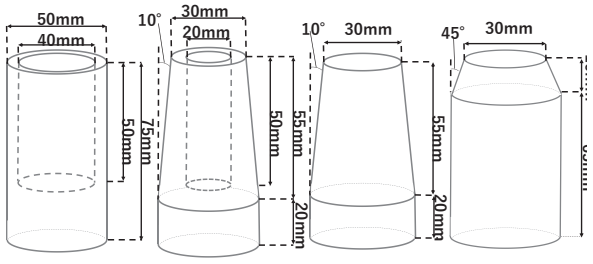

Fig. 3 Structure of four different anode tips: (a) cylindrical hollow-end anode, (b) 10° tapered hollow-end anode, (c) 10° tapered flat-end anode, and (d) 45°tapered flat-end anode.

4. Experimental results

4.1 Typical waveform

Figure 4 shows the operating waveforms and photos taken by the high-speed camera when the 10°

tapered hollow type was used. Figure 4(a) shows the discharge current by the Rogowski coil, the ion current density by the BIC, the hard X-ray signal by the scintillation probe, and the gate signal for the high-speed camera. As shown in Fig. 4(a), the current has a large dip from 630 kA to 420 kA between 1.8 μs and 2.4 μs, indicating the sudden change in inductance caused by the collapse of the plasma column due to instabilities in the plasma. The hard X-ray signal is observed at the same time as the current dip and the ion current density also rises almost simultaneously with the X-ray signal. The ion current density has a maximum value of 2 kA/cm^2, but the second peak around 2.1 μs is considered to be ions pushed out axially during plasma sheet propagation.

Figure 4(b) is a plasma column image taken 10 ns before the hard X-ray signal falls. It can be seen from Fig. 4(b) that the plasma sheet is generated from the anode to the cathode direction. In addition, a plasma column is formed around the anode tip and cut off in its middle. Therefore, we can see that the collapse of the plasma column has started at this time.

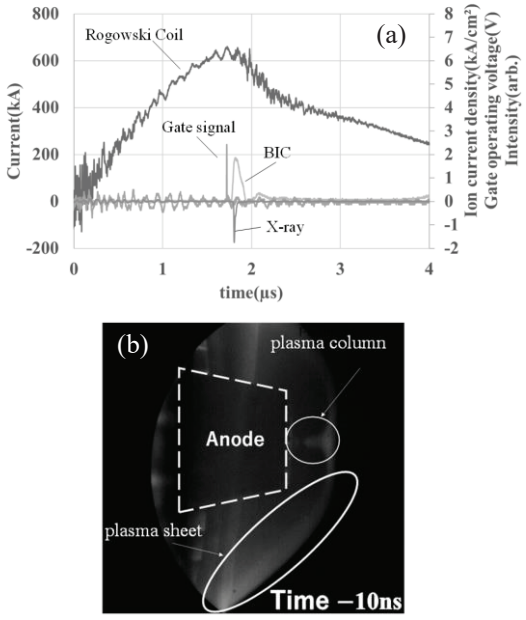

Fig.4 (a) Typical waveforms and (b) Photo taken by high-speed camera for 10° tapered hollow anode.

4.2 Evolution of plasma sheet

Figure 5 shows photographs of the plasma sheet evolution for each anode shape. The time difference between the gate timing of the ICCD camera and the fall time of the scintillation probe is shown in the lower right of the photo. We made a comparison between the photos for anode shapes with almost the same gate timing, since it is difficult to set the gate time for each shot. As seen in Fig. 5(a), in the cylindrical hollow type, the plasma sheet has already reached the anode tip at time 138 ns before the X-ray signal starts, and begins to contract toward the center of the anode. The current sheet reaches the electrode center axis 100 ns after reaching the electrode and starts to pinch. A plasma column is formed at time -33 ns, a local contraction and collapse of the plasma column are observed at time -16 ns, and then the plasma column disappears.

From Figs. 5(b) and 5(c), in the tapered anode, the plasma sheet has not reached the anode tip at around -130 ns yet and is moving in the axial direction. It begins to move toward the center of the anode tip after reaching the tip at around -80 ns. A plasma column is formed at around -30 ns, and after a local

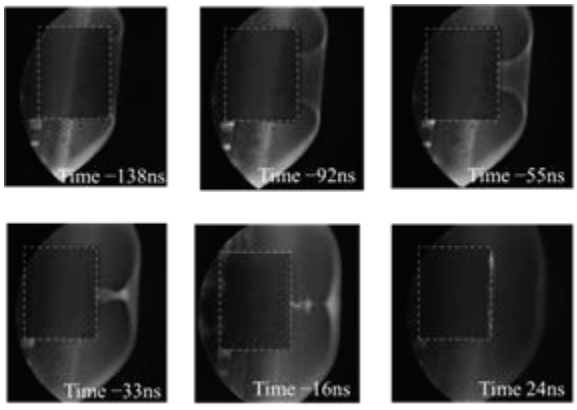

(a) cylindrical hollow-end anode

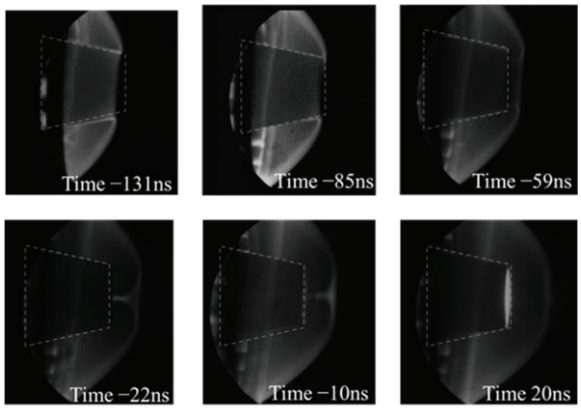

(b) 10° tapered hollow-end anode

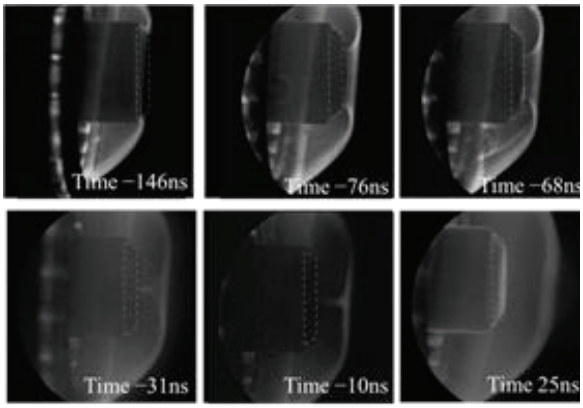

(c) 45° tapered flat-end anode

Fig. 5 Gated images of plasma sheet evolution for each anode shape

contraction and collapse at around -10 ns, the plasma column finally disappears. It can also be seen that at all anode shapes, the plasma sheet travels not only in the central direction but also in the axial direction after it reaches the anode tip.

4.3 Plasma column for each anode shape

Figure 6 shows photos taken at the time of plasma column formation for each anode geometry. Here, the gate width of the high-speed camera is 5 ns. The time listed in the lower right corner of the figure is the time difference from the fall time of the hard X-ray signal.

Table 1 shows the plasma column parameters for each anode tip shape. It can be seen that the length and diameter of the plasma column become shorter and the angle of the plasma sheet becomes larger when a tapered anode is used. With the increase of the inclination angle of the taper anode, the length and diameter of the plasma column become longer, while the angle of the plasma sheet was almost the same as that of the cylindrical anode. The use of a hollow electrode shortened the length and diameter of the plasma column but did not change the angle of the plasma sheet.

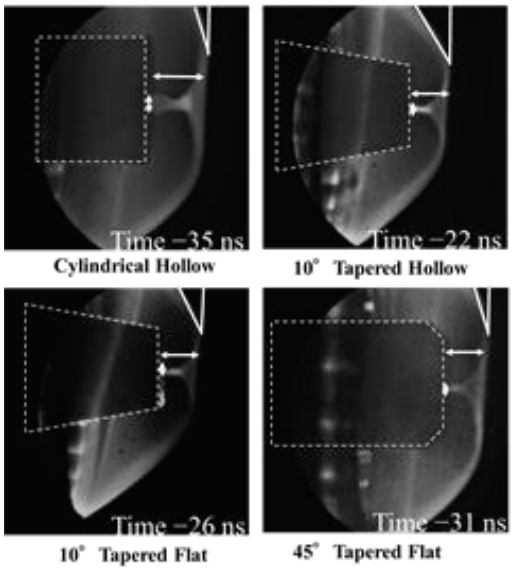

Fig. 6 Gated images of Plasma column for each anode shape

Table. 1 Parameter of plasma column

	Length(mm)	Diameter(mm)	Angle(deg)
Cylindrical Hollow	22.0	6.59	18.1
10° Tapered Hollow	14.1	2.35	29.3
10° Tapered Flat	14.4	2.65	30.8
45° Tapered Flat	14.8	3.30	18.2

4.4 Plasma sheet propagation speed and angle

Figure 7 shows the time evolution of velocity and angle of the plasma sheet for each anode shape. The closer the plasma sheet is to the central axis of the anode, the faster the plasma sheet velocity is. It is evident from Fig. 7(a) that the cylindrical anode has a faster evolution velocity of the current sheet than the tapered one and that the tapered anode with an inclination angle of 45° has a faster evolution velocity than one with a 10° inclination angle. It can be seen from Fig. 7(b) that the radial velocity increases as the plasma sheet approaches the center of the anode, since the closer the plasma sheet is to the center of the anode, the sharper the angle of the plasma sheet becomes. The cylindrical electrode has a sharper angle of the plasma sheet than the tapered one. In addition, the angle of the plasma sheet is sharper with an increase of the inclination angle for the tapered anode.

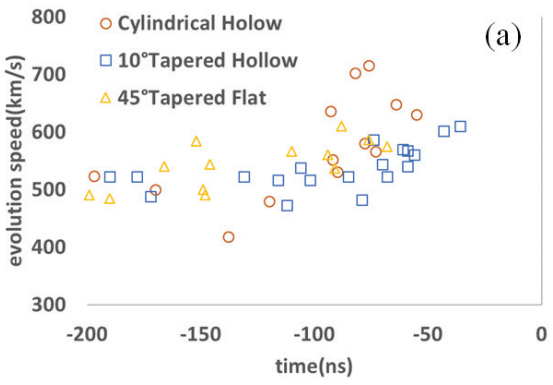

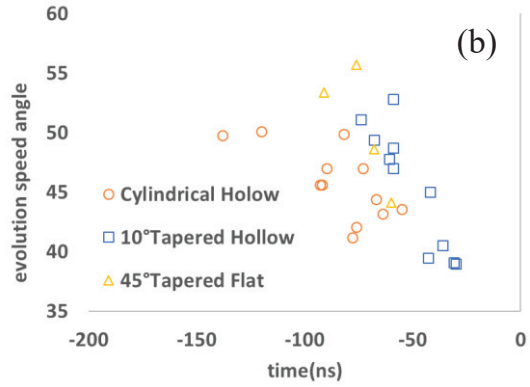

Fig. 7 Time evolution of (a) velocity and (b) angle of plasma sheet for each anode shape

5. Conclusions

The effect of the anode tip shape on the plasma column formation and the time evolution of the plasma sheet in a PF device were investigated using a high-speed camera. When the tapered anode was used, both the length and diameter of the plasma column became shorter. The velocity of the current sheet was getting faster as the sheet propagated toward the electrode tip. In addition, both the length and diameter of the plasma column and the current sheet velocity became larger and faster, respectively when the inclination angle of the tapered anode was changed from 10° to 45°. These results indicate that the anode tip shape affects the high-density plasma column and plasma sheet. Previous studies showed that the ion current and energy of the ion beam on the axis were enhanced when the tapered anode was used. The results obtained in this study suggest that the plasma column for the tapered anode has a smaller volume than for the cylindrical one, resulting in a denser plasma column and stronger pinch. Therefore, the tapered anode has a larger plasma column energy, which is thought to be able to generate a higher-energy and high-intensity ion beam. Since the density in the plasma column was not evaluated in this study, we need to measure the density in a plasma column using shadowgraphs or other methods to evaluate the effect on the ion beam in detail.

Acknowledgment

This work was supported by JSPS KAKENHI Grant Number JP19H02126.

References

[1] M.A. Mohammadi, *et al*., "The effect of anode shape on neon soft X-ray emissions and current sheath configuration in plasma focus device", J. Phys. D, **42**, 045203 (2009).

[2] A. Vladimir, *et al*., "Examination of a chamber of a large fusion facility by means of neutron activation techique with nanosecond neutron pulse generated by dense plasma focus device PF-6", Fusion Eng. Des., **125**, pp.109–117 (2017).

[3] H.R. Yousefi, Y. Nakata, H. Ito, K. Masugata, "Characteristic observation of the ion beams in the plasma focus device", Plasma Fusion Res., **2**, S1084 (2007).

[4] A. Patran, *et al*., "Spectral study of the electron beam emitted from a 3 kJ plasma focus", Plasma Sources Sci.Technol., **14**, pp.549-560 (2005).

[5] H. Kelly, *et al*., "Analysis of the Nitrogen Ion Beam Generated in a Low-Energy Plasma Focus Device by a Faraday Cup Operating in the Secondary Electron Emission Mode", IEEE Trans. Plasma Sci., **26**, pp.113-117 (1998).

[6] H. Ito, Y. Nishino, K. Masugata, "Emission characteristics of a high-energy pulsed-ion-beam produced in a dense plasma focus device", J. Korean Phys. Soc., **59**, pp3674-3678 (2011).

[7] M.A.Mohammadi, *et al*., "The effect of anode shape on neon soft x-ray emissions and current sheath configuration in plasma focus", J. Phys. D: Appl. Phys. **42**, 045203 (2009).

[8] V.A.Gribkov, "Physical processes taking place in dense plasma focus devices at the interaction of hot plasma and fast ion streams with materials under test", Plasma Phys. Control. Fusion, **57** 065010 (2015).

[9] Y. Sagano, *et al*., "Characteristics of pulsed ion beam emitted from plasma focus device with different anode shapes", NIFS-PROC, **121**, pp.30-35 (2021).

Study on X-ray emission and generation conditions for divergent wire array Z-pinch

Miharu Takao, Hiroaki Ito, Taichi Takezaki, and Keiichi Takasugi*

Department of Electrical and Electronic Engineering, University of Toyama

*Institute of Quantum Science, *Nihon University*

ABSTRACT

In order to produce high-temperature pinch plasmas, various types of wire array Z-pinches have been studied so far. These Z-pinch experiments require a fast pulsed power generator with a rise time of less than 100 ns to prevent the wire from evaporating and turning into plasma before the Z-pinch occurs. We have shown a new type of Z-pinch based on a slow-rising current like a capacitor bank can be realized by arranging the wires divergently. Divergent wire array Z-pinch experiments were conducted by using the capacitor bank with a capacitance of 18 μF and a charging voltage of −25 kV. Two wires were aligned divergently between the electrodes. Six kinds of wire materials, aluminum (Al), copper (Cu), molybdenum (Mo), tungsten (W), platinum (Pt), and gold (Au) were used as the discharge medium. In order to observe the soft x-ray of more than 700 eV emitted from the pinch plasma and the time-resolved shape of the plasma, a scintillation probe (SCI) with a 5 μm thick Be window and a gated camera with an image intensifier were used, respectively. The gate width was set to 20 ns. When the copper wire with a diameter of 25 μm was used, the SCI signal was the most stable and strongest of the six materials. In addition, an isolated hot spot was observed at the moment of the pinch.

Keywords

Divergent z pinch, wire array, hot spot, soft x-ray radiation

1. Introduction

Plasma focus and divergent gas puff Z-pinch have been used to develop sources of neutrons, hard X-rays, and soft X-rays [1,2]. In particular, it has been found that mixing gases with a large atomic number increases the energy input to the plasma in the latter device, resulting in higher temperatures [3]. Wire array Z-pinch using heavy elements other than gases has also been studied to produce high-temperature pinch plasmas, and the atomic number dependence of the electron temperature has been reported [4]. However, a fast pulsed power supply is required to prevent the wire from evaporating before plasma formation. In addition, to the best of our knowledge, there are no reports that plasma is focused on a single point in wire array Z-pinch devices.

We have developed a new type of wire array Z-pinch with single-point focusing using a capacitor bank with a simple device structure. In this study, we investigated the effect of the conditions for generating the divergent wire array Z-pinch and the X-ray emission on the wire material and diameter was investigated to generate a pinch plasma with a higher temperature.

2. Experimental Setup

Figure 1 shows the experimental setup. A capacitor bank with a capacitance of 18 μF was used as the power supply, and experiments were conducted at a charging voltage of −25 kV. The anode was an aluminum electrode with a diameter of 20 mm and the cathode was an aluminum electrode with a hole with an inner diameter of 60 mm. A negative voltage

was applied to the anode, while the cathode was attached to a vacuum vessel and was at ground potential. Two metal wires were attached between the electrodes. In order to examine the conditions for generating a pinched plasma, six types of metal wire, aluminum (Al), copper (Cu), tungsten (W), gold (Au), molybdenum (Mo), and platinum (Pt), were used as discharge media. The pressure in the vacuum vessel was kept in the range of 5.0×10^{-3} to 1.0×10^{-2} Pa in all experiments.

The input and output currents to the plasma are measured by two Rogowski coils built into the device, respectively. An X-ray diode (XRD), a scintillation probe (SCI) with a Be filter of 5 μm thickness, and a pinhole camera with a Be filter of 15 μm thickness were used to observe soft X-rays emitted from the pinched plasma. A high-speed camera with a gate width of 20 ns using an image intensifier was also used to capture the plasma shape.

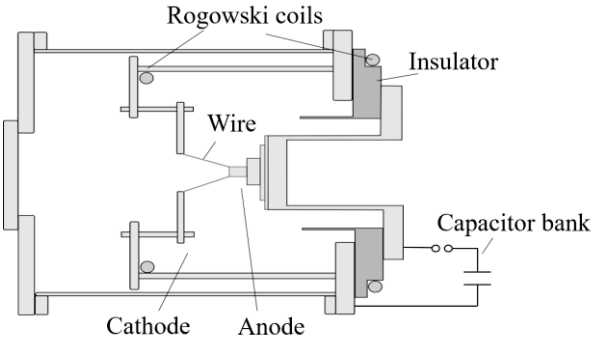

Fig. 1 Experimental Setup

3. Results and Discussion

3.1 Wire Array Z-Pinch

Figure 2 shows the waveforms of the current, scintillation probe (SCI) signal, and X-ray diode (XRD) signal obtained in this experiment. Here, a copper wire with a diameter of 25μm was used as discharge media. The XRD signal rises at 1 μs after the start of discharge and increases with time. As seen in Fig. 2, the discharge current has a dip at 2.3 μs later, and the current value at this time is −220 kA, indicating an abrupt change in inductance. The SCI signal strongly spikes at the same time as the current dip. From these results, it can be found that the plasma starts to generate at 1 μs after the voltage is applied, and the plasma is pinched at 2.3 μs.

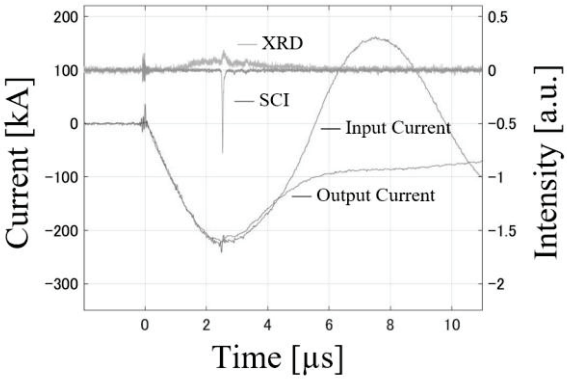

Fig. 2 Typical Waveforms

Figure 3 (a) shows a photograph of the plasma shape taken by a high-speed camera at the first pinch of 2.26 μs. As shown in this figure, the plasma contracts toward the central axis, forming a plasma column. Figure 3 (b) shows a soft X-ray image taken by a pinhole camera. It is evident from Fig. 3(b) that soft X-rays are strongly emitted from a single point. These results show that a new type of wire array Z-pinch with single-point focusing can be realized using a capacitor bank.

3.2 Generation conditions of the divergent wire array Z-pinch on the wire material and diameter

In order to investigate the generation conditions of Z-pinch plasma for wire materials and diameters, we performed the experiments using eleven types of wire: Al Φ 25 μm, Cu Φ 25 μm, Cu Φ 30 μm, Cu Φ 50 μm, Mo Φ 30 μm, W Φ 10 μm, W Φ 20 μm, W Φ 30 μm, Pt Φ 30 μm, Au Φ 25 μm, and Au Φ 30 μm. Table 1 shows the correlation between the formation

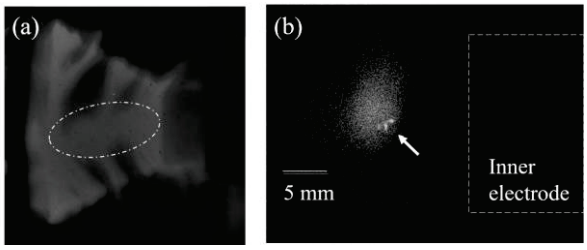

Fig. 3 (a) photo of plasma shape taken by high-speed camera at the first pinch of 2.26 μs and (b) soft X-ray image taken by a pinhole camera

of pinch plasma and the wire properties: material, diameter, atomic number, latent heat, and resistance. Here, the generation of pinch plasma was evaluated by the scintillation probe signal.

Table 1 Correlation between formation of pinch plasma and wire properties

	Atomic Number	Latent Heat (J)	Resistance (Ω)	Pinch
Al Φ25 μm	13	1.31	2.87	○
Cu Φ25 μm		1.90	1.70	○
Cu Φ30 μm	29	2.73	1.18	○
Cu Φ50 μm		7.60	0.43	×
Mo Φ30 μm	42	4.23	3.77	×
W Φ10 μm		0.60	33.60	○
W Φ20 μm	74	2.43	8.41	○
W Φ30 μm		5.48	3.73	×
Pt Φ30 μm	78	3.35	6.69	×
Au Φ25 μm	79	1.42	2.03	○
Au Φ30 μm		2.05	1.41	○

It can be seen from Table 1 that the occurrence of pinch plasma depends on the wire material and the wire diameter. The wire in which the pinch plasma is formed tends to have smaller latent heat than that in which no pinch occurs. The threshold of the latent heat is considered to be 2.8 - 3.5 J under the present experimental conditions. We now discuss the reason why latent heat affects the generation of Z-pinch plasma. The latent heat is the sum of the heat of fusion and the heat of evaporation. Thus, the latent heat has a relationship with the energy required to evaporate the wire when an electric current is applied to the wire. Although the latent heat is small compared to the energy input to the device calculated from the current waveform, it is considered that the latent heat affects the time it takes for the wire to turn into a plasma.

Figure 4 shows soft X-ray images taken with a pinhole camera for four types of wires: Cu Φ25 μm, Al Φ25 μm, W Φ20 μm, and Au Φ25 μm. It is turned out from Fig. 4 that soft X-rays are strongly emitted from a single point when Al and Cu are used, while soft X-rays are emitted from a wide area when W and Au are used. The current waveform for each wire reaches its peak at 1/4 period (about 2.7 μs), although there is some variation from shot to shot. The plasma contraction time depends on the mass of the wire material. The contraction time for the heavier element is longer than the time of the current peak. Therefore, it is considered that the area of observed X-ray emission becomes wider, since the plasma cannot be sufficiently pinched for heavy elements.

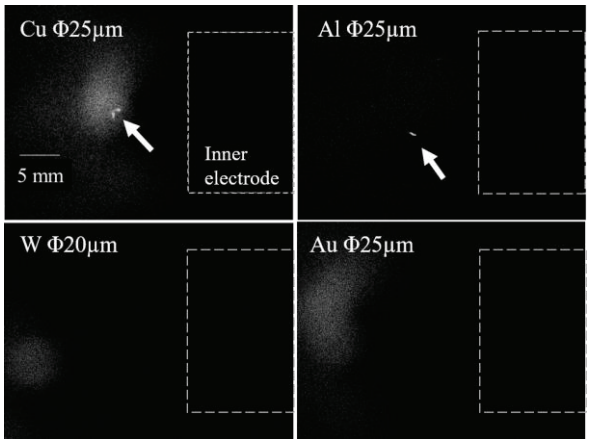

Fig. 4 Soft X-ray images of Cu, Al, W, and Au by pinhole camera

3.3 Generation conditions of the divergent wire array Z-pinch for number of wires

The results show that the material of the wire affects pinch plasma generation and soft x-ray emission, and latent heat is one of the parameters. Next, we investigated the dependence of the number of wires on the formation of pinch plasma and soft X-ray emission. Four types of wires were used in the experiments: aluminum with a diameter of 25 μm, copper with diameters of 25 μm and 30 μm, and tungsten with a diameter of 20 μm. Three to five wires were placed axisymmetrically between the electrodes. Table 2 shows the results of latent heat and Z-pinch plasma generation for each experimental condition. Here, the symbols: circle, triangle, and cross, indicate the intensity of the X-ray emission. In aluminum wire, the formation of Z-pinch plasma was

Table 2 Results of Z-pinch plasma generation for number of wires

	Latent Heat (J) 2本	3本	4本	5本
Al Φ25 μm	1.31	○ 1.97	○ 2.63	○ 3.29
Cu Φ25 μm	1.90	○ 2.85	× 3.80	-
W Φ20 μm	2.43	△ 3.65	-	-
Cu Φ30 μm	2.73	△ 4.10	-	-

observed even when the number of wires increased up to 5. For 25 μm-diameter copper wires, Z-pinch plasma was observed with three wires, but not with four wires. For 20-μm diameter tungsten and 30-μm diameter copper wires, the X-ray emission is observed or not with three wires from shot to shot. In addition, the X-ray intensity was smaller than when two wires were used.

Figure 5 shows X-ray intensity, X-ray generation time (pinch time), and peak current time as a function of latent heat. Here, the numbers ①～⑫ in Fig. 5 indicate ①W Φ 10 μm, ②Al Φ 25 μm, ③Au Φ 25 μm, ④Cu Φ 25 μm, ⑤three Al Φ 25 μm, ⑥Au Φ 30 μm, ⑦W Φ 20 μm, ⑧four Al Φ 25 μm, ⑨Cu Φ 30 μm, ⑩three Cu Φ 25 μm, ⑪five Al Φ 25 μm, and (12) three W Φ 20 μm, respectively. As seen in Fig. 5, the pinching time tends to increase with the increase of latent heat. It is found that the wire materials with high X-ray intensity, where are surrounded by circles, are aluminum and copper.

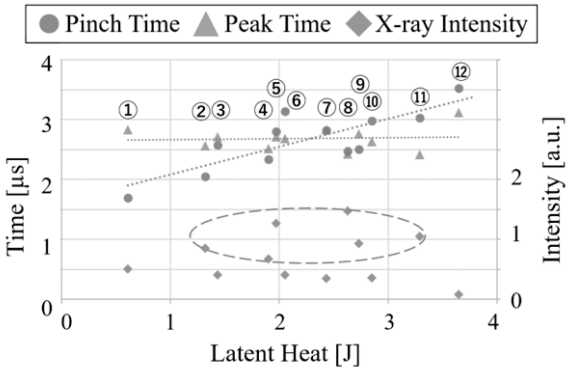

Fig. 5 Pinch time, current peak time and X-ray intensity as a function of latent heat

The current and the Lorentz force $\boldsymbol{J} \times \boldsymbol{B}$ per wire decrease with increasing the number of wires, so it takes longer for the plasma to converge. The generation of pinch plasma was confirmed even when the number of aluminum wires with a diameter of 25 μm increase up to 5 wires. It is obvious from Fig. 5 that the X-ray intensity is relatively high for any number of aluminum wires, and the X-ray intensity tends to increase when 2 to 4 wires are used. It is considered that as the number of wires increases, the plasma density becomes dense and a stronger pinch occurs. However, this explanation is inconsistent with the results for the 20 μm diameter tungsten and 30 μm diameter copper wires, where the X-ray intensity decreases with increasing the number of wires. For these two wires, one possible reason why X-ray intensity does not increase is that the latent heat of each wire is greater than the threshold value for the X-ray generation (2.8 J to 3.3 J).

4. Conclusions

When a current was applied to divergently aligned two Cu wires of 25 μm in diameter, we were able to generate a single-point convergent wire array Z-pinch plasma using a capacitor bank. The formation of pinch plasma depends on the wire material and the wire diameter. It was found that the latent heat of the wire for pinch plasma generation has a critical value of 2.8-3.5 J. In Cu and Al wires, a spatially isolated hot spot was observed and the soft X-ray was emitted more strongly than the other wire materials.

References

[1] A. Vladimir, *et al*., "Examination of a chamber of a large fusion facility by means of neutron activation technique with nanosecond neutron pulse generated by dense plasma focus device PF-6", Fusion Eng. Des., **125**, pp.109–117 (2017). J

[2] Bailey *et.al.,* "Gas-puff Z pinches with D_2 and D_2 - Ar mixtures", Appl. Phys. Lett. 40, 460 (1982)

[3] G. H. Mileyet al., "Inertial-Electrostatic Confinement Neutron/Proton Source", *Proc. 3rd Int. Conf. on Dense Z-pinches*, AIP Press, pp.675–688 (1994).

[4] K. Yamauchi *et.al.,* "Neutron Production Characteristics and Emission Properties of Spherically Convergent Beam Fusion", *Fusion Technol.*, **39**, 3, pp.1182–1187 (2001).

Relationship between Electron Beam Behavior and Output Microwave Characteristics in Virtual Cathode Oscillator

Ryotaro Hasegawa, Yuito Tanaka, Hiroaki Ito, and Taichi Takezaki

Department of Electrical and Electronic Engineering, University of Toyama

ABSTRACT

A virtual cathode oscillator is one of the most promising high-power microwave sources. The virtual cathode oscillator has the attribute of high-power capability, wide frequency tuning ability, and conceptual simplicity, whereas it has difficult problems with a low microwave conversion efficiency of less than 12% and frequency stability. To overcome those problems, experimental and simulation studies on the virtual cathode oscillator have been conducted worldwide over the last four decades. In this study, to investigate the microwave oscillation mechanism in the virtual cathode oscillator, the output microwave characteristic and electron beam currents contributing to microwave generation were measured by using three types of stainless-steel meshes with different transparency. In addition, the correlation between the electron beam and the output microwave characteristics was evaluated.

Keywords

High-power microwave, virtual cathode oscillator, vircator, intense electron beam, pulsed power technology,

1. Research Background and Objectives

A virtual cathode oscillator is a microwave generator using a relativistic electron beam. The structure of the virtual cathode oscillator is simpler than other high-power microwave sources, but it is capable of oscillating microwaves of tens of MW to several GW classes [1,2]. High-power microwaves are expected to be applied in various fields, such as wireless power transmission technology to generate solar power in space and transmit that power to the earth wirelessly, and plasma heating for nuclear fusion fuel [3,4]. However, there is a problem that the microwave conversion efficiency is remarkably low, and research has been conducted to improve the efficiency.

Previous studies suggested that the microwave output from the virtual cathode oscillator is greatly affected by the electron beam [5]. However, the current flowing into the metal mesh has not been taken into account as one of the parameters for studies on the correlation between an electron beam and an output microwave in the virtual cathode oscillator. In this study, the diode current, leakage current through the virtual cathode, and current through the mesh electrode were measured by using three different types of stainless-steel meshes with different transparency. In addition, the correlation between the electron beam and the output microwave characteristics was evaluated by these currents.

2 Principle of Virtual Cathode Oscillator

Figure 1 shows a schematic diagram of the principle of microwave generation in the virtual cathode oscillator. The virtual cathode oscillator consists of a cathode and a meshed anode. When a negative high-voltage pulse is applied to the cathode, electrons are ejected from the cathode surface due to the electric field concentration. The electrons are accelerated toward the mesh anode by the electric field between the cathode and the anode and pass through the anode into the drift space. When the electron current in the drift space exceeds the space charge limit current, a virtual cathode, where the potential is almost the same as the cathode, is formed and most of the electrons in

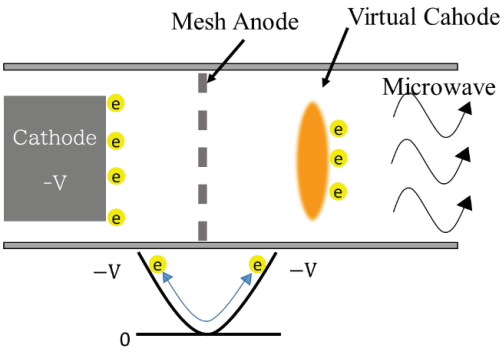

Fig. 1 Principle of Operation of Virtual Cathode Oscillator

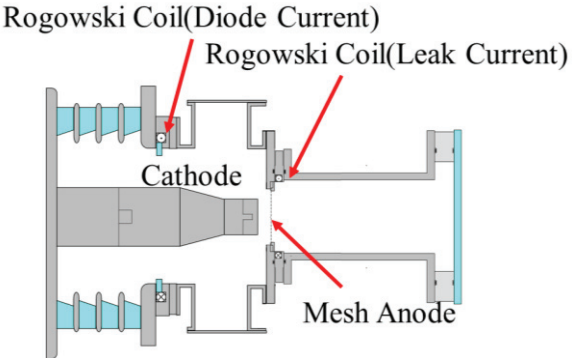

Fig. 2 Experimental setup

the beam are reflected back. In reality, some electrons are not reflected by the virtual cathode and leak into the drift space. Once the virtual cathode is formed, the subsequent electrons move back and forth between the real and virtual cathodes. Thus, microwaves are generated by the oscillating motion of the electrons. The microwave frequency is given by approximately the electron bounce frequency. The virtual cathode is also an unstable area maintained by a subsequent electron beam. Therefore, microwaves are generated when the virtual cathode itself oscillates temporally and spatially. The virtual cathode oscillator has the above two microwave oscillation mechanisms.

3. Experimental setup

A high-voltage pulsed power system, which consists of a Marx generator, a single pulse forming line (PFL), a SF_6 gas spark gap, and a pulse transmission line (PTL), was used as the power supply in this study. The PFL is filled with deionized water as a dielectric and has a characteristic impedance of 3 Ω, and an electrical length of 50 ns. The pulsed power system was operated in negative-output mode and the output voltage of the Marx generator was set to 384 kV. The high-voltage pulse was applied to the cathode of the electron beam diode.

Figure 2 shows the cross-sectional view of the experimental setup for the axially-extracted virtual cathode oscillator. Polyester fiber velvet was used as the electron emitter. Stainless-steel meshes with three kinds of transparency of 49.0 %, 64.5 %, and 74.4 % were used as the anode. The gap distance (d_{AK}) between the anode and cathode electrodes was changed from 7 to 11 mm with the step of 1 mm.

The diode voltage V_d and the diode current I_d were measured using a resistive $CuSO_4$ voltage divider at the end of the PTL and a Rogowski coil located at the upstream of the anode, respectively. The leak current I_l leaking due to electrons leaking through the virtual cathode into the free space was estimated by placing the Rogowski coil between the meshed anode and the virtual cathode.

The microwave from the vircator traveled along a circular waveguide of 100 mm in diameter and 375 mm in length and is emitted into a free space through an acrylic window. All microwave measurements were carried out with the receiving antenna placed on the central axis at a distance of 0.7 m away from the vircator window. The open-ended rectangle waveguide (WR187) was utilized as the receiving antenna. The temporal waveform of the microwave was measured by a high-speed digital oscilloscope with a sampling rate of 40 GS/s and a frequency band of 12 GHz through a coaxial RF cable. The oscillation frequency of the emitted microwave was evaluated by the time-dependent frequency analysis (TFA) [6] of the received temporal waveform. The output microwave was also detected by using a crystal diode and recorded together with the diode voltage and current by a digital oscilloscope with a bandwidth of 200 MHz and a sampling rate of 2 GS/s.

4. Experimental Results

Figure 3 shows typical output waveforms when the virtual cathode oscillator was operated with the gap

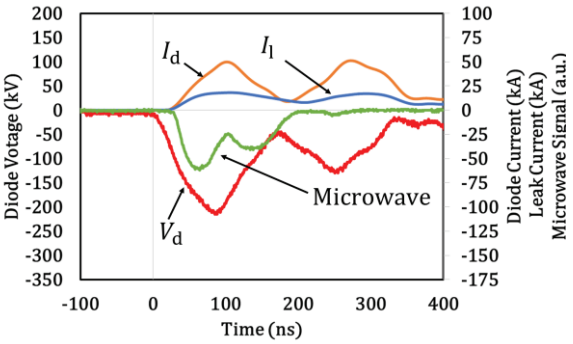

Fig. 3 Typical waveform at $d_{AK} = 9$ mm and mesh transparency of 74.4 %

distance of $d_{AK} = 9$ mm and mesh transparency of 74.4 %. The peaks of diode voltage and diode current were $V_d = 215$ kV and $I_d = 52$ kA, respectively. The pulsed microwave with a pulse duration of $\tau = 165$ ns was observed. Figure 4 shows the TFA (time-dependent frequency analysis) results of the output microwave frequency to investigate the time variation of the microwave spectrum. As seen in this figure, the oscillation frequency of the output microwave shifts up with time. Figure 5 shows the rise in an oscillation frequency $\Delta f/\Delta t$ as a function of the gap distance for different mesh transparency. It turns out from this result that the shift in the frequency of the microwave becomes smaller with the increase in the gap distance and with the decrease in the mesh transparency. Figure 6 shows the dependence of the gap distance on the pulse duration of the output microwave for different mesh transparency. The results show that the microwave duration becomes longer as the mesh transparency increases. The output microwave has the

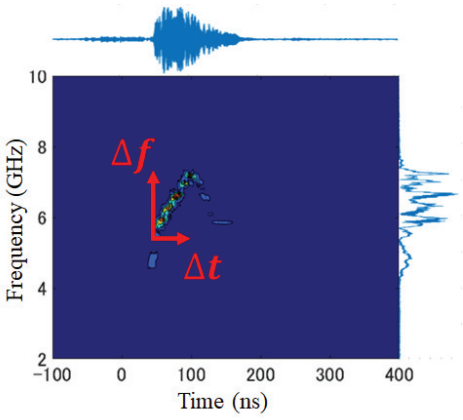

Fig. 4 TFA result of output microwave

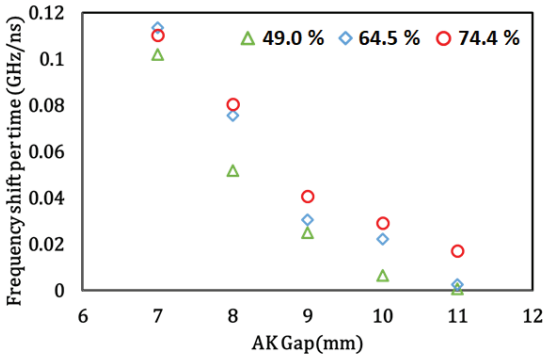

Fig. 5 Shift in frequency $\Delta f/\Delta t$ as a function of gap distance for different mesh transparency

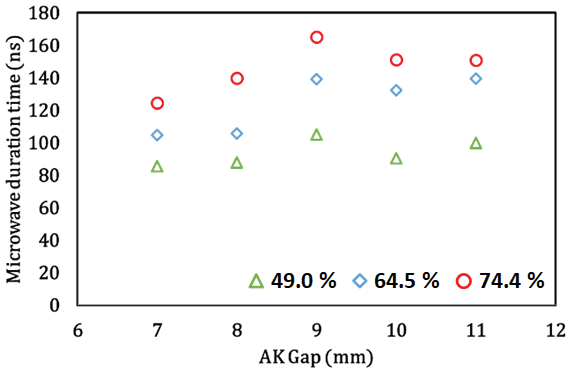

Fig. 6 Microwave duration as a function of gap distance for different mesh transparency

longest pulse duration of 165 ns at $d_{AK} = 9$ mm and the transparency of 74.4 %.

Next, we calculated the leak current I_l passing into free space by taking into account the mesh transparency and estimated the amount of charge that contributes to microwave oscillation. Figure 7 shows the typical waveforms (Fig.3) and the leak current, where the gap distance is $d_{AK} = 9$ mm and the mesh transparency is 74.4 %. By integrating the shaded area with time, we calculated the amount of charge during microwave radiation. Figure 8 shows the dependence of the gap distance on the charge amount for different mesh transparency. It is found from Fig. 8 that the amount of charge decreases as the mesh transparency decreases or the gap distance increases.

Figure 9 shows the microwave frequency shift $\Delta f/\Delta t$ as a function of the charge amount for different mesh transparency. In the case of a large charge amount, the microwave frequency time shift becomes larger. The plasma density in the virtual cathode

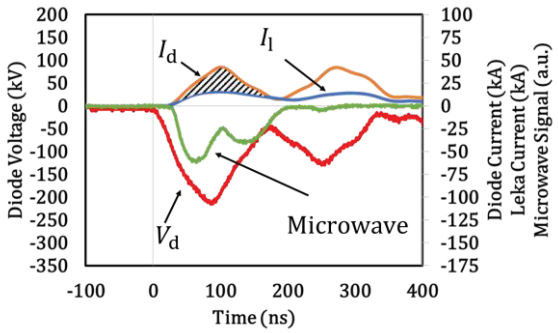

Fig. 7 Typical waveforms and leak current I_l at $d_{AK} = 9$ mm and transparency of 74.4 %

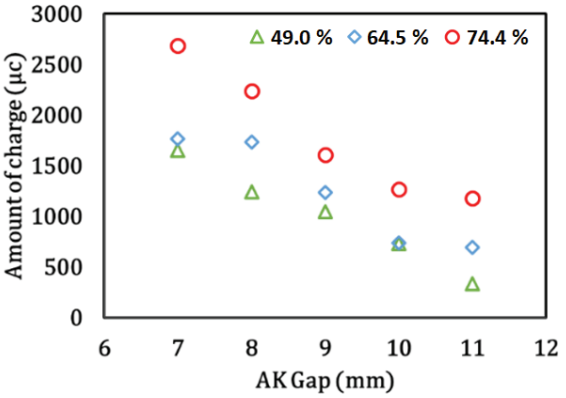

Fig. 8 Dependence of gap distance on charge amount for mesh transparency

increases due to the large charge amount. Therefore, the potential of the virtual cathode enhances, leading to a larger time shift in the oscillation frequency.

Figure 10 shows the relationship between the pulse duration of the output microwave and the amount of charge. In the case of the mesh transparency of 74.4 %, the microwave duration is longer than that of 49.0 % and 64.5 % because the amount of charge is larger. We found that there was a correlation between the microwave duration and the amount of charge. However, even if the amount of charge is equal, it is necessary to know the optimal amount of charge for the gap distance in order to extend the microwave duration, since the pulse duration of the microwave depends on the gap distance and the mesh transparency.

5. Summary

We investigated the characteristic of the output microwave and electron beam current in the virtual cathode oscillator by changing the gap distance and the

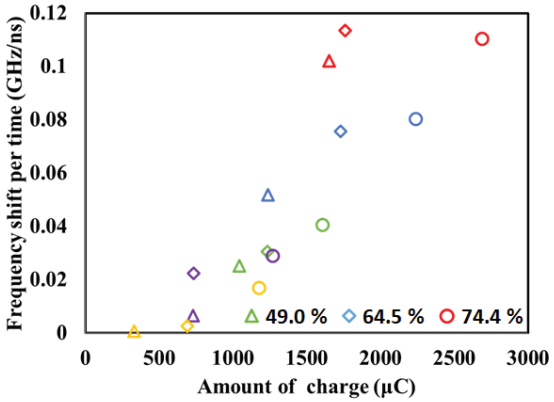

Fig. 9 Dependence of charge amount on microwave frequency shift $\Delta f/\Delta t$ for mesh transparency

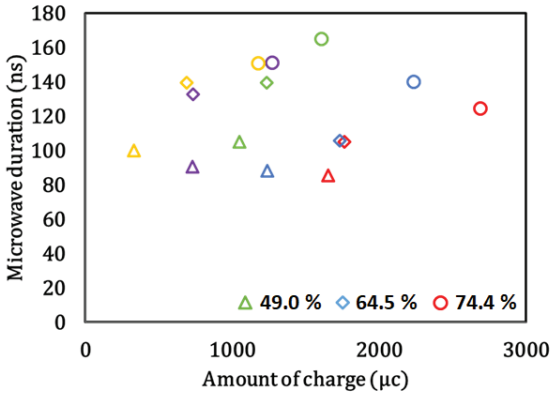

Fig. 10 Dependence of charge amount on microwave pulse duration for mesh transparency

transparency of the meshed anode. We found a correlation between the amount of charge and the frequency of the output microwave. When the amount of charge is large, the oscillation frequency shifts up significantly with time. The experimental results showed that the pulse duration of the microwave became longer when the amount of charge was large. The microwave with the longest pulse duration of 165 ns was observed at mesh transparency of 74.4 % and a gap distance of $d_{AK} = 9$ mm.

Acknowledgment

This work was partially supported by JSPS KAKENHI Grant Number JP19H02126.

References

[1] J. Benford, “Space Applications of High-Power Microwaves,” IEEE Trans. Plasma Sci. 36, 569–

581 (2008).

[2] J. Benford, J. Swegle, and E. Schamiloglu, High Power Microwaves, 2nd ed. (Taylor & Francis, Boca Raton, 2007).

[3] S. H. Gold and G. S. Nusinovich, “Review of high-power microwave source research,” Rev. Sci. Instrum., vol. 68, pp. 3945–3974 (1997).

[4] J. Benford, J. Swegle, and E. Schamiloglu, “High Power Microwaves” 3rd ed., New York: Taylor & Francis (2016).

[5] A. E. Hramov, S. A. Kurkin, A. A. Koronovskii, and A. E. Filatova “Effect of self-magnetic fields on the nonlinear dynamics of relativistic electron beam with virtual cathode” Physics of Plasmas 19, 112101 (2012).

[6] W. Jiang, “Time-frequency analysis of virtual cathode oscillator,” IEEE Trans. Plasma Sci. 38, 1325-1328 (2010).

Line profile modeling for unresolved satellite lines of nitrogen Balmer-α using NISEM (noninteracting spectator-electron model) for radiation transport calculation

Shoto Ito, and Tohru Kawamura

Department of Physics, School of Science, Tokyo Institute of Technology

ABSTRACT

Hydrogen-like nitrogen Balmer-α (N-Baα) is one of the candidates for extreme ultraviolet laser light sources. According to the previous studies, it is necessary to solve a radiation transport equation with a large number of unresolved satellite lines for good lasing conditions since the satellite lines affect the creation of population inversion. To estimate line profiles of the satellite lines, a model of distributions of satellite lines approximated to be Gaussian functions is adopted. Since the number of satellite lines with a high-lying spectator electron is more than several thousand, resultant line profiles of the satellite lines can be effectively treated in the calculation of radiation transport.

Keywords

hydrogen-like nitrogen, spectator electron, extreme ultraviolet, satellite lines, radiation transport equation

1. Introduction

The extreme ultraviolet (EUV) light, of which wavelength is from about 10 nm to 124 nm [1], is studied recently. Hydrogen-like nitrogen Balmer-α (N-Baα) is one of the candidates for EUV light sources. Hydrogen-like ions have only one bound electron, and Balmer-α is a transition between $n = 2$ and $n = 3$ where n is a principal quantum number [2]. EUV light sources are expected to be applied to photolithography, which is microfabrication for circuit patterns on silicon wafers [3]. The transition energy of N-Baα is approximately 92.6 eV, and the wavelength is 13.4 nm [4].

Unresolved satellite lines of N-Baα affect the creation of population inversion of N-Baα. They are emission of doubly excited ions, for example the emission from $3sn\ell$-$2pn\ell$ transition, where ℓ is an azimuthal quantum number. Ozawa *et al*. [5] discussed that dielectronic-capture ladderlike excitation and deexcitation processes (DL processes) [6] have a large effect on the populations of $n = 3$ and 2. The DL processes contain doubly excited states implicitly. Taking into account Ozawa's result, Tatsumura *et al*. [7,8] solved a rate equation, explicitly considering doubly excited states, and discussed that stimulated emission of unresolved satellite lines affects the population inversion for N-Baα.

Solving a radiation transport equation with the satellite lines is required for the net estimation of the N-Baα laser intensity. The radiation transport equation is to calculate the emission and absorption of radiation in plasma [9] given by

$$\frac{1}{c}\frac{\partial I_\nu}{\partial t} + \frac{\partial I_\nu}{\partial r} = j_\nu - \kappa_\nu I_\nu \,, \qquad (1)$$

where c is light speed, j_ν and κ_ν are emissivity and opacity, respectively. Solving such an equation with unresolved satellite lines is quite challenging due to the huge number of the satellite lines, and those considered in the present study are 4092 lines.

2. Line profile modeling using NISEM (noninteracting spectator-electron model)

In this study, discussed are the satellite lines of nitrogen Balmer-α with a spectator electron of which

principal quantum number n_{spc} is 7–9. The number of satellite lines is 4092.

NISEM proposed by Honda *et al.* [10] can reduce the amount of transition line to explicitly handle. In this model, a large number of satellite lines are considered to be distributed in a Gaussian form. There are three quantities to identify the Gaussian functions: Average Energy Shift (AES), Energy Root Mean Square Spread (ERMSS), and Sum of Einstein's A coefficient (SEA).

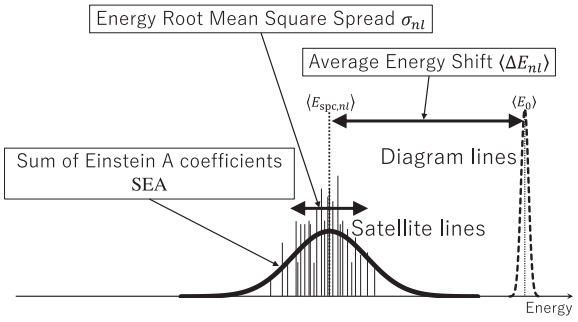

Fig. 1 Schematic drawing of a Gaussian function produced by NISEM. Dashed curve: diagram lines, thin vertical bars: satellite lines, bold Gaussian curve: NISEM profile.

AES $\langle E_{nl} \rangle$ is calculated by Eq. (2):

$$\langle E_{nl} \rangle = \langle E_0 \rangle - \langle E_{\mathrm{spc},nl} \rangle , \qquad (2)$$

$$\begin{cases} \langle E_0 \rangle = \dfrac{\sum_i A_{i0} E_{i0}}{\sum_i A_{i0}} , \\ \langle E_{\mathrm{spc},nl} \rangle = \dfrac{\sum_i A_{\mathrm{spc},nl,i} E_{\mathrm{spc},nl,i}}{\sum_i A_{\mathrm{spc},nl,i}} , \end{cases}$$

where E_{i0} and A_{i0} are the ith emission energy and the Einstein's A coefficient without spectator electrons, and $E_{\mathrm{spc},nl,i}$ and $A_{\mathrm{spc},nl,i}$ are the i th emission energy and the Einstein's A coefficient with a spectator electron of which orbital is $n\ell$, respectively. Equation (3) is the definition of ERMSS σ_{nl}:

$$\sigma_{nl} = \left(\frac{\sum_i A_i (E_i - E_{\mathrm{ave}})}{\sum_i A_i} \right)^{\frac{1}{2}} , \qquad (3)$$

where E_{ave}, E_i, and A_i are the averaged emission energy of satellite lines, the ith emission energy and the Einstein's A coefficient with a spectator electron of which orbital is $n\ell$. SEA is calculated by the summation of Einstein's A coefficients with a spectator electron of which orbital is $n\ell$.

The 4092 satellite lines can turn 72 Gaussian functions by calculating the three quantities for 24 spectator electrons (7ℓ–9ℓ). In addition, there are 3 Balmer-α transitions: 3*d*-2*p*, 3*p*-2*s*, and 3*s*-2*p* to be 72 Gaussian functions in total. In the calculation, satellite lines of $\ell_{\mathrm{spc}} = 8$ were replaced by those of $\ell_{\mathrm{spc}} = 7$ because GRASP2 [11,12] calculations for the orbital failed and the profile for $\ell_{\mathrm{spc}} = 8$ may be similar to that for $\ell_{\mathrm{spc}} = 7$.

3. Results and Discussion

3.1 Calculation Results

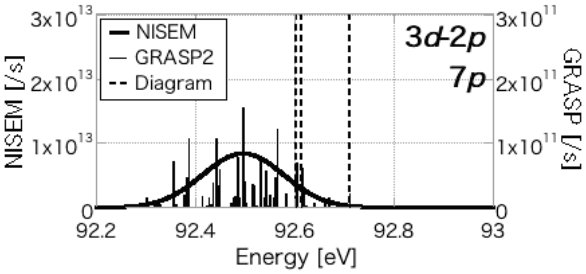

Fig. 2 Einstein's A coefficients vs. transition energies of 3*d*7*p*-2*p*7*p* transitions.

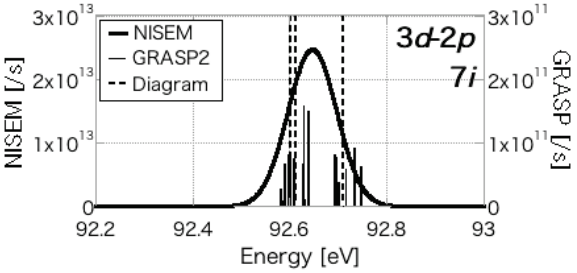

Fig. 3 Einstein's A coefficients vs. transition energies of 3*d*7*i*-2*p*7*i* transitions.

In Figs. 2–3, typical results of NISEM calculation are given, the bold Gaussian curves are by NISEM, and the thin vertical bars are satellite lines, and the three dashed vertical lines are diagram lines standing for $3d_{3/2}$ - $2p_{3/2}$, $3d_{5/2}$ - $2p_{3/2}$, and $3d_{3/2}$ - $2p_{1/2}$ from the left-side. In Fig. 2, which is for 3*d*7*p*-2*p*7*p*, the distribution of satellite lines can be almost

approximated by the shape of a Gaussian function. On the other hand, in Fig. 3, which is for $3d7i$-$2p7i$, the distributions cannot be done with the functions due to the split two distributions of the satellite lines.

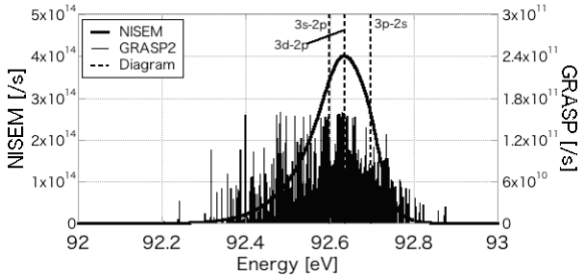

Fig. 4 Einstein's A coefficients vs. transition energies of which Balmer-α and satellite lines with a spectator electron (n_{spc} =7–9).

In Fig. 4, the curve is a line profile superposed with 72 NISEM Gaussian functions, the thin vertical bars are 4092 satellite lines, and the dashed vertical lines are diagram lines: 3*s*-2*p*, 3*d*-2*p*, and 3*p*-2*s* shown in the figure. The shape of the NISEM profile can express the distribution of satellite lines. The more NISEM Gaussian functions are superposed, the more the profile is similar to the distribution of the satellite lines. The split distribution, such as shown in Fig. 3, does not matter due to the superposition with other satellite lines.

3.2 Discussion

The split distribution in Fig. 3 is attributed to the difference of the total angular momentum quantum number j. The three quantities of NISEM are calculated in the framework of $n\ell$-scheme, *i.e.*, the NISEM Gaussian function does not account for the difference of j, thus the distributions are not similar to the functions.

As shown in Fig. 4, the superposition of the distributions can fill the split features. The energy separation of the split is in the order of 0.1 eV. Thus, the split is buried and obscured by the superposition of 72 distributions.

NISEM can be also used in $n\ell$-scheme for ions with smaller atomic numbers, such as nitrogen. In the paper [10], NISEM was applied to gold ions in jj-scheme and the atomic number is 79. In this case, the effect of jj-coupling is much larger and the grouping of the satellite lines must be done according to the energy separation.

4. Development of a radiation transport calculation code

In the previous studies, the radiation transport equation for N-Baα without satellite lines [13] and the rate equation for N-Baα with satellite lines [8] have been solved. It has been found that the intensity of N-Baα is greater than 10^{12} W/cm^2/nm by solving the radiation transport equation. Furthermore, the results of the rate equation have shown that the satellite lines affect the creation of the population inversion for N-Baα when the intensity of N-Baα is greater than 10^{12} W/cm^2/nm. These results lead to the necessity of the radiation transport calculation with satellite lines.

The approximation for line profiles by NISEM allows us to easily see the interference between diagram and unresolved satellite lines.

5. Conclusions

In this study, the NISEM profiles of N-Baα work well to express the distribution of unresolved satellite lines. The superposition of the NISEM Gaussian functions in $n\ell$-scheme can approximate the distribution of the satellite lines. The split features of the distributions due to the differences of total angular momentum quantum number can be ignored for low atomic number ions like nitrogen. NISEM can explicitly reduce the amount of transition lines handled in radiation transport calculation since 4092 satellite lines can be modeled to be 72 Gaussian functions.

In the future, to obtain the net intensity of N-Baα, radiation transport calculation considering unresolved satellite lines modeled by NISEM will be done.

References

[1] M. W. Zürch, "High-Resolution Extreme Ultraviolet Microscopy", Springer (2015).

[2] J. J. Balmer, "Notiz über die Spectrallinien des Wasserstoffs", *Annalen der Physik und Chemie*

Third, **25**, pp.80–87 (1885).

[3] X. Ma *et al*., "Computational Lithography", *Wiley series in pure and applied optics*, John Wiley & Sons, Inc. (2010).

[4] A. Kramida *et al.*, "NIST Atomic Spectra Database (ver. 5.8)", National Institute of Standards and Technology (2020).

[5] T. Ozawa *et al.*, "Lasing of extreme ultraviolet light with nitrogen plasma in a recombining phase―Roles of doubly excited states", *Phys. Plasmas*, **19**, 063302 (2012).

[6] T. Fujimoto *et al.*, "Enhancement of the excitation and deexcitation rate coefficients of ions in dense plasmas: The role of autoionizing states", *Phys. Rev. A*, **32**, 3, pp.1663–1998 (1985).

[7] N. Tatsumura *et al.*, "Effects of unresolved satellite lines on lasing of extreme ultraviolet light with nitrogen plasma in a recombining phase", *Phys. Plasmas*, **20**, 083304 (2013).

[8] N. Tatsumura *et al.*, "Erratum: "Effects of unresolved satellite lines on lasing of extreme ultraviolet light with nitrogen plasma in a recombining phase" [Phys. Plasmas 20, 083304 (2013)]", *Phys. Plasmas*, **20**, 099902 (2013).

[9] D. Salzman, "Atomic Physics in Hot Plasma", *International Series of Monographs on Physics No.97*, Oxford University Press (1998).

[10] K. Honda *et al.*, "M-shell x-ray spectra of laser-produced gold plasmas", *Phys Rev E*, **55**, 4, pp.4594–4601 (1997).

[11] I. P. Grant, "Relativistic calculation of atomic structures", *Adv. Phys.*, **19**, pp.747–811 (1970).

[12] K. Dyall *et al.*, "GRASP: A general-purpose relativistic atomic structure program", *Comput. Phys. Commun.*, **55**, pp.425–456 (1989).

[13] T. Yoshikawa, bachelor thesis, Tokyo Institute of Technology (2017).

Analysis of Inertial Electrostatic Confinement Plasma Using One-Dimensional PIC-MCC Simulation

Kazuhiro Matsuda, Jun Hasegawa

Laboratory for Zero Carbon Energy, Institute of Innovative Research, Tokyo Institute of Technology

ABSTRACT

Particle motions inside an inertial electrostatic confinement (IEC) fusion neutron source is analyzed using the one-dimensional Particle-In-Cell Monte-Carlo-collision (PIC-MCC) method. In the analysis, five kinds of ion/neutral particle species (H_2^+, H^+, H^{3+}, H_2, H) as well as electrons are considered. The simulation results are compared with the experimentally obtained relationship between background H_2 gas pressure and discharge sustaining voltage as well as the Hα spectrum observed from the axial direction of the IEC device. We found that the heat load to the cathode was mostly given by H_2^+ and that to the cathode was mostly given by electrons.

Keywords

Neutron Source, Inertial Electrostatic Confinement Fusion, Glow Discharge, PIC-MCC Simulation

1. Introduction

Neutrons are one of the nucleons that compose the atomic nucleus together with protons and has no electric charge. Therefore, neutrons do not interact electromagnetically with charged particles and have very high material permeability. X-rays are also well known as radiation with high material permeability, but there is a big difference in the manner that they interact with matter. X-rays lose energy mainly by interacting with electrons in the atom, so they are well shielded by atoms with large atomic numbers. In contrast, neutrons lose their kinetic energy due to elastic collisions particularly with small atomic nuclei, so they are well shielded by atoms with small atomic numbers. X-rays is easily generated by irradiating a solid target with an electron beam of several keV to several tens of keV. On the other hand, to generate neutrons, we need to use nuclear reactions. Therefore, while X-rays have been commercially used in various applications such as X-ray radiography and baggage inspection at airports, the industrial use of neutrons has been limited.

In recent years, the application of neutron rays in various fields is expanded with the development of accelerator-driven high-intensity neutron sources such as J-PARC and Riken RANS. High-intensity neutron sources based on huge particle accelerators and nuclear fission reactors can provide neutron production rates (NPR) more than 10^{13} neutron/s, but costs of construction and operation are extremely high. On the other hand, neutron sources using radioisotopes such as ^{252}Cf are less intense than other neutron sources, despite their high management costs.

Inertial electrostatic confinement (IEC) fusion neutron sources are small, inexpensive, and highly

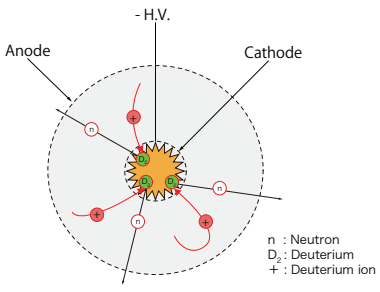

Fig. 1 Principle of inertial electrostatic confinement fusion.

portable neutron sources. In the IEC fusion neutron source, deuterium ions are generated by glow discharge in low-pressure (~1 Pa) deuterium gas. After accelerated by the electric field between the electrodes, some deuterium ions and neutral particles collide with deuterium molecules (D_2) in the background gas and cause D-D fusion reactions to generate 2.45-MeV neutrons.

One of the most important issues of the IEC fusion neutron source is improving the neutron production rates (NPR). NPRs of ~10^8 n/s have been achieved in previously developed IEC D-D fusion neutron sources. To achieve NPRs more than 10^9 n/s, it is inevitable to increase the electric input power, which probably brings serious problems to the discharge electrodes due to excessive heat load originating from high-energy particle bombardment. Therefore, it is very important to understand the behavior of energetic particles in the IEC device and feedback that knowledge to the device design. Our research group has also developed a linear-type IEC device[1] and been studying particle behavior in the device by combining Doppler spectroscopy and numerical analyses based on Monte-Carlo particle tracking. In those analyses we assumed vacuum potential between electrodes because the degree of ionization of background gas in the IEC device was typically quite low. However, if the input power is increased, the potential modulation due to the space charge effect will be remarkable. In this study, numerical analysis including space-charge effects is performed by an originally developed one-dimensional simulation code based on the Particle-In-Cell Monte-Carlo-Collision (PIC-MCC) method, and we aim to clarify the energy distributions of energetic particles that bombard the electrodes and deposit heat to them.

2. Simulation model

The PIC-MCC code developed in this study treats five kinds of ion/neutral particle species (H_2^+, H_2, H^+, H, and H_3^+) as well as electrons. As for neutral particles such as H_2 and H, only fast particles generated by charge exchange reactions are tracked.

Table 1. Collisional processes in MCC method.

$e+H_2 \rightarrow$(elastic) $e+H_2 \rightarrow 2e+H_2^+$	$H^++H_2 \rightarrow$e(total) $H^++H_2 \rightarrow$fast H $H^++H_2 \rightarrow H\alpha$ ($D^++D_2 \rightarrow$D-D fusion)
$H_2^++H_2 \rightarrow$e(total) $H_2^++H_2 \rightarrow$slow H_2^+ $H_2^++H_2 \rightarrow$fast H^+ $H_2^++H_2 \rightarrow H_3^++H$ $H_2^++H_2 \rightarrow H\alpha$ ($D_2^++D_2 \rightarrow$D-D fusion)	$H+H_2 \rightarrow H_2^+$ $H+H_2 \rightarrow$fast H^+ $H+H_2 \rightarrow H\alpha$ ($D+D_2 \rightarrow$D-D fusion)
$H_2+H_2 \rightarrow$fast H^+ $H_2+H_2 \rightarrow H\alpha$ ($D_2+D_2 \rightarrow$D-D fusion)	$H_3^++H_2 \rightarrow$fast H^+ $H_3^++H_2 \rightarrow$fast H_2^+ $H_3^++H_2 \rightarrow H\alpha$ ($D_3^++D_2 \rightarrow$D-D fusion)

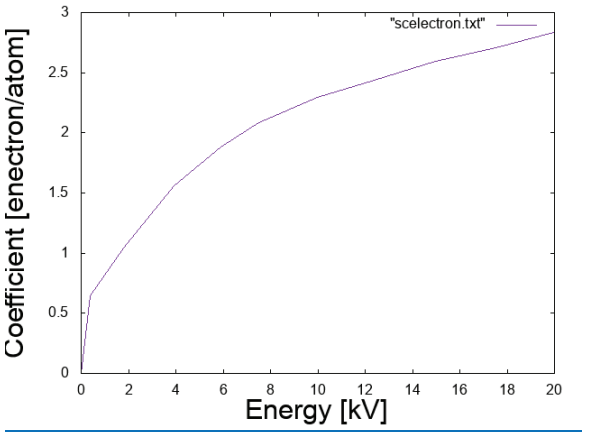

Fig. 2 Secondary electron emission coefficient. [4]

Table 1 summarizes collisional processes considered in this study. To calculate the probabilities of these collisions, we used the cross-section data compiled by Tabata, *et al.*[2,3] In addition to the above collisional processes, backscattering of electrons that collide the anodes and secondary electron emission from the cathodes due to bombardment of energetic ions, neutral atoms and molecules. [4,5]

In this analysis the electrodes are assumed to be parallel flat plates arranged in the order of anode, cathode, and anode. The distances between the anode and the cathode are 0.2 m. The probability of particle transmission through the center cathode was assumed to be constant. To reproduce stable discharge in the numerical analysis, the applied voltage was feedback controlled so that constant discharge current flow between the cathode and the anodes.

3. Results and Discussion

3.1 Discharge sustaining voltage

The relationship between background gas pressure and discharge maintenance voltage was investigated. As shown in the Fig. 3, the discharge sustaining voltage tends to decrease with increasing background gas pressure from 0.3 Pa to 1.0 Pa. This tendency well agree with the experimental result shown in the figure.

3.2 Hα spectrum

The spectral intensity profile of Hα emission was numerically predicted from the axial velocity distribution of fast hydrogen atoms in the PIC-MCC simulation. As shown in Fig. 4, the central peak and the left and right Doppler peaks observed by the experiment were well reproduced also in the simulation. The inflection points on the spectral curve around 653 nm and 659 nm were also reproduced.

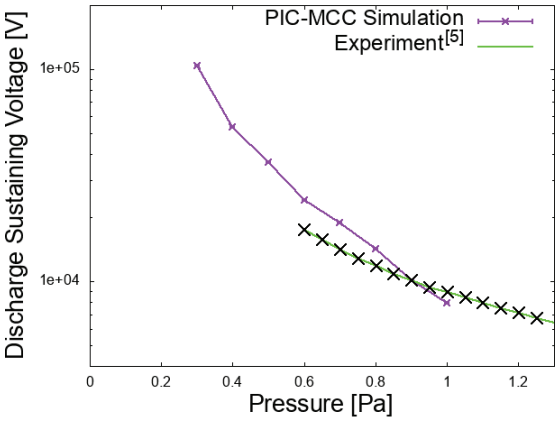

Fig. 3 Pressure dependence of discharge sustaining voltage.

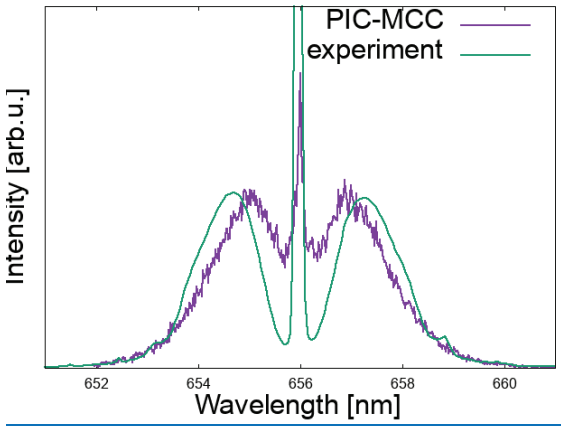

Fig. 4 Hα spectra observed with a discharge voltage of 20 kV. [6]

The qualitative agreement between the numerical analysis and the experiment shows the correctness of our present analytical method to some extent.

3.3 Internal state of IEC device

In Fig. 5, the populations of the particles present on the simulation space are plotted as a function of time. As for H_2 and H, only fast particles produced by charge exchange reactions were counted in this plot. After the calculation starts, the number of ions and neutral particles increases rapidly due to the ionization and charge exchange reactions, and eventually reaches the equilibrium values.

Figure 6 shows the energy distribution of the particles (e, H, and H_2) colliding with the anodes at a discharge sustaining voltage of about 25 kV. The electron energy distribution deviates significantly from the Maxwell-Boltzmann distribution because most of the secondary electrons are accelerated from the cathode to the anode without collision. From these results, we found that 86% of the total thermal deposition on the anodes was due to electrons.

The energy distribution of the particles colliding with the cathode was shown in Fig. 7. The kinetic energy of most particles is much smaller than the energy equivalent to the applied voltage (~25 kV). The particle species that gave the highest heat load to the cathode was H_2^+, which accounted for about 54% of the total. The heat loads due to the other particles were ~17% for H_2, ~17% for H^+, and ~10% for H.

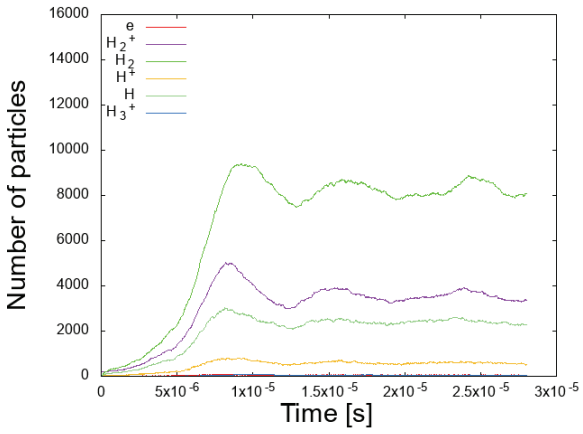

Fig. 5 Time variation of the number of each particle.

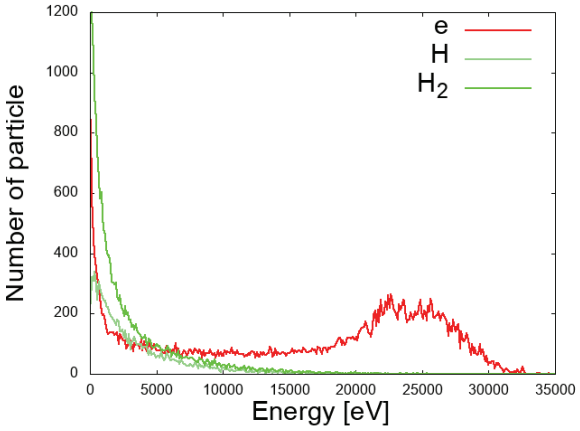

Fig. 6 Energy distribution of particles colliding with anodes.

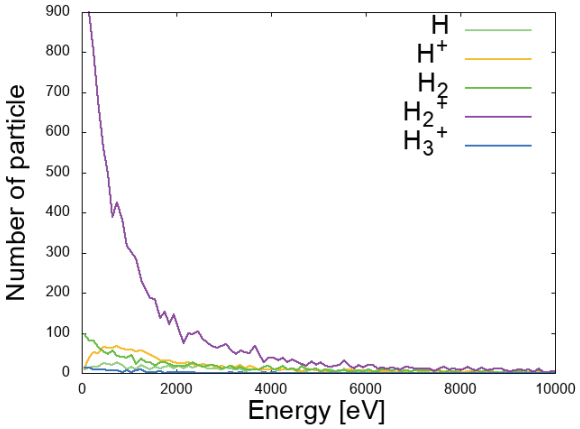

Fig. 7 Energy distribution of particles colliding with cathode.

4. Conclusions

In this study, we analyzed particle kinetics in glow discharge in the linear-type IEC device operated with background gas pressures from 0.3 Pa to 1.0 Pa by using an originally developed 1D PIC-MCC code. The dependence of the discharge sustaining voltage on the background gas pressure, which was predicted by the simulation, showed a good agreement with the experiment. The numerically predicted Hα spectrum including the Doppler shift qualitatively reproduced the experimentally observed one. We found that the heat load on the anodes is mainly provided by energetic electrons and the influence of high-energy atoms and molecules is relatively small. On the other hand, the heat load on the cathode was found to be due mainly to H_2^+ ions.

References

[1] J. Hasegawa, E. Hotta, K. Takakura, and H. Miyadera, "Recent progress on inertial electrostatic confinement fusion neutron sources", *Reza Kenkyu*, **46**(10), 589–593 (2018) (in Japanese).

[2] T. Tabata and T. Shirai, "Analytic cross sections for collisions of h+, h2+, h3+, h, h2, and h-with hydrogen molecules", *Atomic Data and Nuclear Data Tables*, **76**(1), 1–25 (2000).

[3] J.S. Yoon, M.Y. Song, J.M. Han, S.H. Hwang, W.S. Chang, and B. Lee, "Cross Sections for Electron Collisions with Hydrogen Molecules", *Journal of Physical and Chemical Reference Data*, **37**, 913, (2008).

[4] E. H. Darlington, "Backscattering of 10-100 keV electrons from thick targets", J*ournal of Physics D: Applied Physics*, **8**, 85–93 (1975).

[5] B. Szapiro, J.J. Rocca and T. Prabhuram, "Electron yield of glow discharge cathode materials under helium ion bombardment", *Appl. Phys. Lett*, **53**, 358–360 (1988).

[6] S. Tabata, "Effects of cathode shape and discharge mode on ion motions in a linear inertial electrostatic confinement device", *Master thesis, Tokyo Institute of Technology* (2020). (in Japanese).

Research on Laser Ablation of Cryogenic CO_2 Targets

Yuji Inoue[1], Jun Hasegawa[1], Takuma Jinnai[1], Kazuhiko Horioka[1],
Kazumasa Takahashi[2], Jun Tamura [3], Ken Takayama[4]

[1]Tokyo Institute of Technology, [2]Nagaoka University of Technology, [3]Japan Atomic Energy Agency,
[4]High Energy Accelerator Research Organization (KEK)

ABSTRACT

The supply characteristics of carbon ions from a laser ion source using a cryogenic carbon dioxide (CO_2) target are investigated with the aim of applying it to the accelerator system of heavy ion cancer therapy that requires highly charged carbon ions. A cryogenic target is generated by sublimating CO_2 gas on the surface of a cylindrical cold head cooled with liquid nitrogen. By irradiating the target with a frequency-doubled Nd:YAG laser, plasmas containing up to C^{4+} ions are generated. Carbon ions are provided stably with a peak fluctuation of about ±10%. Main component of the plasma is found to be carbon ions. The cryogenic target (solid CO_2) is transparent to visible light, requiring us to optimize the focal point positions of the incident laser.

Keywords

Laser ion source, Cryogenic target, Heavy ion cancer therapy

1. Introduction

Heavy ion cancer therapy is a type of radiation cancer treatment using energetic carbon ions. Heavy ions locally deposit their kinetic energy just before they stop in the target (Bragg peak), so they can damage cancer cells deep in the human body more effectively compared to conventional radiotherapy using X-rays, etc.[1] However, because of the high construction cost of the heavy ion accelerator system, the spread of heavy ion cancer therapy to developing countries is still on the way[2].

At present accelerator facilities for heavy ion cancer therapy, C^{4+} are usually generated by conventional plasma ion sources, such as electron cyclotron resonance (ECR) ion sources. After accelerated to several MeV/u by linear accelerators (injector), C^{4+} are converted to C^{6+} by a carbon thin film stripper and then injected to synchrotrons[1]. To reduce the size and cost of the accelerator for heavy ion cancer therapy, Takayama, *et al.* have recently proposed a novel accelerator system based on induction synchrotron, in which a laser ion source is used to supply highly-stripped carbon ions (C^{5+} and C^{6+}) directly to the synchrotron[3]. Munemoto, *et al.*[4] and Fuwa, *et al.*[5] have so far confirmed that highly ionized carbon ions are generated directly from graphite targets by laser ablation. These results indicate that the injector such as RF linear accelerators is not necessary in this novel accelerator system, leading to the reduction of the size and cost of the heavy ion cancer therapy facility.

On the other hand, when a solid target in the laser ion source is repeatedly irradiated by a laser to produce

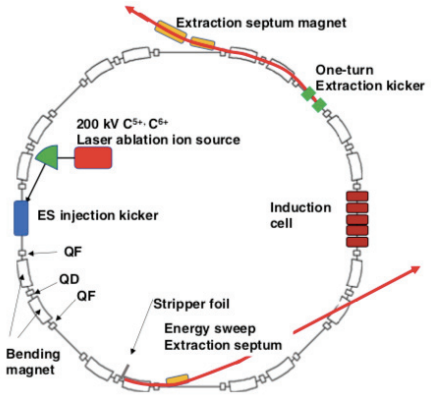

Fig. 1. A next-generation heavy ion cancer therapy accelerator using a laser ion source[3].

source plasma, damage accumulates on the target surface, which makes it difficult to reuse the target for succeeding plasma generation. Thus, one needs to replace the target on a regular basis, which limits the continuous operation time of the laser ion source. Tamura, *et al.,* proposed to generate a plasma from a thin solid neon layer formed on a GM cooler cold head [6]. In this study, to solve the limited lifetime of the solid target of the laser ion source and generate carbon ions repeatedly, we propose to use a cylindrical cryogenic target. In this method, a thin solid layer consisting of gas molecules is formed by sublimation on a metal cylinder cooled with liquid nitrogen, and plasma is generated by irradiating it with a pulsed laser. The sublimation gas layer is locally destroyed and removed after laser ablation, but is regenerated by sublimation of continuously supplied "fuel" gas. The purpose of this study is to develop a novel laser ion source using a cryogenic target and to demonstrate that it can operate stably without a limit on the lifetime of the target. In this paper, we report results of preliminary experiments using a sublimated CO_2 target and describe the properties and reproducibility of plasmas generated by laser irradiation of cryogenic targets.

2. Experimental Setup

Figure 2 shows the experimental equipment used in this study. The equipment is divided into a plasma generation chamber, an ion flux measurement chamber, and an electrostatic energy analyzer. These chambers are evaluated to ~10^{-4} Pa by two sets of turbo molecular pumps.

A cylindrical cryogenic target is located in the plasma generation chamber. The structure of the target is shown in Fig. 3. The target consists of a cylindrical

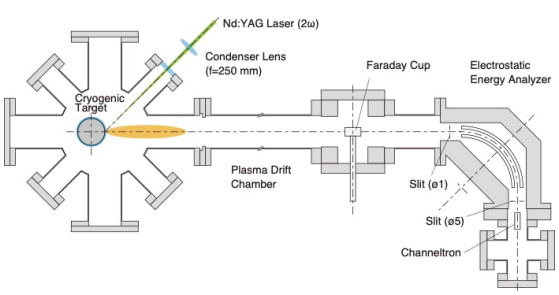

Fig. 2. Experimental setup.

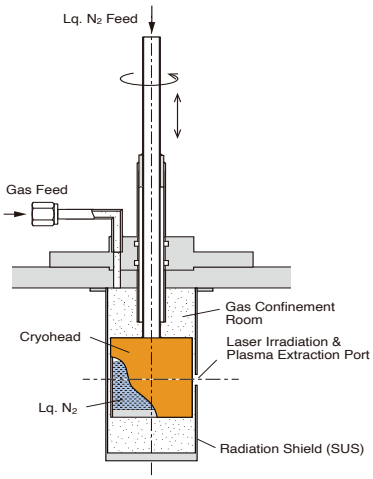

Fig. 3. Structure of the cryogenic target.

cryogenic cold head, a cylindrical radiation shield, and a gas supply system. Both the cryogenic head and the shield are made of stainless steel. To protect the cold head from laser ablation, a 100-μm thin copper sheet covers the side wall of the head.

Plasma generation is performed as follows. First, the surface of the cold head is cooled to ~88 K with liquid nitrogen. Then, by feeding carbon dioxide (CO_2) gas through a mass flow controller into the radiation shield, a sublimation layer of CO_2 is gradually formed on the cold-head surface. After the thickness of the sublimation layer reaches a certain value, the layer is irradiated by a frequency-doubled Nd:YAG laser through a ø5-mm aperture on the radiation shield. Finally, a dense and hot plasma produced by laser ablation is extracted through the aperture into vacuum. Because the sublimation layer is locally removed by laser ablation, the cold head is rotated horizontally by precise motorized stages to avoid the overlap of laser spots on the target. In the present experiment, the pulse energy of the laser was set to 90 mJ. The laser spot size on the target has an elliptical shape with a size of 0.3 mm×? mm. Thus, the laser power density was 1.1×10^{9} W/cm^2.

In the plasma ion flux measurement section, a Faraday cup with an entrance aperture of 5 mm was installed 850 mm away from the laser irradiation surface of the cryogenic target. A bias voltage of –50 V was applied to the cup to measure the ion flux in the laser-generated plasma.

The electrostatic energy analyzer was used for the charge-state analysis of the plasma ions. The analyzer

consists of two cylindrical deflection electrodes, a slit, and a channel electron multiplyer (CEM) detector. Under a specific deflection voltage, only ions with a specific charge-to-mass ratio and a specific kinetic energy can be detected. We measured ion signals with various deflection voltage.

3. Results and Discussion

3.1 Formation of cryogenic target

Figure 4 shows the temporal changes in the plasma generation chamber pressure and the cold head surface temperature during the sublimation layer formation experiment. As shown in the figure, when liquid nitrogen was introduced at time zero ($t = 0$), the surface temperature of the cold head began to decrease and reached ~88 K after ~50 min. The background pressure of the chamber also began to decrease and reached ~10^{-4} Pa. After 1 hour, CO_2 gas supply started at a flow rate of 40 sccm and continued for 25 min. During this period, the surface temperature increased slightly from 88 K due to the latent heat deposited to the head by CO_2 gas sublimation. After stopping the supply of liquid nitrogen and CO_2 gas, CO_2 molecules forming the sublimation layer on the cold head began to be released as gas after a certain time (t = ~260 min). Then, the chamber pressure increased rapidly to ~1 Pa and decreased to ~10^{-4} Pa again with the termination of outgassing from the cold head (t = ~310 min). Assuming a molecular flow in the chamber, the pressure increases linearly with the amount of gas molecules released. Thus, we evaluated the total amount of gas molecules released from the cold head from the pressure history in Fig. 4. When CO_2 gas was supplied with a flow rate of 40 sccm for 25 min (1000 cc in total), the total amount of released gas was about 990 cc, indicating that the most of supplied gas (~99%) sublimated to the cold head. From the total amount of sublimated CO_2 gas, we estimated the thickness of the sublimation layer (solid CO_2 target) to be 100 μm.

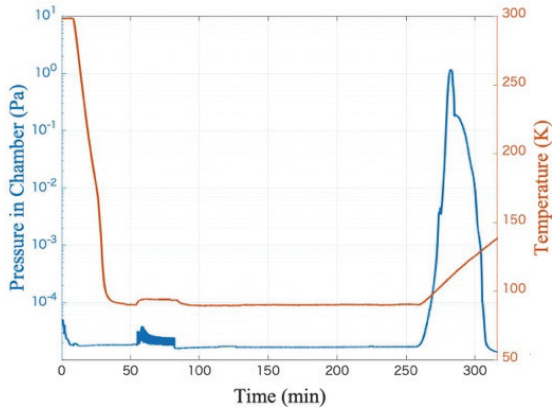

Fig. 4. Time evolutions of background pressure and surface temperature of the cryogenic cold head during a cryogenic target formation experiment.

3.2 Laser ablation from sublimated solid CO_2 layer

Figure 5 shows the plasma ion flux waveforms observed by the Faraday cup when the same position on the target was repeatedly irradiated with the laser. As shown in the figure, there is a big difference between the waveform obtained by the first laser shot and those obtained by succeeding laser shots. The first shot waveform has a larger and sharper peak than the

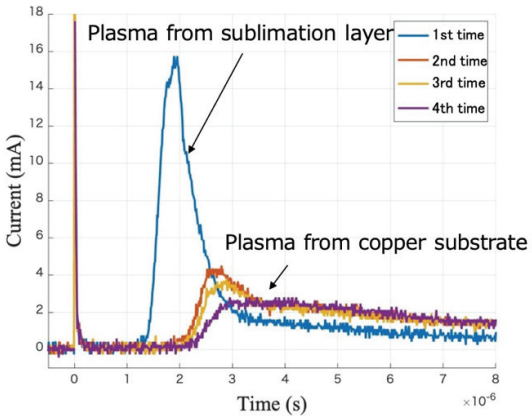

Fig. 5. Plasma ion flux waveforms obtained by repeatedly irradiating the same position of the cryogenic target with the laser.

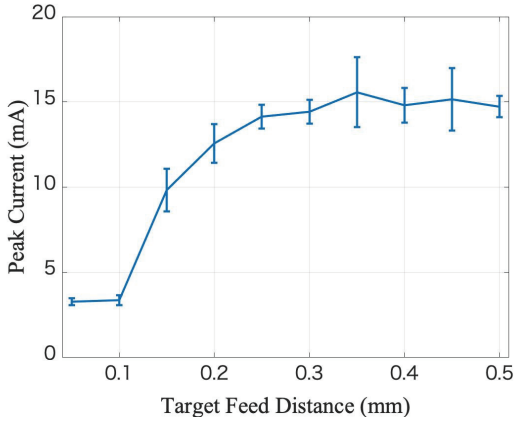

Fig. 6. Dependence of peak ion flux on target feed distance.

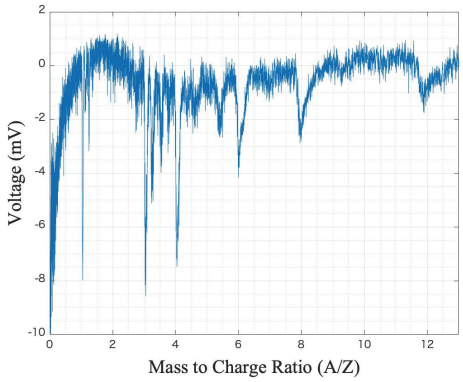

Fig. 7. A typical signal waveform from electrostatic energy analyzer.

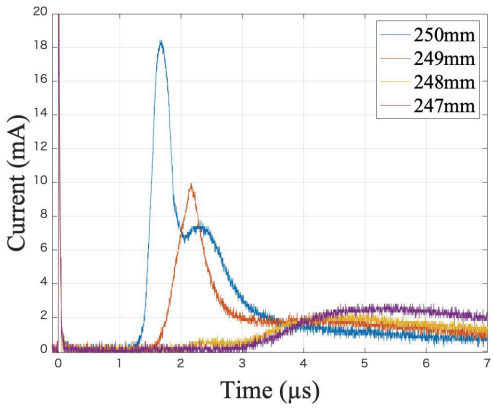

Fig. 8. Ion flux waveforms observed with various lens positions.

other waveforms. Also, the average kinetic energy of the ions that compose the first shot waveform seems to be considerably larger than the others. This result implies that the plasma ion flux produced by the first laser shot is mainly composed of light ions such as carbon and oxygen ions, while the plasma ion fluxes from subsequent laser shots are composed of heavy ions such as copper ions. Therefore, it is natural to assume that almost all of the sublimation layer in the laser spot was lost by the first laser shot. This means that the cryogenic target must be changed after each laser shot.

3.3 Relationship between target feed distance and ion current waveform

To investigate conditions for stable plasma generation from the cryogenic target, the peak value of plasma ion flux was measured by the Faraday cup as a function of the target feed distance. Here, the target feed distance is defined as the distance between the irradiation positions of two successive laser shots on the target. As shown in Fig. 6, the peak current increased with increasing feed distance and reached almost constant value with feed distances more than ~0.3 mm. When the feed distance was smaller than 0.2 mm, the laser ablation of the sublimation layer was significantly disturbed by the local destruction of the layer caused by the previous laser shot, leading to a large reduction in peak ion flux. On the other hand, when the target feed distance set to 0.3 mm or more, we could avoid the overlap of the laser spots on the target and achieve stable plasma generation from the sublimation layer.

3.4 Charge state analysis of laser-produced plasma ions

Figure 7 shows a typical signal waveform from the CEM detector in the electrostatic energy analyzer when the deflection voltage was 10 V. Note that the values on the horizontal axis in the figure were converted from time to mass-to-charge ratio of detected ions. This result confirms that C^{+}~C^{4+} ions were generated from the sublimated solid CO_2 layer.

3.5 Laser irradiation on a transparent target

The solid CO_2 layer formed on the cold head by sublimation was transparent to visible light. Because the frequency-doubled Nd:YAG laser (λ=532 nm) was used for laser ablation of the target, it is important to optimize incident laser optics so as to cause the laser ablation stably on the sublimation layer surface. Results of the ion flux measurement under various focal point positions are shown in Fig. 8. Changes in focal position over a distance of a few millimeters significantly changed the available plasma ion flux. This is probably due to the difference in whether the initial ablation occurs on the surface of the sublimation layer or at the interface between the sublimation layer and the copper base plate.

4. Conclusions

In this study, we developed a new laser ion source using a cryogenic target to meet the demand for long-time supply of high-stripped carbon ions at the heavy-

ion accelerator facility for cancer therapy. In the preliminary experiments, we succeeded in generating a CO_2 sublimation layer on a cold head cooled with liquid nitrogen. Although the sublimation layer on the cold head was locally lost by a single laser irradiation, it was found that the effect was limited to the laser spot area. By setting the target feed distance to the diameter of the laser spot or more, we demonstrated stable plasma generation from the CO_2 sublimation layer. We clarified that carbon ions with charge states of 1+ to 4+ were produced and supplied by the developed laser ion source.

References

[1] Y. Sioyama, M. Shinoto, A. Matsunobu and K. Matsumoto, “Heavy Ion Radiotherapy for Malignant Tumors: Current Status and Future Direction", *Fukuoka Medical Association*, **103**(4), 73–81 (2012).

[2] S. Yamada, T. Ono, K. Yusa and M. Tashiro, “Carbon Therapy Facility at Gunma University Heavy Ion Medical Center”, *journal of the Particle Accelerator Society of Japan*, **4**(3), 176–179 (2007).

[3] K. Takayama, T. Kawakubo, T. Adachi, T. Dixit, and A. Shaikh. “Energy-varying beam extraction assisted by large momentum deviation and charge exchange”, *Physical Review Accelerators and Beams*, **24**(1), 011601 (2021).

[4] N. Munemoto, K. Takayama, S. Takano, M. Okamura, and M. Kumaki. “Development of the C6+ laser ablation ion source for the KEK digital accelerator”, Review of Scientific Instruments, 85(2), 02B922 (2014).

[5] Y. Fuwa, S. Ikeda, M. Kumaki, N. Munemoto, D. Cinquegrani, M. Romanelli, T. Kanesue, M. Okamura, and Y. Iwashita, “Comparison of graphite materials for targets of laser ion source”, *Review of Scientific Instruments*, **85** (2), 02B924 (2014).

[6] J. Tamura, M. Okamura, T. Kanesue, and S. Kondrashev. “Ion generation from a solidified Ne target for a laser ion source”, *Applied Physics Letters*, **91**(4), 041504 (2007).

Study on laser ion source based on flowing liquid metal target using low melting point alloy

Kazumasa Takahashi, Toru Sasaki, Takashi Kikuchi

Nagaoka University of Technology, 1603-1 Kamitomioka, Nagaoka, Niigata, 940-2188, Japan

ABSTRACT

Laser ion sources have been used for providing high current ion beams extracted from plasmas generated by irradiating a laser. In order to avoid the change in ion beam current due to the target damage by laser irradiation, we have proposed a target whose laser irradiation surface is continuously renewed by using a circulating liquid. In this study, we investigated the characteristics of ions in laser ablation plasmas and the reproducibility of ion current for the development of a liquid target laser ion source using U-alloy, which is an alloy containing Bi with a low melting point. The result indicated that the ion current from the liquid target was similar with that based on a solid target and can provide high current ion beams. On the other hand, the result implied that it is necessary to suppress the fluctuation of the target surface to obtain the good reproducibility of current waveforms.

Keywords

Laser ion source, Laser ablation, Liquid metal, Heavy ion beam, Heavy ion inertial fusion, Massive ion inertial fusion

1. Introduction

A laser ion source is an ion source that extracts ion beams from plasma produced by laser irradiation on a target and has been expected to be an ion source that can produce high-current ion beams. In recent years, it has been researched to supply ions required for radiation biology applications [1], carbon beams for particle therapy [2-7], a lithium driver for an accelerator-driven neutron source using a lithium beam [8, 9], and a driver for heavy ion inertial fusion [10, 11].

When the laser ion source is used to produce low charge-state ions, the laser power density should be kept around the threshold of ablation plasma production. Such a situation, the low laser power density suppresses target damage and ensures reproducible plasma generation even if the same target surface is irradiated with a laser over a long term [1]. On the other hand, when a laser ion source produces multiply charged ions or a compound target containing multiple elements such as alloys, ceramics, or plastics is used, the amount of desired ion species is reduced compared to the case of a single element target. Therefore, it is necessary to increase the laser power density to achieve a high current ion beam. As the laser power density is the larger, the target damage by laser irradiation becomes larger. Therefore, the irradiated surface must be renewed after each laser irradiation. In such a use, the number of laser irradiations is limited to the target area, and the lifetime of the laser target becomes an issue for the operation of the laser ion source because frequent replacements of the target disturb the operation of accelerator.

In order to solve this problem, we have suggested a laser ion source using a circulating liquid target that can continuously renew the target surface. In this study, a U-alloy which is an alloy containing Bi with a low melting point was used as a laser target to supply Bi ions. High current Bi ion beams have been required for heavy ion inertial confinement fusion and supplying the ions from a liquid metal target could be useful for the purpose. We investigated the plasma ion current generated and the reproducibility of the obtained plasma.

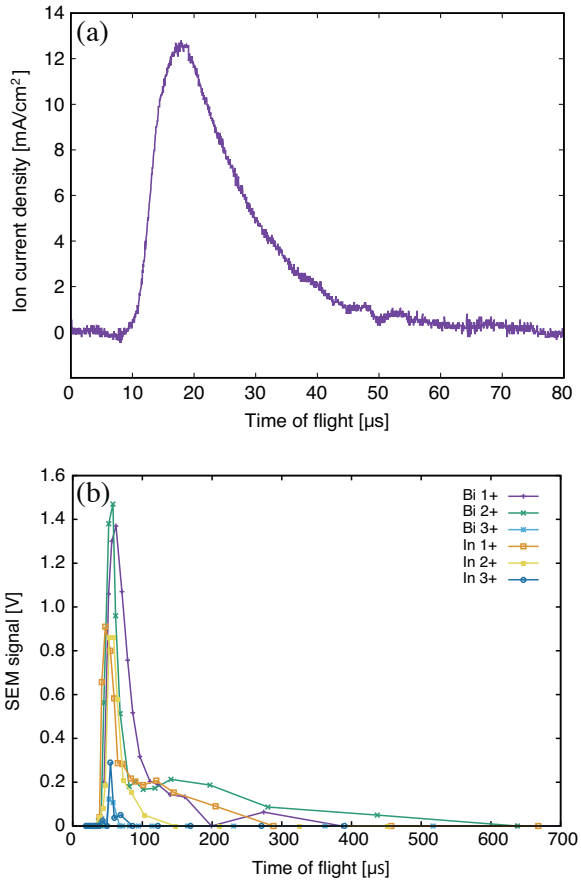

Figure 1: (a) Ion current waveform measured by a Faraday cup and (b) ion species and charge-state distribution of laser ablation plasma using a target of U-alloy 72.

2. Plasma diagnostics using solid target

To investigate the potential of supplying Bi ions from a U-alloy target, we measured the ion current and charge state distribution using a solid target. In this experiment, a laser target of U-alloy 72 whose melting point is 72 ℃ and which contains Bi (33wt%) and In (67wt%) was used. To generate plasmas, a Nd:YAG laser with a wavelength of 532 nm, a pulse width of 17 ns, and an energy of 0.3 J was used. The laser was focused to a spot of 3.1×10^{-2} cm^2 on the target using a lens with a focal length of 300 mm and irradiated at a laser power density of 5.7×10^8 W/cm^2.

Figure 1(a) shows the ion current in the plasma measured using a Faraday cup. The Faraday cup had an aperture of 2 mm in diameter and was located 150 mm from the laser target. The ion current was measured by applying a retarding voltage of -30 V. The result shows that the ion current density and the pulse duration were similar to them using a metal target made of a single element.

For the analysis of ion species and charge state distribution, an electrostatic ion analyzer (EIA) was used. Ions are detected using a secondary electron multiplier (SEM) placed at the end of EIA. The ion species and charge state distribution can be obtained by scanning the bias voltage applying to deflecting electrodes [12]. Figure 1(b) shows the obtained ion species and charge state distribution. The generated plasma consisted of In ions and Bi ions with up to triply charged ions for both ion species. As shown in the graph, ions of Bi^{1+} and Bi^{2+} were dominated in the ions. This result indicates the U-alloy has a potential to provide high current Bi ion beams as a target for laser ion sources.

3. Reproducibility of ion current

3. 1 Experimental setup

Figure 2 shows the experimental setup for measurement of ion current in laser ablation plasmas using a liquid target. The liquid metal target was circulated using a magnet pump (MP15RM, HAI YI

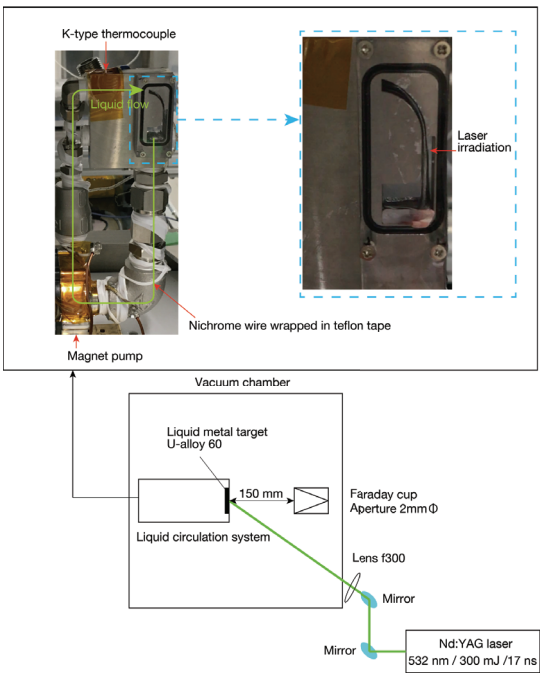

Figure 2: Schematic of experimental setup for ion current measurement of laser ablation plasma generated from a flowing liquid metal target.

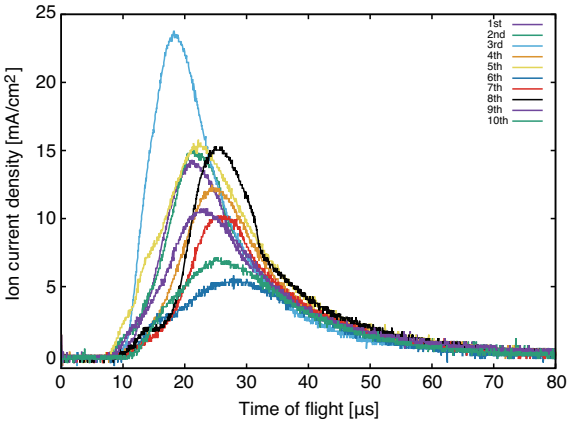

Figure 3: Ion current waveforms measured by a Faraday cup under the same experimental condition.

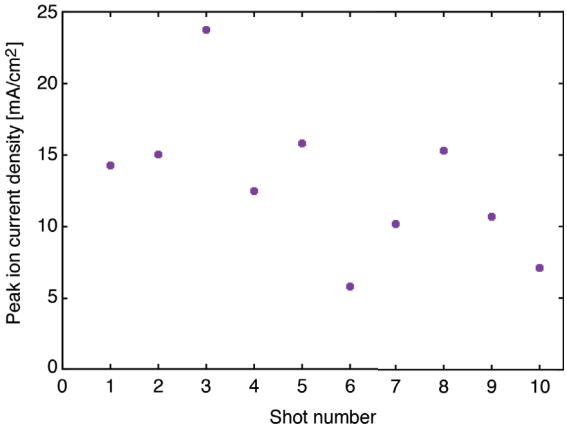

Figure 4: Variation of peak ion current for consecutive 10 laser shot.

PUMP &VALVE CO LTD.) in a vacuum. The liquid target was U-alloy 60, which is an alloy consisting of Bi (32.5wt%), In (51wt%) and Sn (16.5wt%) and whose melting point is 60 ℃.

The alloy was heated by a nichrome wire winding on the stainless-steel pipe used for the flow channel. The flowing target was designed to have a width of 15 mm and a thickness of 1 mm at the laser irradiation point. The liquid metal started to flow at temperature of 140 ℃ measured by a K-type thermocouple attached on the flow channel. Laser irradiation experiments were performed at this temperature.

In this experiment, the plasma generation was performed at a pressure of 1×10^{-2} Pa in a vacuum chamber. The laser energy, the power density on the target and the Faraday cup condition to measure the ion current were the same as them in the experiment for the investigation of ion species and charge state distribution using the solid target.

3.2 Reproducibility of ion current

Figure 3 shows the waveforms of the ion currents generated by laser irradiation of 10 shots. The obtained ion currents and pulse width of the plasmas are similar to those obtained using the solid U-alloy target. On the other hand, the reproducibility of the current waveform is poor as shown in this figure.

Figure 4 plots the peak of the ion current waveform obtained in Fig. 3 against the number of laser irradiations. The result shows that the peak of ion current varied randomly and was independent of the number of laser irradiations.

In this experiment, we did not measure the displacement of surface fluctuation. However, the displacement should be a few mm at a maximum based on the observation. The ion current of the generated plasma depends on the laser power density on the target. However, the variation of the laser spot size by the displacement of the surface is less than 1% and the effect of surface displacement would have little effect on the laser power density. Therefore, the variation of the ion current is considered to be mainly caused by the variation of plasma expansion direction due to the fluctuation of the liquid target surface. The result implies that the surface fluctuation of the liquid target should be reduced to obtain stable ion beams.

4. Conclusion

In order to avoid damaging the target due to laser irradiation, we have proposed a target whose laser irradiation surface is continuously renewed by using a circulating liquid. In this study, we investigated the characteristics of ion supply and the reproducibility of ion current for the development of a flowing liquid target laser ion source using U-alloy 60. As a result, it was indicated that the obtained ion currents and pulse width of the plasmas are similar to those obtained using the solid U-alloy target. On the other hand, the ion current waveform varied for shot by shot and the reproducibility is necessary to be improved by suppressing the fluctuation of the target surface.

References

[1] M. Okamura *et al.*, “Performance of the low charge state laser ion source in BNL”, in *Proc. 2nd North American Particle Accelerator Conference (NAPAC2016)*, Chicago, IL, USA, pp. 49-53 (2016).

[2] M. Okamura *et al.*, “Simulation of direct injection scheme for RFQ linac”, *Rev. Sci. Instrum.* **73**, pp. 761-763 (2002).

[3] T. Takeuchi *et al.*, “Acceleration of heavy ion beams by means of direct injection into RFQ Linac”, Rev. Sci. Instrum. 73, 2002, pp. 764-766.

[4] T. Takeuchi *et al.*, “Measurement of the laser plasma properties of the direct plasma injection method to the RFQ LINAC on the RIKEN laser ion source”, *Rev. Sci. Instrum.* **73**, pp. 767-769 (2002).

[5] H. Kashiwagi *et al.*, “Nd–YAG laser ion source for direct injection scheme”, *Rev. Sci. Instrum.* **87**, pp. 1569-1571 (2004).

[6] M. Okamura *et al.*, “Direct plasma injection scheme in accelerators (invited)”, *Rev. Sci. Instrum.* **79**, pp. 02B314-1-5 (2008).

[7] T. Sako *et al.*, “Development of C6+ laser ion source and RFQ linac for carbon ion radiotherapy”, *Rev. Sci. Instrum.* **87**, pp. 02C109-1-3 (2016).

[8] S. Ikeda *et al.*, “Neutron generator based on intense lithium beam driver”, *Rev. Sci. Instrum.* **91**, pp. 023304-1-5 (2020).

[9] A. Cannavò *et al.*, “Optimization of laser-target parameters for the production of stable lithium beam”, *Rev. Sci. Instrum.*, **91**, 033317-1-5 (2020).

[10] J. Hasegawa *et al.*, “Laser ablation ion source for heavy ion inertial fusion”, *Nucl. Instrum. Meth. Phys. Res. B,* **161-163**, pp. 1104-1107 (2000).

[11] M. Okamura *et al.*, “Laser ablation ion source for heavy ion inertial fusion”, *Nucl. Instrum. Meth. Phys. Res. A* **733**, pp. 97-102 (2014).

[12] K. Takahashi et al., “Resolution improvement of electrostatic ion analyzer using additional slit for laser ion source”, *J. Phys: Conf. Ser.*, **2244**, pp. 12089-1-5 (2022).

Generation of pulsed aluminum ion beam by bipolar pulse accelerator

Wataru Tagami, Akira Hujino, and Hiroaki Ito

Department of Electrical and Electronic Engineering, University of Toyama

ABSTRACT

Intense pulsed heavy ion beam is expected to be applied to materials processing including surface modification and ion implantation. For those applications, it is very important to generate high-purity ion beams with various ion species. We have developed a new type of pulsed ion beam accelerator named “bipolar pulse accelerator (BPA)” to improve the purity of the intense pulsed ion beam. The basic BPA system has two magnetically insulated acceleration gaps and is operated with a bipolar pulse. In this study, a vacuum arc discharge ion source, which can generate various metallic ions by selecting the electrode material, was installed in the bipolar pulse accelerator to generate high-purity pulsed metal ion beams. The pulsed ion beam was measured using a biased ion collector. It was confirmed from the evaluation of the ion beam energy by the time of flight delay time method that the aluminum ion beam was accelerated in two stages in the bipolar pulse accelerator.

Keywords

Pulsed ion beam, Bipolar pulse accelerator, vacuum arc ion source, pulsed power technology

1. Introduction

Silicon (Si) semiconductor products are close to the limit of material properties. Wide-gap semiconductors such as silicon carbide (SiC) are attracting attention as next-generation semiconductor materials instead of Si. The ion implantation method is used as a doping technique in the manufacturing process of wide-gap semiconductor devices. The conventional ion implantation method requires an annealing process. Wide-gap semiconductors, however, have problems such as extremely high annealing temperatures and redistribution of implanted ions. Therefore, the pulsed ion implantation method is expected to be applied as a doping technology for the next generation power semiconductors [1]. The pulsed ion implantation method is a doping technique that uses an intense pulsed heavy ion beam, which enables fast heating at about the pulse width and cooling effect by thermal diffusion so that ion implantation and annealing can be completed simultaneously.

A number of pulsed ion beam (PIB) sources have been developed so far for research and industrial application [2, 3]. The conventional PIB technology, however, is not suitable for the ion implantation due to the limitation of producible ion species and the low ion purity of PIB. It is important to generate high-purity ion beams with useful ion species for donor and acceptor in SiC such as nitrogen, phosphorous, boron and aluminum for the application of the pulsed ion implantation process. We have developed the high-purity pulsed nitrogen and aluminum ion beam sources with purity of more than 90 % and a new accelerator named “bipolar pulse accelerator (BPA)” that can further improve the ion purity by utilizing the difference in travel distance caused by different ion species [4, 5]. We have succeeded in generating the pulsed nitrogen ion beam for donor by installing a gas puff plasma gun as an ion source in the BPA [6, 7].

It is essential to develop a pulsed ion beam source for P-type dopant. In this study, we worked on a vacuum arc discharge metal ion source that can generate various metal ions by selecting metal electrodes. In addition, the vacuum arc discharge ion source was installed in the bipolar pulse accelerator for

generating the high-purity pulsed aluminum ion beam for acceptor in SiC. We report the experimental results about characteristics of the pulsed ion beam accelerated by BPA.

2. Principle of bipolar pulse accelerator

Figure 1shows a schematic of the BPA with the ion source developed in this study. The BPA system consists of a grounded ion source (anode), a drift tube, and a grounded cathode. In the system, a bipolar pulse with voltage of $\pm V_0$ and pulse duration of τ_p is applied to the drift tube. When ions generated in the grounded ion source reach the anode surface, the negative voltage pulse is applied to the drift tube and ions are accelerated toward the drift tube (①). If τ_p is adjusted to the time of flight delay of the ions to pass the drift tube, the pulse is reversed and the positive voltage is applied to the drift tube when top of the ion beam accelerated in the first gap reaches the 2nd gap. As a result, the ions are again accelerated in the 2nd gap toward the grounded cathode (②).

As an example, let us consider the principle of the improvement of the purity of the ion beam which contains the main component of aluminum ion (Al^+), which is acceptor in SiC, and impurity ion, hydrogen ion (H^+). Because of the difference in mass between aluminum and hydrogen ions, the beam length l_i of each beam accelerated with a pulse duration τ_p at a voltage V_0 is different. By matching the length (L) of the drift tube with the beam length of the target ion (Al^+), only Al^+ ion can be successfully accelerated in two stages, thus improving the ion beam purity. The beam length l_i of Al^+ ion accelerated by a pulse voltage of V_0= 200 kV with a pulse duration of τ_p= 70 ns is obtained to be 86 mm from the following equation:

$$\frac{1}{2} m_i {v_i}^2 = ZeV_0$$

$$l_i = \tau_p \cdot v_i$$

where m_i is the mass of the ion, e is elementary charge, Z is the charge state of the ion, and v_i is the ion velocity. In this study, the distance from the anode surface to the 2nd gap was set to 86 mm.

3. Experimental arrangement

3.1 Overview of vacuum arc discharge ion source

Figure 2 shows a schematic of the vacuum arc discharge ion source developed in this study. Vacuum arc discharge is generated by applying a pulse voltage between metal electrodes. The vacuum arc discharge can produce a variety of metal plasmas because the cathode material is evaporated and ionized [5, 8]. In this study, aluminum was selected as the electrode material to generate aluminum ions that can function as acceptor for next-generation power semiconductor materials. In the developed ion source, the ion current density injected into the acceleration gap can be controlled by changing the discharge position. The time delay between the vacuum arc discharge and the arrival of the ions at the acceleration gap need to be taken into account when operating as an ion source for BPA. In this study, a bipolar pulse voltage was applied 5 μs after the vacuum arc discharge ion source worked.

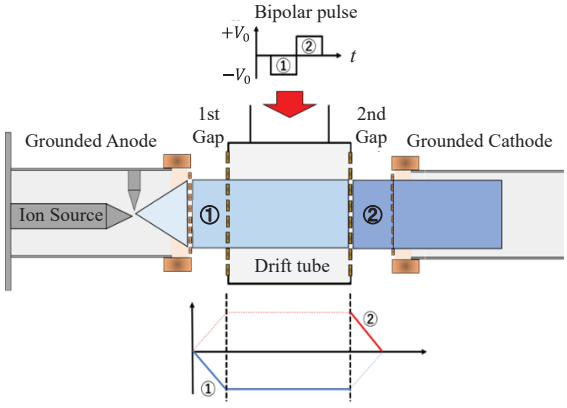

Fig.1 Acceleration principle of BPA

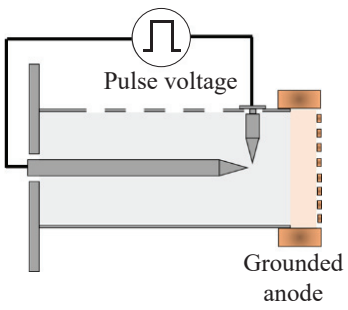

Fig. 2 Overview of vacuum arc discharge ion source

3.2 Overview of BPA system

Figure 3 shows a schematic diagram of the BPA system. The BPA consists of a Marx generator, a pulse forming line (PFL), a rail gap switch, a pulse transmission line (PTL), and an ion beam diode as a load. The designed output of the bipolar pulse generator is the negative and positive pulses of voltage ± 200 kV with pulse duration of 70 ns each. The PFL has a double coaxial structure consisting of a center conductor, a middle conductor, and an outer conductor, and pure water is used as the dielectric. The characteristic impedance of the line between the inner and intermediate conductors and one between the intermediate and outer conductors are 6.7 Ω and 7.6 Ω, respectively. The PFL is charged positively by the low inductance Marx generator with maximum output voltage of 300 kV through the intermediate conductor. The rail gap switch is filled with pure SF_6 gas and the pressure can be adjusted to control the optimum trigger timing.

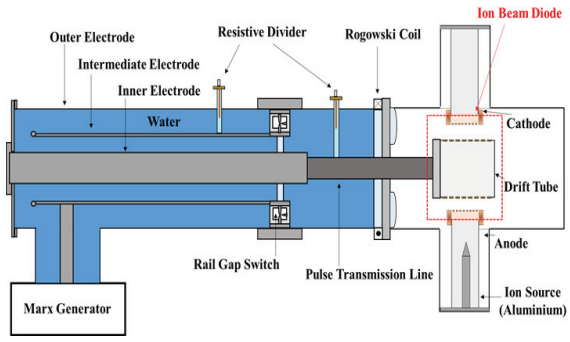

Fig.3 Schematic configuration of bipolar pulse accelerator

The BPA has two magnetically insulated acceleration gaps with gap length of $d_{AK} = 15$ mm each. In order to produce magnetic fields for suppression of the electron flow in both acceleration gaps, a magnetic field coil of grating structure is used and installed on the rectangular drift tube. The uniform magnetic field with strength of 0.3-0.4 T is produced in direction transverse to the acceleration gap by a capacitor bank with capacitance of 500 μF and charging voltage of 4 kV. Since at peak of the magnetic field, the bipolar pulse voltage is applied to the drift tube, the pulsed current produced by the capacitor bank is applied to the magnetic coil through an inductively isolated current feeder.

The charging voltage of the PFL (V_{PFL}) and the output voltage (V_0) of the bipolar pulse were measured by the resistive voltage divider placed near the rail-gap switch, respectively. The current through the ion beam diode was measured by a Rogowski coil. A bias ion collector (BIC) was placed inside the drift tube and the cathode to measure the ion current density of the pulsed ion beam.

4. Experimental Results

The output waveforms of the BPA with the developed ion source is shown in Fig. 4, where the Marx generator was operated at 75 % of the of the full charge condition. When the PFL was charged by the Marx generator and the rail gap switch is turned on ($V_{PFL} = 225$ kV), the bipolar pulse of voltage $V_o = -162$ kV, $+135$ kV and current $I_{out} = -12.4$ kA, $+11.7$ kA was observed.

The BIC was installed at 25 mm downstream from the anode surface inside the drift tube to measure the ion beam accelerated in the 1st gap by the first pulse of the bipolar pulse. Figure 5 shows the typical waveforms of the output voltage (V_0) of the bipolar pulse and the ion current density (J) of the pulsed ion beam accelerated in the 1st gap. As a result of the experiment, the ion beam with a peak current density of about 74 A/cm^2 was observed about 25 ns after the peak of the negative pulse voltage ($V_0 = -157$ kV). The energy of the pulsed ion beam can be estimated from a time of flight delay. Assuming that the observed ion is a singly ionized aluminum ion, the energy of the ion is calculated to be about 140 keV by the time-of-

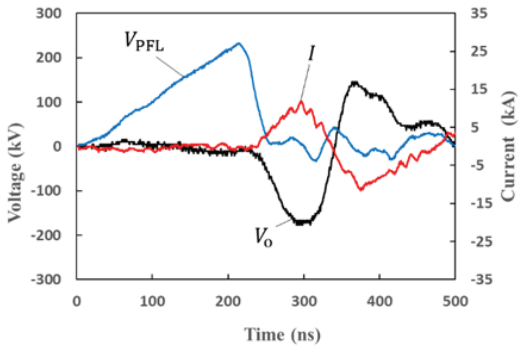

Fig.4 Typical output waveforms of BPA

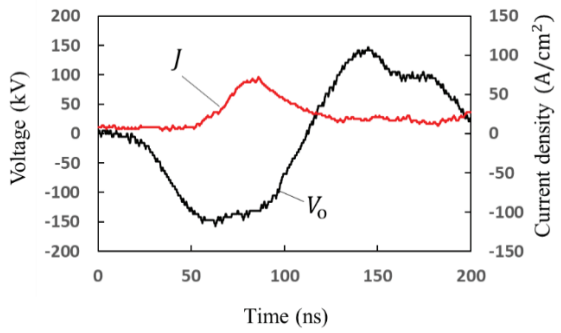

Fig. 5 Experimental result of ion beam accelerated in first gap

flight method. The estimated ion energy is in almost good agreement with the peak value of the negative voltage 157 kV, which suggests that the singly ionized aluminum ion was accelerated in the 1st gap.

Next, in order to confirm the acceleration of the pulsed ion beam in the 2nd gap, the energy of the pulsed ion beam was evaluated by a time of flight method (TOF). The BIC was placed in the cathode 15 mm away from the drift tube. Figure 6 shows the typical waveforms of the output voltage (V_0) of the bipolar pulse and the ion current density (J) of the pulsed ion beam accelerated in the 2nd gap. As shown in Fig. 6, the ion beam is observed about 11 ns after the peak of the positive pulse voltage ($V_0 = 142$ kV), and the peak ion current density was about 5 mA/cm^2. Assuming that the observed ion is a singly ionized aluminum ion, the energy calculated by the time-of-flight method is about 275 keV. This ion energy is close to the sum of the bipolar pulse voltages (-157 kV, $+142$ kV) that contributed to the two-step acceleration, suggesting that singly ionized aluminum

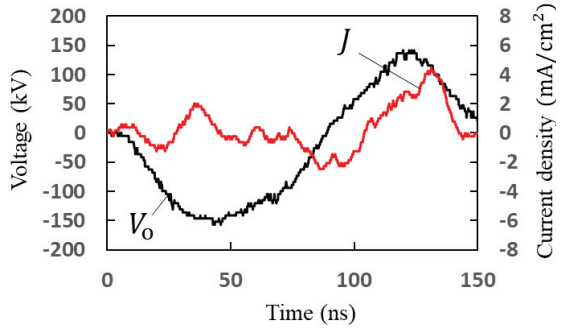

Fig. 6 Experimental result of ion beam accelerated in second gap

ions were accelerated in two-step. The ion current density after the second-stage acceleration was very small compared to one after the first-stage acceleration. This may be because the length of the drift tube does not match the beam length, since the applied acceleration voltage is lower than the designed value.

5. Summary

A vacuum arc discharge aluminum ion source has been developed to generate aluminum ions that can work as P-type dopants for next-generation power semiconductor materials. Experiments on two-stage acceleration of aluminum ions by a bipolar pulse accelerator were performed. The energy of the pulsed ion beam in the first-stage and two-stage acceleration can be estimated to 140 keV and 275 keV from a time of flight delay, respectively. We found from these results that the aluminum ion beam was successfully accelerated in the 1st and 2nd gaps by applying the bipolar pulse to the drift tube.

Acknowledgment

This work was supported by JSPS KAKENHI Grant Number JP19H02126.

References

[1] J. Khamsuwan, *et al*., "High-energy heavy ion beam annealing effect on ion beam synthesis of silicon carbide", Surface & Coatings Technology, Vol.206, pp.770-774 (2011).

[2] Y. Hashimoto et al., "Generation and focusing of intense ion beam with an inverse pinch ion diode", Jpn. J. Appl. Phys., Vol.31, pp.1922-1927 (1992).

[3] X. P. Zhu et al., "Characterization of a high-intensity bipolar-mode pulsed ion source for surface modification of materials", Rev. Sci. Instrum., Vol.73, pp.1728-1733 (2002).

[4] H. Ito et al., "Diagnosis of high-intensity pulsed heavy ion beam generated by a novel magnetically insulated diode with gas puff plasma gun", Rev. Sci. Instrum., Vol.79, 103502 (2008).

[5] H. Ito et al., "Characteristic observation of intense pulsed aluminum ion beam in magnetically insulated ion diode with vacuum arc ion source",

IEEE Trans. Plasma Sci., Vol.37, pp. 1879-1884 (2009).

[6] K. Masugata et al., "Development of bipolar-pulse accelerator for intense pulsed ion beam acceleration", Nucl. Instrum. & Methods in Phys. Res. A, Vol.535, pp.614-621 (2004).

[7] H. Ito et al., “Characteristics of Pulsed Heavy Ion Beam Generated in Bipolar Pulse Accelerator”, IEEJ Trans. on Fundamentals and Materials, Vol.135, pp.136–141 (2015).

[8] I. Brown, "Vacuum arc ion sources", Rev. Sci. Instrum., Vol.65, pp.3061-3081 (1994).

New area of target structure explored by the massive ion ICF

Kazuhiko Horioka

Tokyo Institute of Technology, Tokyo 152-8550, Japan

ABSTRACT

A new concept of massive multi-bunch ion accelerator enables us to explore a variety of target structures for inertial fusion. They are direct-drive, indirect-drive, fast-ignition, and indirect-driven fast-ignition schemes. Among them, fast-ignition schemes based on the massive ion beam driver are shown to be promising for robust, high gain and reproducible fuel target of inertial fusion energy (IFE).

Keywords

Heavy ion fusion, Inertial fusion energy, Massive ions, Fast ignition, Isentrope parameter, Fuel gain

1. Introduction

Recent experiments at National Ignition Facility (NIF) at Lawrence Livermore National Laboratory (LLNL) demonstrated a proof of existence of the ignition state in the laboratory by an implosion of spherical pellet in a high-Z radiation cavity (hohlraum) [1,2]. The stage of R&D on the inertial confinement fusion (ICF) seems to move to an exploration of practical scheme for a system of inertial fusion energy (IFE), together with investigation into a high gain, more robust and reproducible fuel-pellet implosion scheme.

Most inertial confinement fusion (ICF) approaches pursue laser driven central hot-spot ignition in which both compression of the fuel to almost 10^3 times of solid density and heating of the target center to the ignition temperature, must be accomplished simultaneously. In the final stage of compression, a localized area of high entropy stagnated region (hot-spot) must be surrounded by much lower entropy fuel. Namely, the high temperature central spark plug and the high density (much lower temperature) fuel must go together. However, the compression and the heating intimately coupled to each other through hydrodynamics and thermodynamics during the implosion. In addition, the spherical fast implosion suffers from various hydrodynamic instabilities which induce mixing and/or eddies in the sensitive region of the fuel core. As a result, the hydrodynamical instabilities degrade the conversion efficiency from kinetic energy to internal energy of the fuel at stagnation. Then the central spark ignition scheme strongly increases the requirement of high-precision symmetrical drive of the target.

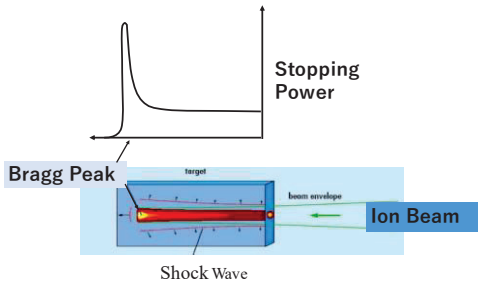

Fig.1 Schematic of energy deposition profiles of heavy ion beams.

An energy driver system based on an intense accelerator has been considered to be promising for a practical ICF reactor [3]. However, developing a massive, high average power, efficient, and low-cost heavy ion accelerator remains a critical issue for heavy ion inertial fusion (HIF).

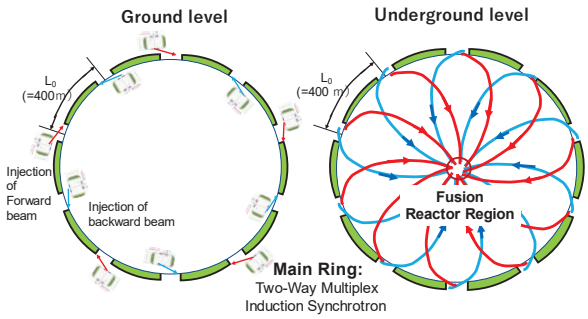

Fig.2 Schematic of main-ring of the massive ion beam driver [4].

The hydrodynamics and the fusion gain of ICF-target are sensitive functions of the irradiation scheme and energy deposition profiles of the driver. An illustration of the energy deposition profile of heavy ion beams (HIBs) is shown in Fig.1.

The laser-matter interaction is complex and not predictable. The energy deposition process of energetic ions is completely different from that of intense laser. That is, the laser light is basically cut off at the critical density and the energy deposition process at denser region depends on the plasma behavior. On the other hand, that of energetic particle beams can be almost explained by the Coulomb collision that enables us to control the deposition profile in a target. As shown in the figure, HIBs can penetrate into a dense region and deposit significant energy at the end of the range (at the Bragg peak). This is another advantageous point for the drive of ICF target and allows us to explore various target structures.

2. Massive Ion Beam Driver

An accelerator system using a repetitive induction modulator was proposed as a cost-effective and massive ion beam (MIB) driver in which a counter-facing, two-way multiple beams are accelerated in a stacking ring (Two way and multiplex scheme) [4].

An illustration of the two-way multiplex induction synchrotron is shown in Fig.2, which makes use of maximum magnetic-flux density and the induction fields.

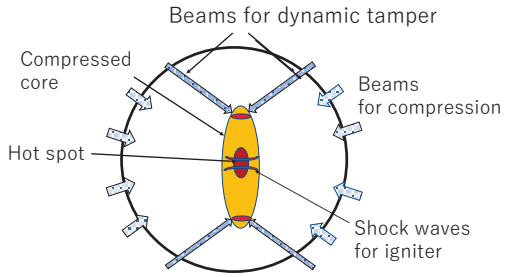

Fig.3 Direct-drive target for the massive ion driver.

The compact system expected to accelerate massive multiple ion bunches with tens of GeV and high (~ 30%) electrical efficiency via the two-way stacking ring composed of permanent magnets. The main ring has 10-fold symmetry and the fusion reactor will be placed in the center of the ring.

3. Possible Schemes for High Fusion Yield

One of the most important parameter characterizing the target compression is the *isentrope parameter* α

$$\alpha = p(\rho, T)/p_{deg}(\rho) \qquad (1)$$

where p_{deg} is the fuel pressure with Fermi-degenerated electrons [5]. Then α (= 1 ~ 4) indicates entropy of the fuel. Since high-gain ICF target requires highest compression for given pressure p, we have to keep α as small as possible.

The fuel gain G_f is a strong function of the isentrope parameter. That can be analytically derived, regardless of implosion schemes, as follows,

$$G_f \propto (\eta E_d)^{\beta} / \alpha^{\gamma} \qquad (2)$$

where E_d is the driver energy, η is the coupling (driver to fuel energy) efficiency. The exponents range β= 0.3 ~ 0.4 and γ = 0.9 ~ 1.2, depending on the implosion scheme. This indicates that keeping the entropy of the fuel as small as possible, is of primary importance for high yield of fusion energy.

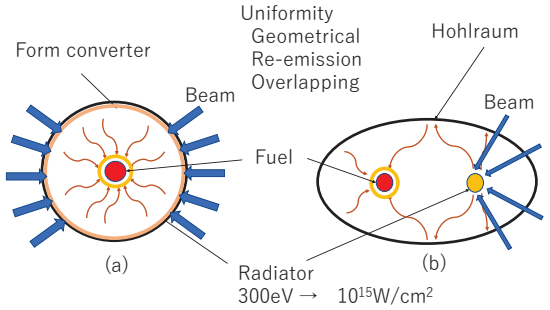

Fig.4 Illustrations of indirect-driven HIF targets. MIBs penetrate through the tamper (a) or hohlraum (b) and the multiple beams heat the form Xray-converter.

On the other hand, in case of the hot-spot ignition, the compression process should be somewhat dissipative to heat a part of the fuel core to the ignition temperature. The fast ignition scheme can avoid this incoherence. That is, as the ignition is driven by an independent external energy source, the compression phase can be carefully scheduled so as to suppress the entropy generation.

3.1 Advantages of massive ion driver

The merits of the MIBs for the driver include:

Reducing the space charge effect ;
Controlling the energy deposition profile;
Efficient and localized energy deposition;
and Cost-effective system.

Utilizing these advantages, we can extend the area of target structure for high-gain ICF.

3.2 Direct Irradiation Scheme

The MIBs enable us to directly drive the target with multiple beams. A schematic of the direct drive target is shown in Fig .3. Incase of the MIB driver, a quasi-spherical (barrel shaped) target is planned to use. The upper and the lower regions are irradiated to make hydrodynamical tamper. They are expected also to work as a shock wave igniter in the compressed fuel.

3.3 Indirect drive

The radiation symmetrization is a critical issue in the achievement of highly uniform implosion.

A schematic of the indirect MIB-drive fuel pellet is shown in Fig.4 (a) and (b). The indirect drive target relies on smoothing by radiation energy transport in the fuel pellet (a) [6], and in a casing enclosing the fuel pellet (b). As illustrated in the figure, MIBs penetrate into the X-ray converter inside the pellet or radiation cavity (hohlraum) in which a form is filled as a X-ray radiation converter [7]. The outer high-Z layer of Fig.4 (a) has tamping effect which increases the hydrodynamic efficiency.

3.4 Fast Ignition Scheme

The concept of fast ignition (FI) is to separate the fuel compression process from heating of the central spot. That is, in the FI scheme, the compression can be carefully scheduled to keep the entropy production as small as possible. A tandem acceleration of the target is planned to use to increase the implosion velocity with minimum entropy generation [8]. After the near isentropic compression, the core is ignited by an external energy driver that makes the target hydrodynamically less sensitive to asymmetries. The FI approach has flexibility of target design which relaxes symmetry requirement and allows non-spherical drive.

The delivery of ignition trigger and efficient coupling of an ultra-intense beam pulse are the prise to be paid for FI. Although Petta-watt (PW) laser has been the primarily candidate of the external ignition driver, the core of fuel has a high density in the order of $n / n_c \sim 10^5$. Then the feasibility of external trigger by Peta-watt (PW) laser largely depends on the energy

transport from the laser absorption layer (n_c) to the compressed dense fuel core. However that is not established yet.

Recently a new concept using bunch rotation in a large amplitude detuned RF cavity was proposed as a method to make ultra-short heavy-ion-beam pulse in which a number of bunch trains are stacked by the detuned RF cavities [8]. That extends the area of target structure of HIF from conventional indirect drive and hot-spot ignition to the FI scheme.

3.5 New Area of Target Design

Energetic ion beams can deposit their energy in an internal structure through an outer component such as high-Z radiation cavity and tamper of fuel pellet. In addition, HIB can deposit its energy in a localized dense region and the deposition profile is well-defined.

Utilizing these features, the MIB driver can extend the area of target structure. All of the proposals shown in Fig.3-5 are new structures of HIF target extended by the MIB driver.

4. Concluding Remarks

Massive ion beams extend the exploration area of the target structure of ICF. Among the various approaches, FI seems to be the most attractive scheme to realize robust and reproducible high fusion yield.

The guideline to get high fusion yield is quite simple in case of the external trigger of ignition; nearly isentropic compression and highly localized heating. That is the highway to get high fuel gain.

As the fuel gain is basically a strong function of *isentrope parameter* and fuel energy (ηE_d), fast ignition scheme driven by the massive ion beam should be advantageous to drive high fuel gain target.

The electrical conversion (electricity to the beam energy) efficiency of the massive ion accelerator is estimated to be ~ 30% [8]. The high gain target and the efficient accelerator are expected to relieve greatly the criteria of fusion power system.

In addition to the advantages of HIBs (capability of repetitive operation, high efficiency and reliability), the massive multiple-beam driver facilitates us to design a practical power plant.

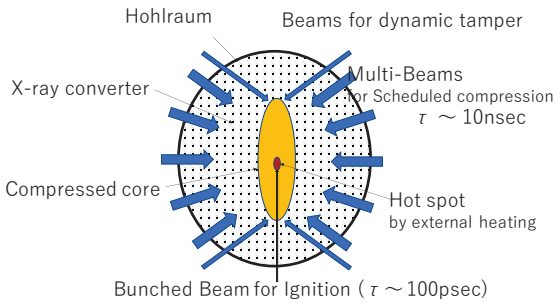

Fig.5 An example of in-direct drive fast ignition target.

References

[1] A.B.Zylstra et.al., "Record Energetics for an Inertial Fusion Implosion at NIF", *Phys. Rev. Lett.,* **126**, 025001 (2021).

[2] A.B.Zylstra, O.A.Hurricane et.al., "Burning plasma achieved in inertial fusion", *Nature*, **601**, 27 Jan. (2022).

[3] K.Horioka, " Progress in Particle-Beam-Driven Inertial Fusion Research: Activities in Japan " *Matter and Radiation Extremes*, **3**, 12 (2018).

[4] K.Takayama et. al., "A massive-ion beam driver for high-energy-density and future inertial fusion", *Phys. Lett.*, **A 384**, 126692 (2020).

[5] S.Atzeni and J.Meyer-ter-vhen, "The Physics of Inertial Fusion", *Oxford Univ. Pres*., (2004).

[6] S.Kawata, "Direct-drive heavy ion beam inertial confinement fusion: a review, toward our future energy source", *Adv. Phys*., **6**, 1, 1873860 (2021).

[7] M.Murakami, "Target Physics of Heavy Ion Inertial Confinement Fusion", *J. Plasma &,Fusion Res.*, **77**, 40 (2001).

[8] K.Takayama, private communication.

3D Coupled Envelope Approach for a High Intensity Linac and its Comparison with 3D Gaussian Macroparticle Simulation and PIC code (TraceWin)

Ebisawa Takashi, Takayama Ken*

National institutes for Quantum Science and Technology
** High Energy Accelerator Research Organization, Accelerator Laboratory (KEK)*

ABSTRACT

Presented here is a theory model of a beam-envelope approach to determine the global behavior of a charged particle beam propagating through a high intensity linac with a solenoid channel. The model is applied to the Gaussian particle distribution, where the motion of an individual particle is governed by linear focusing and defocusing forces in the solenoid channel and RF fields, except for space-charge forces. In this model, nonlinear effects disappear by averaging over the harmonic motions such as the betatron motion and phase motion in the moving direction and the Gaussian distribution. All particles making up a 3D Gaussian bunch obey the same linear equations of motion where all information of nonlinearity in the space-charge forces and the particle distribution are carried in. The theory is validated by Gaussian macro-particle simulation(GMPS) and PIC codes, TraceWin. As an example, the model is applied to the case of an IFMIF Superconducting RF (SRF) linac with solenoid guiding and half wave resonator (HWR) acceleration. The results are compared with results obtained by this model and other two approaches.

Keywords

Superconducting Radio Frequency accelerator, Space charge effects, Gaussian distribution, Envelope approach

1. Introduction

In high current beam accelerators, motions of charged-particles are well known to be largely affected by space charge effects. An approach of the macroparticle simulation, where space charge effects are properly taken into account, has been traditionally employed in order to understand beam dynamics there. It takes a long computational time in general, since a number of 1 M macropartcles has to be treated in case that sufficient enough accuracy is expected. In most of cases we don't need information of individual macroparticle's motion but want to know the macroscopic evolution of beam along an accelerator of concern. For this purpose, the beam envelope approach is desire. Applications of the envelope approach have been limited to a linear beam focusing system. Unfortunately, the space-charge forces are nonlinear in the excursion (*x,y,z*) from the position of the on-momentum particle in the physical space. Reasonable linearization of the nonlinear space-charge forces is required from this reason. Recently, a necessary linearization has been tried in Ref [1] with some success. In this paper, its essence is described and notable outcomes are introduced below.

A noble concept of the renormalized restoring force coefficient in the betatron equation or the linearized equation of phase motion, which is originated from the space-charge forces, is introduced, as shown below.

$$x''(s)+\left[K(s)+K_{sp}(x)\right]\cdot x(s)=0 \qquad (1\text{-}1)$$

where the renormalized restoring force coefficient $K_{sp}(x)$ is simply proportional to the gradient of space-charge force. This renormalized restoring force coefficient is a function of the individual particle's position *x*, *y*, and *z*, and depends on the particle distribution. Fast oscillations in the betatron motion and linearized phase motion allow averaging of $K_{sp}(x)$ over the bounded motion such as the unperturbed betatron oscillation or the small amplitude phase oscillation, resulting in

$$\bar{K}_{sp}=\frac{1}{x_{max}}\cdot\int_0^{x_{\max}}K_{sp}(x)\cdot dx \qquad (1\text{-}2)$$

where x_{max} is the wavelength of the bounded motion. Consequently, *x*, *y*, and *z* dependence of the averaged renormalized restoring force coefficient disappears, leaving their oscillation amplitude information alone, which is nothing but emittance information of an individual particle. When this averaged renormalized restoring force coefficient is further averaged among the particle distribution $g(\varepsilon)$ in the emittance space, as shown below

$$\langle\bar{K}_{sp}\rangle=\int_0^{\infty}\bar{K}_{sp}\cdot g(\varepsilon)d\varepsilon \qquad (1\text{-}3)$$

$\langle\bar{K}_{sp}\rangle$ may be regarded as the defocusing *k*-value due to the space-charge forces, where the property of nonlinearity in Eq. (1-1) completely disappears.

The particle distribution is assumed to be a Gaussian. Space-charge fields for the Gaussian distribution is given in the integral form using a single parameter [2]. As a result, we acquire a method to treat the nonlinear system in a

context of linear theory.

In the solenoid-magnet guiding system in which solenoid magnets are placed periodically along the beam orbit *s*, the motion of charged particles is necessarily coupled in the horizontal and vertical directions in the real space. This coupling can be separated by introducing a rotating coordinate system. In the rotating coordinate system, which is referred to herein as the rotating coordinate system, the equation of motion has the form of an isolated betatron equation, where the restoring coefficient is a function of *s*. It is known that the RF fields affect fractionally on the horizontal motion, because the longitudinal RF accelerating fields E_z are always associated with the E_r and B_θ fields that are proportional to the excursion from the center *r* within the range of the first-order approximation. These terms take simply a role of discrete focusing or defocusing. Meanwhile, the small amplitude phase motion is mainly dominated by the longitudinal RF fields. Thus, it is concluded that the envelope approach holds in the rotating coordinate and the beam-envelope concept makes sense. The beam envelopes in the transverse direction are converted to that in *x–y* Cartesian coordinates at the last stage. IFMIF/EVEDA LIPAc superconducting RF (SRF) linac using half wave resonator cavities [3], where a 125 mA D+ beam is accelerated from 5 MeV to 9 MeV with focusing by superconducting solenoids is chosen as an example of its application.

2. 3D Envelope approach

We introduce the concept of the betatron equation in rotating system and averaged renormalized restoring force coefficients over the bounded motion and Gaussian distribution. We realize that accompanied with the 3D envelope equations [1]

$$\begin{cases} \rho_{nR}''(s)+\left\{\dfrac{\Omega^2(s)}{4}+\Pi_T(s)-\dfrac{\lambda'(s)}{2}-\dfrac{\lambda^2(s)}{4}-\left\langle \bar{K}_R(s)\right\rangle\right\}\cdot\rho_{nR}(s)=\dfrac{1}{\rho_{nR}^3(s)} \\ \rho_{nl}''(s)+\left\{\dfrac{\Omega^2(s)}{4}+\Pi_T(s)-\dfrac{\lambda'(s)}{2}-\dfrac{\lambda^2(s)}{4}-\left\langle \bar{K}_l(s)\right\rangle\right\}\cdot\rho_{nl}(s)=\dfrac{1}{\rho_{nl}^3(s)} \\ \rho_{nz}''(s)+\left\{\Pi_L(s)-\dfrac{\lambda'(s)}{2}-\dfrac{\lambda^2(s)}{4}-\left\langle \bar{K}_z(s)\right\rangle\right\}\cdot\rho_{nz}(s)=\dfrac{1}{\rho_{nz}^3(s)} \end{cases} \tag{2-1}$$

where $\Omega(s)=\left(\frac{Q}{A}\right)\cdot\left(\frac{e}{mc^2}\right)\cdot\frac{c}{\beta(s)\gamma(s)}\cdot B_z(s)$ is a coefficient of the solenoid focusing force for an ion (mass number *A* and charge state *Q*) with relativistic factors β and γ, $B_z(s)$ is a solenoid fiel,

$$\Pi_L(s)\equiv\frac{1}{2}\cdot\left(\frac{Q}{A}\right)\cdot\left(\frac{e\hat{E}}{mc^3}\right)\cdot\frac{\omega_{rf}}{\beta_s^3\gamma_s^3}\cdot f(s)\cdot cos\left[\frac{\omega_{rf}}{c}\cdot\int^s\frac{ds'}{\beta_s(s')}+\delta_s\right]$$

and

$$\Pi_T(s)\equiv\frac{1}{2}\cdot\left(\frac{Q}{A}\right)\cdot\left(\frac{e\hat{E}}{mc^2}\right)\cdot\frac{1}{\beta_s^2\gamma_s}\cdot\left[f'(s)\cdot cos\,\phi(s)+\frac{\beta_s\cdot\omega_{rf}}{c}\cdot f(s)\cdot sin\,\phi(s)\right]$$

with $\phi(s)\equiv\frac{\omega_{rf}}{c}\cdot\int_{s_{in}}^s\frac{ds'}{\beta_s(s')}+\delta_s$ are coefficients of focusing and defocusing term of accelerating filed, $\hat{E}$ is an accelerating field amplitude, *f*(s) is a field profile for beam axis, ω_{rf} is an angular frequency, $\lambda=\frac{p'(s)}{p(s)}$ is a coefficient of friction force by accelerating field. This coefficient was converted variable to remove friction term for deriving envelope equation. The detail definition or deduction of these equations are described in ref [1].

It is easy to solve Eq. (2-1) with a help of commonplace PC. The initial conditions for Eq. (2-1) are determined from the Twiss parameters at the exit of the upper beam channel. Using the solutions of (2-1), the solution of betatron equation is written as

$$\chi_{nR}(s)=\rho_{nR}(s)\cdot\sqrt{\varepsilon_{nR}}\cdot\cos\left[\phi_{nR}(s)+\delta_{nR}\right] \tag{2-2}$$

$\phi_{nR}(s)=\int_0^s\frac{ds'}{\rho_{nR}^2(s')}$ is the betatron phase advances, ε_R and δ_R are the emittance and initial betatron phase of an individual particle. The oscillation amplitude is proportional to the envelope function that does not require information about individual particles. The root-mean-square (rms) beam size is obtained from the normal definition,

$$\sigma_R(s)=\sqrt{\frac{p(0)}{p(s)}}\cdot\sqrt{\left\langle\chi_{nR}^2(s)\right\rangle} \tag{2-3}$$

where,

$$\left\langle\chi_{nR}^2(s)\right\rangle=\frac{\rho_{nR}^2(s)}{2}\cdot\left\{A_{nR}+\cos\left[2\phi_{nR}(s)\right]\cdot B_{nR}-\sin\left[2\phi_{nR}(s)\right]\cdot C_{nR}\right\}$$

$$A_{nR}\equiv\left\langle\varepsilon_R\right\rangle=\frac{\sum_{i=1}^N(\varepsilon_i)_R}{N},$$

$$B_{nR}\equiv\left\langle\varepsilon_R\cdot\cos(2\cdot\delta_R)\right\rangle=\frac{\sum_{i=1}^N(\varepsilon_i)_R\cdot\left[2\cdot\cos^2(\delta_i)_R-1\right]}{N}$$

$$C_{nR}\equiv\left\langle\varepsilon_R\cdot\sin(2\cdot\delta_R)\right\rangle=\frac{2\cdot\sum_{i=1}^N(\varepsilon_i)_R\cdot\sin(\delta_i)_R\cdot\cos(\delta_i)_R}{N} \tag{2-4}$$

It is noted that the coefficients B and C in Eq. (2-4) are zero in the Kapchinskij–Vladimirskij (K–V) distribution.

3. Verification of the envelope approach

To verify the present model, in this section we compare its predictions of RMS beam size with results by Gaussian macroparticle simulation (GMPS) and TraceWin with 10^5 test particles. For this purpose, we have chosen the IFMIF/EVEDA-LIPAc SRF linac as shown in Fig 1 [3]. The assumed machine parameters have been optimized for minimizing the halo beam by using the TraceWin simulations, where the beam current of 125 mA is always assumed [4]. Their comparisons are given in Fig 2.

We verified the case, where are the beam current of 0, 40, 80 125 mA. One can find that three approaches have similar structural features for the entire beam current. The

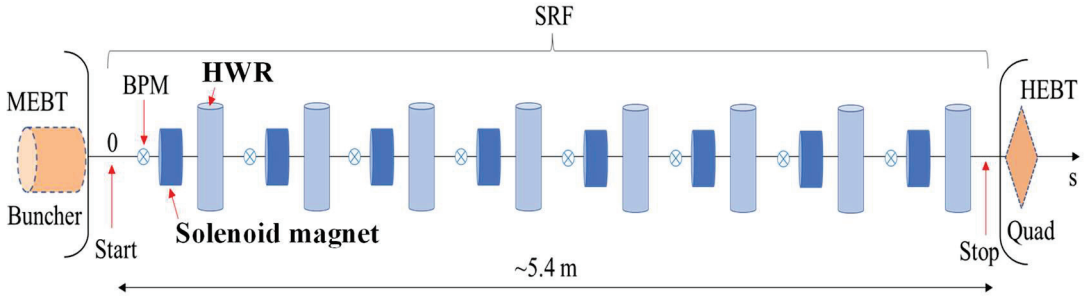

Figure 1: Schematic view of the LIPAc SRF.

agreement among three cases seems to be sufficient enough.

Because solenoid magnetic field values were optimized about 3.5 T to 4.0 T for the beam current of 125 mA, the fluctuation of the beam size is large in case of lower than 40 mA. This behavior is due to the mismatching optics of strong focusing for the low beam current.

It is concluded that the envelope approach is useful for assessing the macroscopic behavior of the beam in the range of 125 mA or lower case.

4. Future plan

As a tool to assess the orbital evolution of any actual beam size under strong space-charge fields, the present envelope approach has been proposed. Its accuracy and calculation time are crucial issues for its real-time use when designing a machine or commissioning. The typical time period for its calculation is around several seconds, which is extremely faster than that of TraceWin of order of several hours.

There are two typical examples where the present envelope approach is useful. One is designing a beam transport line and linac for a space-charge-dominated beam, whatever guiding is quadrupole focusing and solenoid guiding. The other example is providing an efficient tool for studying beam halo formation enhanced by high-intensity beam core breathing through a long beam line including focusing and acceleration devices. As long as the assumption of Gaussian distribution stands, the beam-envelope approach gives the beam core evolution along the orbit coordinate in a self-consistent manner, and consequently the orbit-varying nonlinear forces acting on the halo particles are evaluated immediately in the same matter as that of the GMPS. Thus, it is straightforward and relatively quick to know how the halo particles behave through the beam line.

5. Summary

For the first time, a practical beam-envelope approach for an asymmetric beam in the solenoid guiding channel has been developed. The noble concept of the renormalized restoring force coefficient was introduced. Averaging of this renormalized restoring force coefficient over the bounded motions of an individual particle and over the Gaussian distribution allowed us to treat the space-charge dominated system in the linear theory, where all particles making up a 3D Gaussian bunch obey the same linear equations of motion. This approach has been shown to be exact for the case of the Gaussian distribution that is most likely to be found in most of actual beams.

References

[1] T. Ebisawa and K. Takayama, “3D beam-envelope approach for an asymmetric beam in a high intensity linac with a solenoid channel”, submitted to Phys. Rev. A&B in May (2022).

[2] K.Takayama, “A new method for the potential of a 3-dimensional nonuniform charge distribution”, Lett. Nuovo Cimento **34** 190 (1982).

[3] H. Dzitko *et al.*, “Technical and logistical challenges for IFMIF-LIPAc cryomodule construction ”, Proceedings of SRF2015, Whistler, BC, Canada, paper FRBA01 (2015).

[4] N. Chauvin *et al.*, “Optimization Results of Beam Dynamics Simulations for the Superconducting HWR IFMIF linac”, Proceedings of PAC 2009, Vancouver, Canada, paper TH5PFP005 (2009).

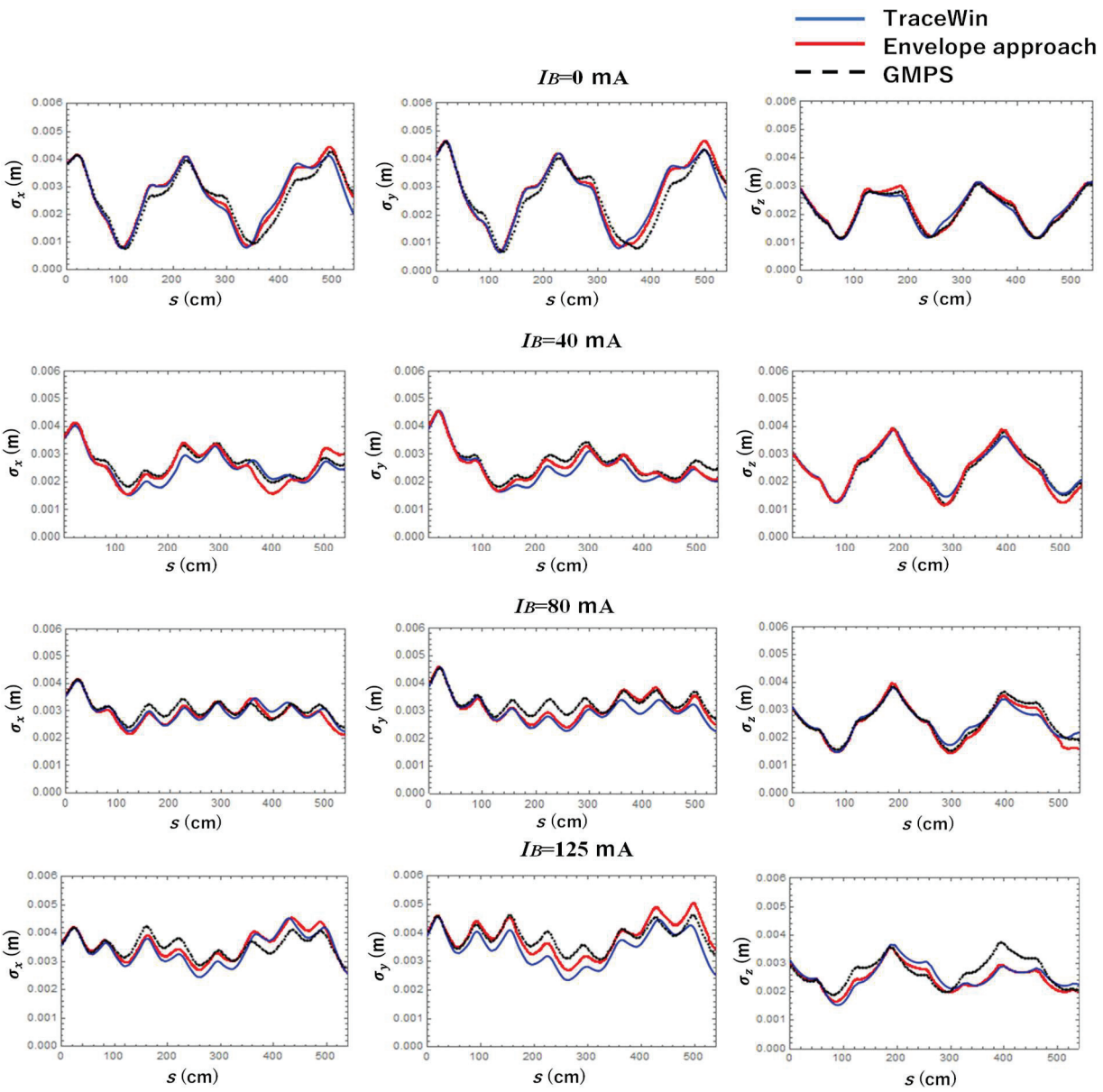

Figure 2: Orbital evolution of the RMS beam sizes.

Design of the Irradiation Line and Beam Physics Issue at the Final Stage of the Massive Ion ICF Driver

K. Takayama

High Energy Accelerator Research Organization, Accelerator Laboratory,

*Tsukuba, Ibaraki 305-0801, Japa*n

ABSTRACT

Further studies of the recently proposed massive ion inertial fusion scheme [1] are described. Especially splitting of the extracted bunches and their path adjusting scenario are discussed. The necessity of beam dumps placed nearby the fusion reactor is discussed and their possible scheme is given. Space-charge effects at the final stage, where 100 driver bunches ballistically hit the fusion target sphere, are estimated.

Key Words: massive ion, inertial fusion, fusion target, beam dump, fusion reactor, space-charge effects

1. Introduction

The massive ion ICF scenario [1] is being extensively studied from various aspects in the research forum in Japan now [2]. It is essential for 100 missive ion bunches to irradiate isotopically a fusion target of 1 cm in diameter in synchronization. 5 bunches simultaneously extracted from the same extraction region of the main driver ring are delivered to the target with different elevation angles. This occurs in the same way in the equally separated high energy beam transport (HEBT) lines with $\pi/10$ in the azimuthal direction. 5 bunches placing vertically are separated by gradient magnet fields in the middle of the extraction region and a fusion reactor as seen in Fig. 1 and run up a guiding slope until a necessary height to have the required elevation angle of $|\pi/6|$ and $|\pi/3|$. Path length from the bunch split magnet to the target must explicitly match for 5 bunches. It will be discussed here how this path adjusting can realized.

We have to note that there is the operation mode called beam commissioning before the actual fusion operation, where 100 bunches never hit the target. In addition, miss-shot can happen in the normal fusion run. A driving ion bunch with beam power of 400 kJ will directly hit the first reactor wall of liq. LiPb with its small beam size of 5 cm in diameter. Predicted significant local ablation from the wall surface is not afforded from a reactor evacuation point of view. This situation must be considered when designing the HEBT. The HEBT further passing beyond the reactor region will be described here.

So far the necessity of charge neutralization at the last stage of HEBT from the final focusing region to the target has been extensively discussed at many occasions. For the first time it will be theoretically shown that the charge neutralization is unnecessary, provided the present massive ion ICF driver parameters [1]. The prediction is proved by inversely solving the beam envelope equation perturbed with strong space-charge forces from the target to the final focusing quadrupole magnet. In addition, it is discussed that a tremendous amount of charge brought into the target sphere by 100 projectile bunches induces deceleration of the projectile ion bunches, which depends on the position of bunch.

2. Bunch split and Path adjuster

5 bunches extracted from the driver ring are split by the gradient magnet, as shown in Fig. 1 and then they propagate through their independent inclined beam

lines until their beam level achieves the necessary value to generate the elevation angles of |π/6| and |π/3| to the target. Its schematic view is given in Fig. 1. It is obvious that the path length depends on the elevation angle. In order to adjust the path length, a kind of

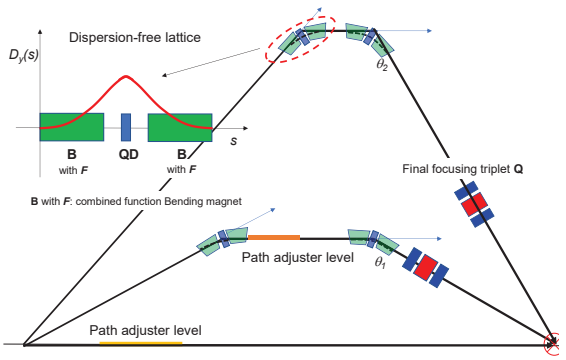

Figure 1: Layout of final stage of the HEBT beyond the bunch splitter, where lower beam lines are ignored. The dispersion-free lattice is used for the

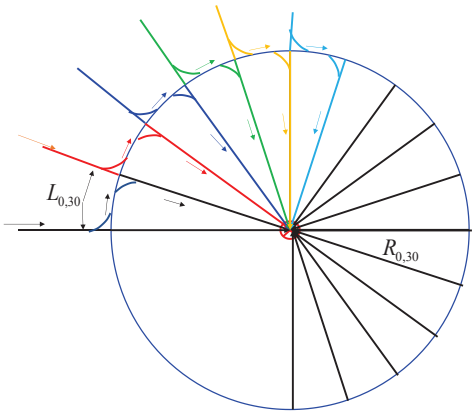

Figure 2: Schematic view of the path adjuster, where $L_{0,30}$ and $R_{0,30}$ are the adjusted distances and adjuster ring radius for 0 degree and 30 degrees bunch, respectively.

circular-shape beam lines are introduced. They will be placed at the flat levels for bunches of 0-radian and |π/6| radian, respectively, as shown in Fig. 2.

3. Miss-shot and beam dump

As pointed out in Introduction, at the beam commissioning stage that shall continue more than 1 year after everything in the accelerator complex becomes ready, 100 bunches must be guided into the target position without the fusion fuel target. The bunches never stop there and propagate toward the first liquid metal wall. Fortunately, the bunch can pass through the beam chamber placed in the opposite position, because each of 100 bunches has its pair and a pair shares the beam line in the reactor chamber. The bunch passing through the opposite beam chamber arrives at the final focusing region and is oppositely focused and defocused, resulting in extra expanding in the transverse plane, and reaches the bending region. There, the bunch is deflected in the opposite direction. If a beam dump is placed immediately after the bending region, the beam power of 400 kJ can be

Figure 3: Schematic view of beam line beyond the fuel target.

deposited in this beam dump with powerful cooling. Fig. 3 shows schematically the beam line beyond the target position.

In addition, this system works when miss shot occurs without the fusion target. We can find a fail-safe solution of the proposed massive ion ICF.

4. Space-charge effects at the last stage

4.1 Self-charge effects

Space-charge effects in the focused beam nearby the target has been long of our big concern. Beam size of each bunch on the target must be fixed from requirements of target physics. It is assumed to be rms value of 1 mm here. We have to know how the beam size evolves in the ballistically moving region assuming the present beam parameters. For this purpose, the space-charge perturbed beam envelope equations are solved upstream from the target position.

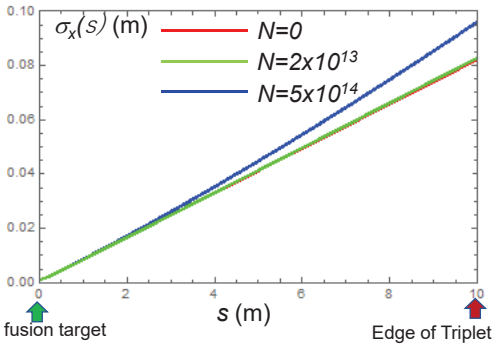

Figure 3.1: σ_x vs. s

The 3D coupled envelope approach for a Gaussian beam [3] that has been developed for beam dynamics in the IFMIF high intensity driver has been employed. Beam size evolution in the reactor region is shown for different particle numbers/per bunch.

The currently assumed number of ions per bunch is $N=2x10^{13}$. We will not find notable space-charge effects if the beam sizes are spread up to the sufficient level at the final focusing region. The last is an issue of optics matching.

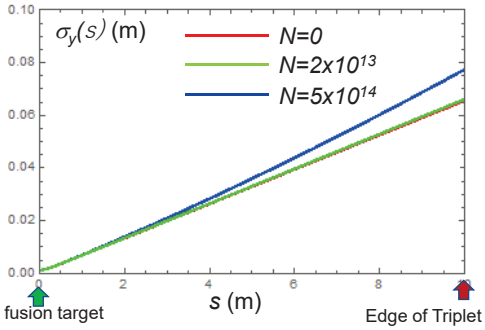

Figure 3.2: σ_y vs. s

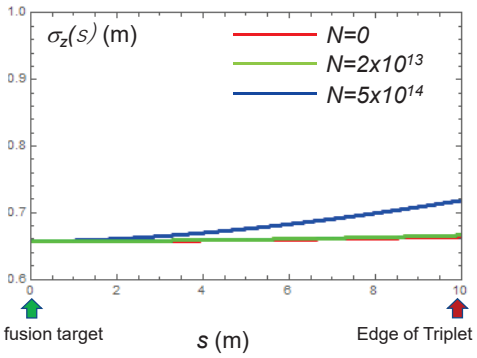

Figure 3.3: σ_z vs. s

4.2 Deceleration due to accumulated charge on the target

A magnitude of charge of order of 10^{15}x1.6x10^{-19} Coulomb brought in by 100 bunches has been already deposited on the target surface before a lower half-part of bunch arrives at the surface. Electric fields in the radial direction created around the target sphere, which is estimated to be 58 GV/m on the surface, may notably affect on the lower parts of 100 bunches which arrive late. It is rather simple to evaluate a magnitude of deceleration due to the longitudinal electric fields.

Fig.4 depicts the schematic view of target and projectile ion bunch. Now we will focus our attention on the bunch tail. Deceleration of this bunch tail is analytically obtained,

The magnitude of deceleration is shown in Fig. 5.

$$\Delta e(z) = \frac{e^2}{4\pi\varepsilon_0}\cdot\frac{N}{L_b}\cdot\left[1+\log\left(\frac{R+L_b}{z}\right)-\frac{R+L_b}{z}\right]$$

where

N is the total number of ions injected into the target, 2×10^{15},

L_b is the bunch length, 1.4 m,

R is the target radius, 5 mm

z is the position of bunch tail.

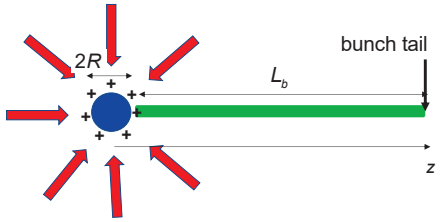

Figure 4: Target and projectile ion bunch

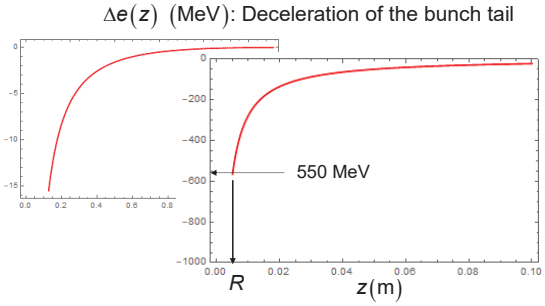

Figure 5: Deceleration of the bunch tail

Comparing this magnitude with the total energy of ion, ~ 10 GeV for Bi1+, it is not small. However, this effect seems to be still tolerable, although the range of projectile ion in tamper material is a bit reduced.

Here we have to reconsider the tremendous amount of 58 GV/m. 580 MV/cm on the target sphere is far beyond the nominal breakdown limit in a realistic vacuum. Positive ions floating in the reactor vessel would be rapidly collected by the charged target sphere. Consequently, The total amount of charge may be much reduced.

4.3 Disruption of mis-shot projectile ion bunches

On the other hand, the electric fields at the location where entire bunches encounter may take a role to cause a uniform eruption of mis-shot bunches. Exploded driver bunch debris will be absorbed in the first liq. metal wall. 6. An expanded beam size can be analytically evaluated, assumed the space-charge of $(L_b/2\sigma)$x3.2x10^{-4} C is uniformly piled up in a volume of $\pi\sigma^2$x2σ at the encounter region, as depicted in Fig. 6. Orbit equation of motion for a projectile ion in the encounter region is written by

In the orbit coordinate,

$$\frac{d^2x}{ds^2} = \frac{1}{2\pi\varepsilon_0}\cdot\left(\frac{Q^2}{A}\right)\cdot\left(\frac{e}{mc^2}\right)\cdot\frac{N}{\gamma\beta^2}\cdot\frac{e}{\sigma^2\cdot L_b}\cdot x = k^2\cdot x$$

where k^2 is zero for $s \geq 2\sigma$.

Here the term of k^2x in the right-hand side represents a linearized defocusing force. The envelope equation obtained straightforwardly from this orbit equation gives the evolution of beam size beyond encounter (see Fig. 7 and its mathematical deduction is given in Appendix.).

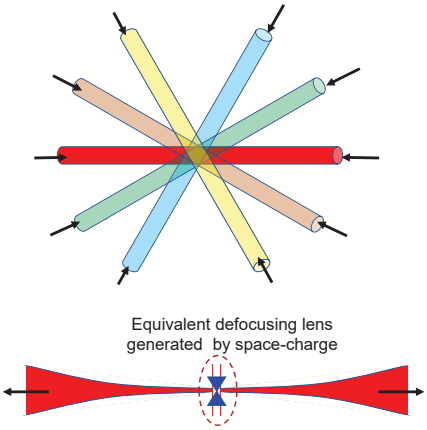

Figure 6: Schematic view of the encounter of mis-shot projectile ion bunches

One finds that the difference between Fig. 3,2 and Fig. 7 is rather small. Namely we will be unable to expect the disruption.

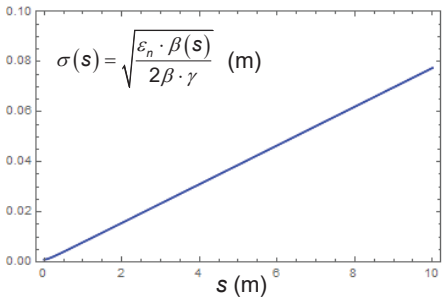

Figure 7: Evolution of rms beam size beyond encounter

5. Summary

A path adjusting scenario to guarantee synchronous irradiation of 100 projectile ion bunches on the fusion target has been given. The necessity of full beam power beam dumps has been emphasized, showing a reasonable solution for this. Three important beam dynamics issues:

1. Self space-charge effects
2. Deceleration of an incoming projectile ion bunch due to charge accumulated on the target surface
3. Disruption of mis-shot projectile ion bunches beyond their encounter

have discussed. We will conclude that Item 1 and 3 are not big issues and Item 2 should be in mind but not significant.

References

[1] K. Takayama *et al.*, "A massive-ion beam driver for high-energy-density physics and future inertial fusion", *Physics Letters A* ***384,*** 126692 (2020).

[2] プラズマ・核融合学会専門委員会（代表：長谷川純）「新たな日本版イオンビーム慣性閉じ込め核融合システムの設計」(2020-21)

[3] T. Ebisawa and K. Takayama, "3D beam-envelope approach for an asymmetric beam in a high intensity linac with a solenoid channel", submitted to *Phys. Rev. A&B* (2022).

蛯沢貴、髙山　健, D Coupled Envelope Approach for a High Intensity Linac and Its

Comparison with 3D Gaussian Macroparticle Simulation and PIC code (TraceWin) 2021 年度核融合科学研究所共同研究形式研究会プログラム 「パルスパワー技術およびプラズマ・量子ビーム技術の最新動向」

Appendix

$$\nabla \cdot \mathbf{E} = \frac{\rho}{\varepsilon_0}$$

If a volume of the encounter region is assumed $\pi\sigma^2 \times 2\sigma$,

$$\rho = \frac{QeN \cdot (2\sigma / L_b)}{\pi\sigma^2 \cdot 2\sigma} \;\Rightarrow\; E_r(r,0) \cdot 2\pi r \cdot 2\sigma = \frac{\rho}{\varepsilon_0} \cdot \pi r^2 \cdot 2\sigma$$

$$E_r(r,0) = \frac{\rho}{2\varepsilon_0} \cdot r = \frac{1}{2\varepsilon_0} \cdot \frac{QeN}{\pi\sigma^2 \cdot L_b} \cdot r = \frac{QeN}{2\pi\varepsilon_0 \cdot \sigma^2 \cdot L_b} \cdot r \qquad (1)$$

Equation of motion for a projectile ion is written by

$$Am\gamma \cdot \frac{d^2x}{dt^2} = QeE_r(r,0) \;\Rightarrow\; Am\gamma c^2\beta^2 \cdot \frac{d^2x}{ds^2} = \frac{Q^2e^2N}{2\pi\varepsilon_0 \cdot \sigma^2 \cdot L_b} \cdot x$$

In the orbit coordinate,

$$\frac{d^2x}{ds^2} = \frac{1}{2\pi\varepsilon_0} \cdot \left(\frac{Q^2}{A}\right) \cdot \left(\frac{e}{mc^2}\right) \cdot \frac{N}{\gamma\beta^2} \cdot \frac{e}{\sigma^2 \cdot L_b} \cdot x = k^2 \cdot x \qquad (2)$$

where k^2 is zero for $s \geq 2\sigma$.

Substitution of beam parmeters into the form of k^2 yields

$k^2 = 14.575\ \mathrm{m}^{-2}$

From (2), we have the beam envelope equation:

$$\rho'' - k^2 \cdot \rho = \frac{1}{\rho^3} \qquad (3)$$

Exact solution of (3) for $0 \leq s \leq 2\sigma$ is known in the form of

$$\begin{cases} \beta(s) = \rho^2(s) = c_1 \cdot \exp(2k \cdot s) + c_2 \cdot \exp(-2k \cdot s) - 2\sqrt{c_1 \cdot c_2 - 1/k^2} \\ \beta'(s) = 2k \cdot \left[c_1 \cdot \exp(2k \cdot s) - c_2 \cdot \exp(-2k \cdot s)\right] \end{cases} \qquad (4)$$

where c_1 and c_2 are determined from initial conditions,

$$\begin{cases} \beta(0) = c_1 + c_2 - 2\sqrt{c_1 \cdot c_2 - 1/k^2} \\ \beta'(0) = 2k \cdot (c_1 - c_2) = 0 \;\Rightarrow\; c_1 = c_2 \end{cases}$$

$$\beta(0) = 2c_1 - 2\sqrt{c_1^2 - 1/k^2} \;\Rightarrow\; 4\left(c_1^2 - 1/k^2\right) = 4c_1^2 - 4c_1 \cdot \beta(0) + \beta^2(0)$$

$$\Rightarrow\; 4c_1 \cdot \beta(0) = \beta^2(0) + \frac{4}{k^2} \;\Rightarrow\; c_1 = \frac{\beta(0)}{4} + \frac{1}{k^2 \cdot \beta(0)}$$

$$\beta'(s) = 4k \cdot c_1 \cdot \sinh(2k \cdot s) = 4k \cdot \left[\frac{\beta(0)}{4} + \frac{1}{k^2 \cdot \beta(0)}\right] \cdot \sinh(2k \cdot s)$$

Thus, we have

$$\begin{cases} \beta(2\sigma) \simeq \beta(0) = \beta^* \\ \beta'(2\sigma) = 4k \cdot \left[\frac{\beta^*}{4} + \frac{1}{k^2 \cdot \beta^*}\right] \cdot \sinh(4k \cdot \sigma) \end{cases} \qquad (5)$$

where $\beta^* = 0.13$ m is assumed in the design of Massive Ion ICF driver.

In the region of $s \geq 2\sigma$, the solution is known in a parabolic function of s,

$$\beta(s) = \frac{4 + \beta'(2\sigma)^2}{4 \cdot \beta(2\sigma)} \cdot (s - 2\sigma)^2 + \beta'(2\sigma) \cdot (s - 2\sigma) + \beta(2\sigma) \qquad (6)$$

RMS beam size is evaluated by

$$\sigma(s) = \sqrt{\frac{\varepsilon_n \cdot \beta(s)}{2\beta \cdot \gamma}} \qquad (7)$$

Study on Reactor Radius of Heavy-Ion Inertial Fusion

Takashi Kikuchi, Yuki Uchida*, Makoto Nakamura**,
Yoshihiro Kajimura***, Kazuhiko Horioka****

Nagaoka University of Technology
**National Institute of Technology (KOSEN), Nagaoka College*
***National Institute of Technology (KOSEN), Kushiro College*
****National Institute of Technology (KOSEN), Akashi College*
*****Tokyo Institute of Technology*

ABSTRACT

A reactor radius for a heavy-ion inertial fusion system was discussed in this study. The radius of reactor was related to gas pressure in the reactor. The gas pressure in the reactor was limited by an allowable level of heavy-ion beam transport to a fuel target. The gas pressure in the reactor increased by helium generated due to nuclear fusion reactions and hydrogen isotopes as a residual fuel. For this reason, the gas pressure was decreased to the allowable level of heavy-ion beam transport to the target using a vacuum pump. The pumping speed was estimated as a function of reactor radius, and the reactor radius was determined by the reasonable pumping speed.

Keywords

Heavy–Ion Inertial Fusion, Reactor Chamber, Reactor Radius, Pumping Speed, Beam Transport, Residual Gas Pressure

1 Introduction

A heavy-ion inertial fusion (HIF) system is one of inertial confinement fusion (ICF) schemes [1, 2]. Heavy-ion beams are irradiated to a fuel target in a reactor, and the irradiated fuel target is heated up. In the fuel target, ablation plasma is generated due to the heavy-ion beam irradiation, and the fuel is compressed into the center of target by the ablation plasma. Dense and high temperature core of the fuel is formed at the target center, and the nuclear energy is released by the nuclear fusion reactions.

The fuel pellet is placed in the reactor chamber, and is illuminated by the heavy-ion beams in the reactor chamber. The reactor has various functions such as the recovery of nuclear fusion output, beam transport environment, radiation shielding, tritium breeding, remnant gas exhaust, pellet material collection, and so on. For this reason, the radius of reactor chamber is related to the various components and factors as follows:

- first wall : wall thickness due to ablation
- vacuum vessel: structure and stiffness
- vacuum system: pumping speed and ultimate vacuum
- target injection: tracking
- beam transport: beam loss and focusing
- power generation equipment: working fluid temperature
- engineering safety equipment: radioactivation
- electromagnet protection: radiation shield and damage

As a result, the radius of reactor chamber is a critical parameter to construct the HIF power plant system.

Figure 1 shows typical operation in the ICF reactor [1, 2]. The gas pressure in the reactor is limited by an allowable level of heavy-ion beam transport to a fuel target. The gas pressure in the reactor increases by helium generated due to nuclear fusion reactions and hydrogen isotopes as a residual fuel. For this reason, the gas pressure should be decreased to the allowable level of heavy-ion beam transport to the target using a vacuum pump.

In the reactor design for laser driven ICF, the pressure is required less than 100 Pa [3]. The pressure is required by 1 Pa for laser driven ICF with fast ignition [4]. In the case of HIF reactor, the gas pressure is determined by the modes of ion beam propagation in the reactor chamber [5]. In this study, the mode of vacuum transport is assumed for the estimation of gas pressure, because of avoiding the various instabilities for ion beam propagation through the gas environment. The pressure is required in ranges of 0.01∼0.1 Pa [6] for the case of HIF. For this reason, the pumping speed and the ultimate vacuum are unique parameters for HIF system in comparisons with the laser driven ICF system. The pressure requirement in the reactor chamber and the pumping speed are estimated as a function of reactor radius in this study.

2 Gas Pressure in Reactor Radius due to Beam Transport

The allowable gas pressure in the reactor is estimated due to the limitation by the collisional ionization of the beam ion in the beam transport, it is written by [5]

$$P_t = \frac{1}{\sigma R} k_B T, \tag{1}$$

where σ is the collisional ionization cross section (e.g., 7×10^{-20} m^2 for Pb [5]), R is the reactor radius (standoff), k_B is the Boltzmann constant, and T is the gas temperature (300 K), in the case of strong stripping ($n\sigma R = 1$ where n is the number of density for gas). In the ICF reactor, it has been proposed to protect the reactor wall by flowing

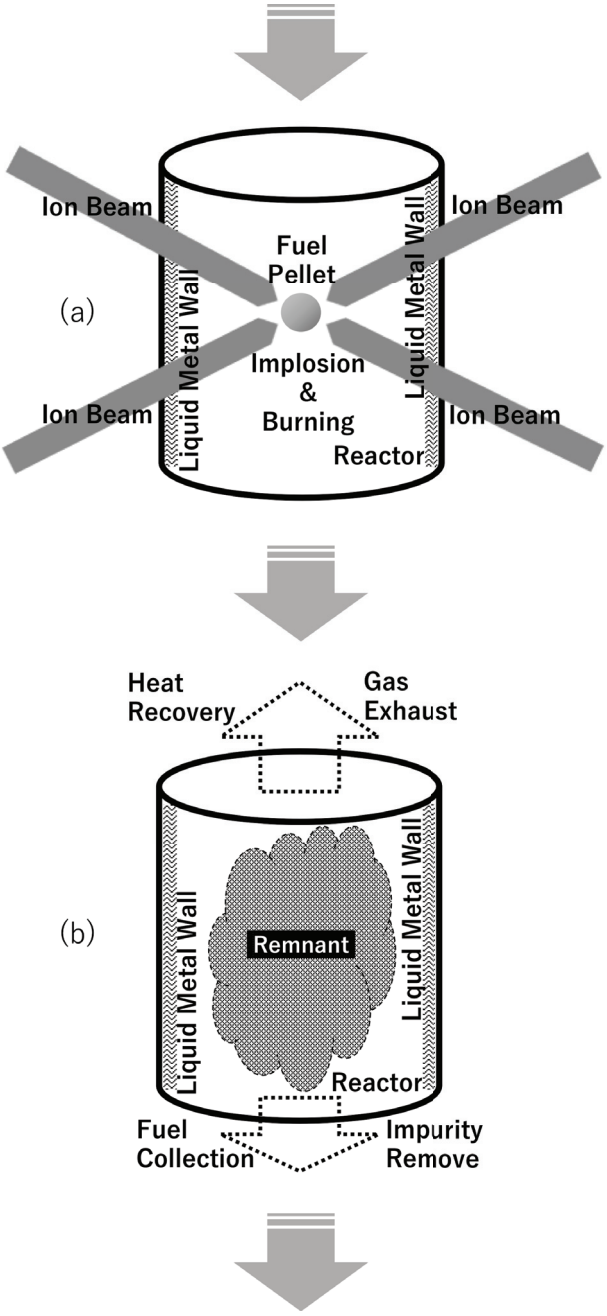

Figure 1: Typical operation in ICF reactor. (a) a fuel pellet is irradiated by ion beams, and nuclear fusion burning with implosion process. (b) nuclear fusion output, remnant gas, and pellet structure material are collected by liquid metal wall and vacuum pump. (a) and (b) processes are repeatedly operated with several Hz, typically.

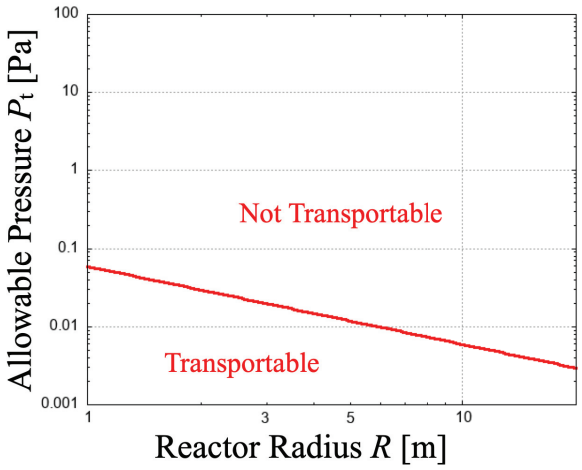

Figure 2: Allowable pressure as a function of reactor radius for Pb gas particle.

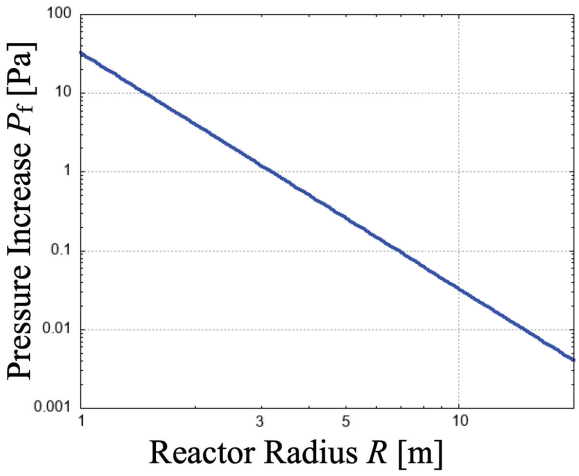

Figure 3: Pressure increase per shot as a function of reactor radius.

liquid metal, which contains Li such as Li, FLiBe (Flibe), and LiPb [1–6]. The beam transport was estimated by the collisions between the beam ion and Pb, because Pb has the largest collisional cross section in the candidates.

Figure 2 shows the allowable gas pressure as a function of the reactor radius.

3 Gas Pressure in Reactor Radius due to Residual Fuel and Fusion Output

The gas pressure in the reactor increase after the fuel pellet implosion, because the DT nuclear reaction creates He and the residual fuel (DT) diffuses in the reactor chamber. The increase of gas pressure is estimated by

$$P_f = \frac{N_f}{V_R} k_B T = \frac{3N_f}{4\pi R^3} k_B T, \tag{2}$$

where N_f is the number of diffused gas particles (D, T, and He) per shot and $V_R = 4\pi R^3/3$ is the reactor volume. In this study, the number of gas particles (D, T, and He) per shot was assumed by 3.3×10^{22} for the burn fraction of 0.3 [2] and the fusion output of 2 GJ per shot.

Figure 3 shows the pressure increase per shot as a function of the reactor radius.

4 Requirement for Pumping Speed

The gas pressure in the reactor increases after the fuel pellet implosion, because the DT nuclear reaction creates He and the residual fuel (DT) diffuses in the reactor chamber.

The pumping (exhaust) speed S for a vacuum pump is estimated by

$$S = -\frac{V_R \Delta P}{P \Delta t}, \tag{3}$$

where P is the gas pressure during the pressure difference ΔP by the time interval Δt. The gas pressure difference is rewritten by

$$\Delta P = P_b - P_a, \tag{4}$$

where P_b and P_a indicate the gas pressure before and after the shot. In this study, the gas pressure P_b before the shot is assumed by the allowable gas pressure P_t for the beam transport ($P_b = P_t$). For this reason, the gas pressure P_a after the shot is increased from P_b by the pressure increase P_f due to the gas particles (D, T, and He), and is written by

$$P_a = P_b + P_f = P_b + \frac{3N_f}{4\pi R^3} k_B T, \tag{5}$$

and

$$P = \frac{P_a + P_b}{2}, \tag{6}$$

is roughly evaluated in this study. Consequently, the pumping speed is calculated by

$$S = \frac{8\pi\sigma N_f R^3}{8\pi R^2 + 3\sigma N_f} \frac{1}{\Delta t}, \tag{7}$$

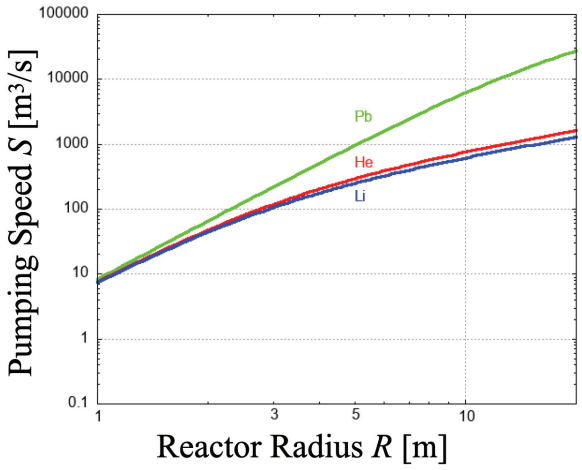

Figure 4: Required pumping speed as a function of reactor radius with time interval of 1 sec.

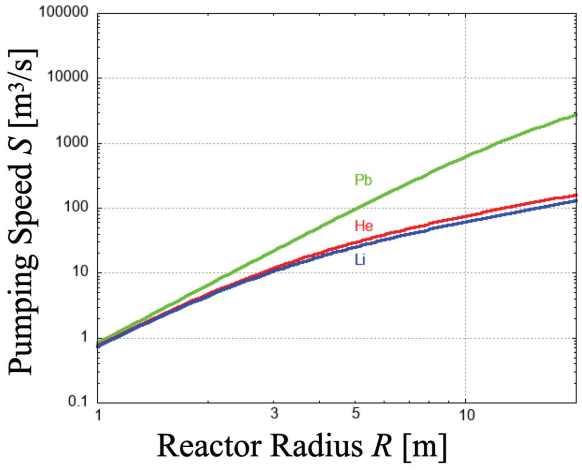

Figure 5: Required pumping speed as a function of reactor radius with time interval of 10 sec.

where σ is assumed by 7×10^{-20} m^2 for Pb [5], 2×10^{-21} m^2 for Li [5], and 2.5×10^{-21} m^2 for He [7], respectively.

Figure 4 shows the required pumping speed as a function of the reactor radius with the shot-by-shot time interval $\Delta t = 1$ sec determined by 1 Hz [8].

The pumping speed per reactor can be reduced using multi reactor design. In the case of 10 reactors, the pumping speed is decreased by 10 at each reactor. Figure 5 shows the required pumping speed as a function of the reactor radius with the time interval of 10 sec.

Li and Pb contained in the liquid metal readhere mainly to the liquid metal for protection of the reactor wall. For this reason, the main work of the vacuum pump is to pump out He and residual fuel (DT) gases.

The pumping speed of 10 m^3/s is assumed as the design parameter in case of KOYO-F [4]. The pumping speed up to 6.2 m^3/s is required by the HYLIFE-II [6]. For this reason, the reactor radius of $3 \sim 5$ m is suitable for the HIF system.

5 Conclusion

In this study, the reactor radius was discussed for the HIF system from the viewpoint of gas pressure in the reactor. The gas pressure in the reactor was limited by the allowable level of heavy-ion beam transport to the fuel target, and increased by the helium generated due to the nuclear fusion reactions and the hydrogen isotopes as the residual fuel. The gas pressure should be decreased to the allowable level of beam transport to the target using the vacuum pump. For this reason, the reactor radius was determined by the reasonable pumping speed.

The pumping speed was estimated as a function of reactor radius. The vapor pressure for LiPb is 0.01∼0.1 Pa [9]. The radius of 10 m is one of limitation for the reactor radius from the viewpoint of vapor pressure for LiPb as shown in Figs. 2 and 3. Consequently, it was found that the reactor radius of $3 \sim 5$ m is suitable for the HIF system on 1 Hz operation with 10 reactors from the viewpoint of vacuum system.

References

[1] S. ATZENI and J. MEYER-TER-VEHN, *The Physics of Inertial Fusion: Beam Plasma Interaction, Hydrodynamics, Hot Dense Matter* (Oxford Univ., N.Y., 2004).

[2] S. PFALZNER, *An Introduction to Inertial Confinement Fusion (Series in Plasma Physics)* (CRC Press, 2006).

[3] W.R. MEIER, *Fusion Eng. Design* **89**, pp.2489∼2492 (2014).

[4] *Conceptual Design for Fast Ignition Laser Fusion Power Plant*, p.64 (ILE, Osaka Univ. and IFE Forum, 2006) (in Japanese).

[5] A.B. LANGDON, *Particle Accelerators* **37-38**, pp.175∼180 (1992).

[6] R.W. MOIR, *Fusion Tech.* **25**, pp.5∼25 (1994).

[7] J. HASEGAWA, *private communication*

[8] K. TAKAYAMA, T. ADACHI, T. KAWAKUBO, K. OKAMURA, Y. YURI, J. HASEGAWA, K. HORIOKA, T. KIKUCHI, T. SASAKI, K. TAKAHASHI, *Phys. Lett.* **A384**, pp.126692-1∼126692-11 (2020).

[9] D. MARTELLI, A. VENTURINI, and M. UTILI, *Fusion Eng. Design* **138**, pp.183∼195 (2019).

Publication List of NIFS-PROC. Series

NIFS-PROC-108
Edited by Yeong-Kook OH, Shigeru MORITA and Liqun HU
Proceeding of A3 Foresight Program Seminar on Critical Physics Issues Specific to Steady State Sustainment of High-Performance Plasmas November 22-25, 2016, Jeju, Korea
Jan. 11,. 2018

NIFS-PROC-109
Edited by Shigeru MORITA, Liqun HU and Yeong-Kook OH
Proceeding of A3 Foresight Program Seminar on Critical Physics Issues Specific to Steady State Sustainment of High-Performance Plasmas 11-14 July, 2017, Sapporo, Japan
Jan. 12, 2018

NIFS-PROC-110
Edited by Jun Hasegawa and Tetsuo Ozaki
Resent Developments of Pulsed Power Technology and Plasma Application Research
Jan. 12, 2018

NIFS-PROC-111
Edited by Liqun HU, Shigeru MORITA and Yeong-Kook OH
Proceeding of A3 Foresight Program Seminar on Critical Physics Issues Specific to Steady State Sustainment of High-Performance Plasmas 12 - 15 December, 2017, Chongqing, China
Jun. 11, 2018

NIFS-PROC-112
Edited by E. Kikutani (KEK) and S. Kubo (NIFS)
Proceedings of the meeting on Archives in Fields of Natural Sciences in FY 2017
Oct. 18, 2018 (Written in Japanses)

NIFS-PROC-113
Pulsed Power and High-Density Plasma and its Applications
Edited by Koichi Takaki and Tetsuo Ozaki
Feb. 6, 2019

NIFS-PROC-114
The 7th Japan-China-Korea Joint Seminar on Atomic and Molecular Processes in Plasma (AMPP2018)
Edited by Daiji Kato, Ling Zhang, and Xiaobin Ding
May 10, 2019

NIFS-PROC-115
CFQS TEAM
NIFS-SWJTU JOINT PROJECT FOR CFQS -PHYSICS AND ENGINEERING DESIGN-
VER. 2.1 2019. SEP.
Nov. 8, 2019

NIFS-PROC-116
Satoshi Ohdachi, Editor of the Post-CUP Workshop proceeding
Collected papers at the 2019 Post-CUP Workshop & JSPS-CAS Bilateral Joint Research Projects Workshop, 24th-26th July, 2019, Nagoya, Japan
Feb. 21, 2020

NIFS-PROC-117
Edited by E. Kikutani (KEK) and S. Kubo (NIFS)
Proceedings of the meetings on Archives in Fields of Natural Sciences in FY2018
June. 9, 2020 (Written in Japanses)

NIFS-PROC-118
Edited by Tetsuo Ozaki and Sunao Katsuki
New Development of Beam Physics and the Application by New Generation Plused Power Technology
June. 29, 2020
National Institute for Fusion Science, National Institutes of Natural Sciences
Institute of Fusion Science, School of Physical Science and Technology, Southwest Jiaotong University

NIFS-PROC-119
Hefei Keye Electro Physical Equipment Manufacturing Co. Ltd.
NIFS-SWJTU JOINT PROJECT FOR CFQS -PHYSICS AND ENGINEERING DESIGN-
VER. 3.1 2020. NOV.
Jan. 25, 2021

NIFS-PROC-120
Edited by Izumi Tsutsui (KEK) and Shin Kubo (NIFS)
Proceedings of the meetings on Archives in Fields of Natural Sciences in FY2019
Feb. 25, 2021

NIFS-PROC-121
Edited by Hiroaki Ito and Tetsuo Ozak
Frontier of Advanced Pulsed Power Technology and its Application to Plasma and Particle Beam
Nov. 08, 2021

NIFS-PROC-122
National Institute for Fusion Science, National Institutes of Natural Sciences
Institute of Fusion Science, School of Physical Science and Technology, Southwest Jiaotong University
Hefei Keye Electro Physical Equipment Manufacturing Co. Ltd.
NIFS-SWJTU JOINT PROJECT FOR CFQS -PHYSICS AND ENGINEERING DESIGN-
VER. 4.1 2022. JAN.
Feb. 10, 2022

NIFS-PROC-123
Edited by Jun Hasegawa and Tetsuo Ozaki
Resent Developments of Pulsed Power Technology and Plasma Application Research
Feb. 5, 2023